INVESTIGATION OF TOPOTACTIC REDUCTION PROCESSES FOR MANGANATE (n=1) RUDDLESDEN-POPPER PHASES AND SCANDIUM VANADATE

By

BRAD HERNDEN

A Thesis submitted to the Faculty of Graduate Studies of

The University of Manitoba

in partial fulfilment of the requirements of the degree of

MASTER OF SCIENCE

Department of Chemistry

University of Manitoba

Winnipeg, Manitoba, Canada

Copyright © 2011 by Brad Hernden

ABSTRACT

Over the last decade progress towards step-wise structural transformations in solid state chemistry has been made using metal hydride reductants. Alkali and alkali-earth metal hydrides can effectively reduce transition metal oxides resulting frequently in novel oxygen defect structures. This provides access to control over cation oxidation states and magnetic exchange pathways, and thus electronic and magnetic properties. The goal for this research was to investigate a representative system that could be used both for exploration of novel oxygen defect phases and for investigating the fundamental parameters governing successful solid state reductions. The systems chosen for investigation were $Sr_{2-x}Ca_xMnO_4$ ($0<x<2$) and $Sr_{2-x}Ba_xMnO_4$ ($x< 0.04$). Detailed analysis of metal hydride reactivity with Sr_2MnO_4 is presented in addition to proof of the solid state reduction mechanism. As a result a number of novel oxygen defect phases have been produced, Sr_2MnO_{4-x} ($0<x<0.37$). The potential for producing novel lithium doped Sr_2MnO_{4-x} phases using a reduction/insertion approach with LiH has also been identified. Lastly as a test of application for metal hydrides as reductants the ability to topotactically reduce $ScVO_4$ has been investigated.

ACKNOWLEDGEMENTS

I would like to express thanks foremost to my supervisor Dr. Mario Bieringer for his guidance and support throughout my project. Our weekly meetings in which we exchanged thoughts and ideas about my research were invaluable to the success of my project. I am grateful for the financial and travel support I have received from my supervisor, Chemistry Department, Faculty of Science and the Faculty of Graduate Studies.

Thanks to Frank Gibbs of McMaster University for collection of TGA data. I would also like to acknowledge the Nanomagnetism Research Group headed by Dr. Van Lierop for allowing me access to the SQUID magnetometer in the Department of Physics and also Vladimir Michaelis and the Kroeker Research Group for allowing me access to a high temperature furnace.

Thanks to fellow group member Shahid Shafi for technical and research advice. I also extend thanks to Lesa Cafferty for manufacturing custom glassware.

Special thanks to my parents (Valerie & Kevin) and my brothers (Ricky & Mike) for all their advice and encouragement.

TABLE OF CONTENTS

LIST OF TABLES

LIST OF FIGURES

1. INTRODUCTION

Part I – Introduction to Instrumentation

1.1. General Diffraction Theory

Diffraction techniques are commonly used to characterize crystalline solids. A suite of diffraction techniques are based upon the interaction of types of radiation or particles with crystalline materials. The long range periodic order of crystalline materials allows them to be characterized by diffraction techniques. Hence amorphous materials lacking long range order cannot be characterized by diffraction methods. The choice of radiation used (e.g. electrons, neutrons, X-rays) governs the interaction at the atomic level thus also determines the atomic detail which can be probed for a material. The periodic atomic structure of single crystals and polycrystalline powders can be determined due to the interaction of X-rays with electron density. Neutron diffraction provides the ability to characterize both a material's atomic and magnetic structure due to the interaction of neutrons with nuclei and magnetic moments. Often X-ray and neutron diffraction experiments accompany one another to determine a material's crystallographic and magnetic structure. X-ray diffraction is readily accessible in laboratory settings. In contrast, neutron diffraction is limited to large scale research facilities such as nuclear research reactors and neutron spallation sources. Electrons are unique among the radiation sources available as they are very commonly used for imaging of both direct space using microscopic techniques (e.g. SEM), and also reciprocal space as does X-rays and neutrons through diffraction. Although X-ray and neutron microscopy techniques are available they are not as common as electron

microscopy. The interaction of electrons with a material is strong compared to that of X-rays and neutrons. Electrons interact strongly due to their charged nature with interactions heavily influenced by Coulombic repulsion and attraction with electrons and nuclei respectively. As a result electron diffraction interactions are explained using a complex dynamical theory while interactions of X-rays and neutrons can be explained using a more simple kinematical theory.

1.2. Powder X-ray Diffraction

Bragg's law (equation 1.1) is widely used as a mathematically equivalent interpretation of X-ray diffraction from crystallographic planes.

$$\lambda = 2d_{(hkl)}\sin\theta \qquad \textbf{1.1.}$$

Bragg's law is dependent on the wavelength (λ) of the incoming X-rays, the interplanar spacing (d_{hkl}) separating sets of lattice planes and the incident angle of incoming X-rays (θ). The satisfaction of Bragg's law requires the path length difference ($2d\sin\theta$) between incident and diffracted X-rays for scattering from adjacent planes to be an integer multiple of the wavelength (figure 1.1). This condition gives rise to in-phase diffracted X-ray photons which interfere constructively producing a Bragg peak at angle 2θ with respect to the incident beam. X-ray wavelengths used in powder X-ray diffraction typically range between 0.5-2.5Å.[1] The choice is dependent on the material to be characterized such that the wavelength should be on the same order as the smallest interatomic distance. Thus for inorganic materials CuKα (~1.54Å) radiation is commonly chosen while for organic

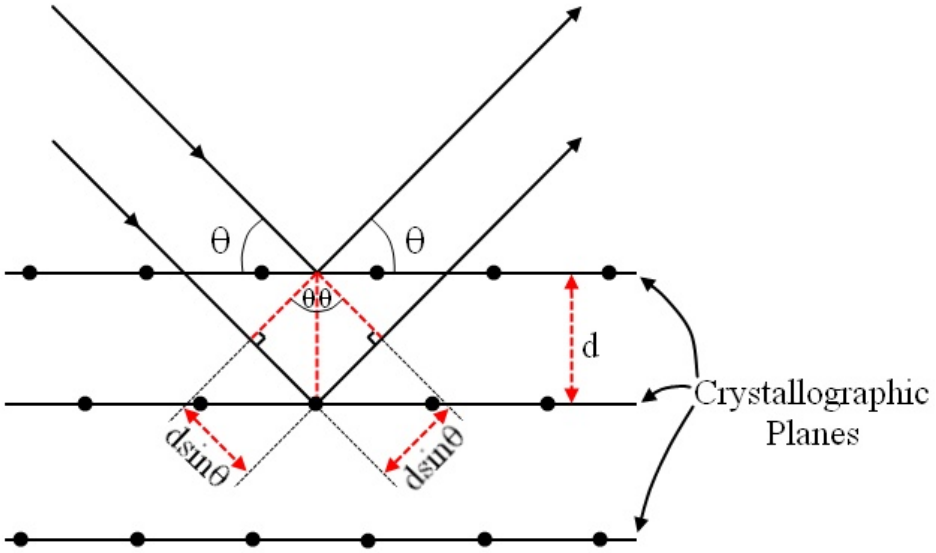

Figure 1.1. Illustration of the underlying geometry of Bragg's Law.

compounds MoKα (~0.71 Å) radiation is more suitable. Factors such as absorption and fluorescence which depend on the relationship between sample composition and wavelength should also be considered. Additionally the choice of wavelength can be utilized to effectively expand (increase λ) or compress (decrease λ) a data set over the 2θ range. This can be used as a tool to optimize data resolution.

The reliability of powder X-ray diffraction data strongly depends on the quality of the sample and proper mounting of the polycrystalline sample. An ideal sample mount contains a suitable number of crystallites such that a completely randomized distribution of crystallite orientations is satisfied. Spinning the sample during data acquisition can improve the data quality since averaging over a larger number of crystallites and thus orientations is accomplished. It is also important to note that powder X-ray diffraction of a polycrystalline sample provides crystallographic information representing an average

for the sample. Thus differences that occur among unit cells for a particular material (e.g. atomic composition, atomic coordinates, vacancies, clustering) cannot be directly probed by powder X-ray diffraction.

The structure factor ($F_{(hkl)}$) equation describes the phase and amplitude of a resultant wave which has been diffracted from the contents of a unit cell with respect to a particular set of (hkl) planes (equation 1.2).

$$F_{(hkl)} = \sum_{j=1}^{n} f_j(2\theta) \exp[i2\pi(hx_j + ky_j + lz_j)] \qquad \textbf{1.2.}$$

In equation 1.2 f_j represents the form factor for atom j located with atomic coordinates (x_j, y_j, z_j) such that Bragg's law is satisfied for Miller indices (hkl) at 2θ. Figure 1.2 illustrates the form factors for several atoms (H, O, Sc, Ti, Mn). Scattering factors are dependent on

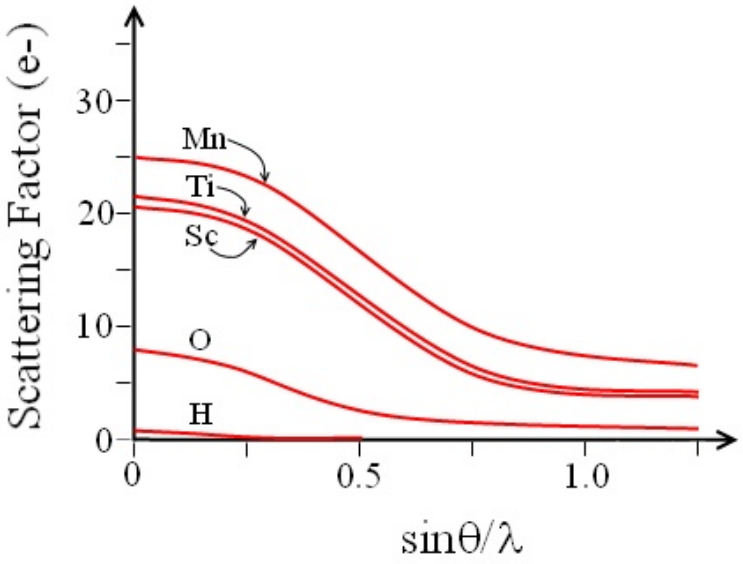

Figure 1.2. Illustration of form factors for H, O, Sc, Ti and Mn constructed by plotting scattering factor as a function of sinλ/θ. As a reference sinλ/θ = 0.25 corresponds to 2θ ≈ 45° for CuKα$_{1,2}$ (~1.54Å).[1]

an atom's electron density and also on the 2θ angle (sinλ/θ). At 2θ = 0º the scattering factor is directly proportional to the atom's electron density. The reduction of an atomic scattering factor with increasing 2θ results from the radial distribution of electrons about the nucleus. Thus it is clear that light atoms such as hydrogen will be challenging to locate and also that atoms of similar electron density (e.g. Sc, Ti) will be difficult to distinguish. Equation 1.3 relates the integrated intensities for Bragg peaks with the corresponding structure factors.

$$I_{hkl} \alpha F_{hkl}^2 \qquad \textbf{1.3.}$$

Various other factors influence the integrated intensity (I_{hkl}) of Bragg peaks in powder diffraction patterns as shown in equation 1.4.[1]

$$I_{(hkl)} = K \times p_{(hkl)} \times L_\theta \times P_\theta \times A_\theta \times T_{(hkl)} \times E_{(hkl)} \times \left|F_{(hkl)}\right|^2 \qquad \textbf{1.4.}$$

The components of equation 1.4 will be briefly discussed. The scale factor (*K)* is a constant used to relate experimental integrated intensities to calculated intensities. This is most relevant for Rietveld refinements (*1.2.2*). Bragg peak multiplicity is accounted for by the multiplicity factor (p_{hkl}). Peak multiplicity corresponds to the number of reciprocal lattice (3-dimensional) points which coincide at the same 2θ angle in a powder X-ray diffraction pattern (1-dimensional). This is closely related to the crystal system, as the lattice symmetry decreases the Bragg peak multiplicity decreases as well. Figure 1.3 illustrates the origin of peak multiplicities for a cubic and a tetragonal system as encountered in a powder diffraction pattern. It is evident from figure 1.3 that lower symmetry lattices (e.g. tetragonal vs. cubic) will have higher peak densities over the 2θ range of a powder X-ray diffraction pattern. The Lorentz factor (L_θ) corrects integrated intensities for specific geometrical factors influencing diffraction (e.g. reciprocal lattice

point size). The polarization factor (P_θ) accounts for partial polarization of the resultant diffracted X-ray beam. A particularly important factor to consider in powder X-ray diffraction is a material's linear absorption coefficient (μ, cm^{-1}). Linear absorption coefficients can be converted to mass absorption coefficients by dividing by a material's density (μ/ρ, cm^2/g).[1] Correction for absorption (A_θ) is most important in highly absorbing materials. Large absorption is often accompanied by re-emission phenomena such as fluorescence. Additionally X-ray absorption is influential over the diffraction geometry most suitable for a sample (*1.2.1*). Depending on the shape of the crystallites in a polycrystalline sample preferred orientation may occur in which the crystallites align in a non-randomized orientation on the sample holder. This can cause inaccuracies in relative intensities among Bragg peaks and in some instances complete absences of expected Bragg peaks. This emphasizes the importance of a properly prepared sample. Preferred orientation is accounted for by the intensity correction factor $T_{(hkl)}$. Preferred orientation can be reduced significantly and possibly eliminated by using a cavity sample holder or a glass capillary. The final component which can influence integrated intensity is X-ray extinction (E_{hkl}) which must be considered only for samples in which complex secondary or tertiary scattering of X-rays take place.

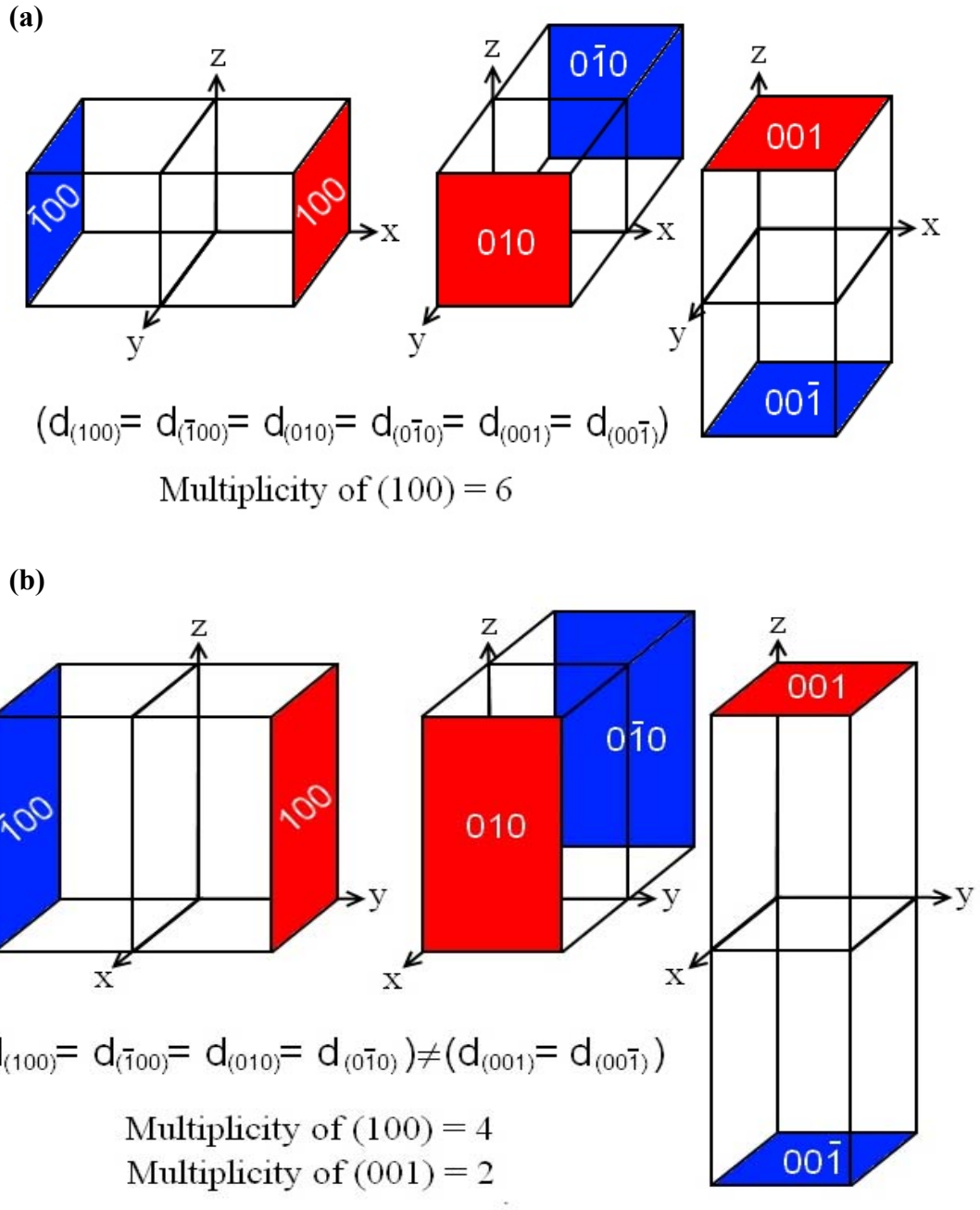

Figure 1.3. Illustration of Bragg peak multiplicity in powder X-ray diffraction. A cubic lattice with a multiplicity of 6 for the (100) Miller index (a) and a tetragonal lattice with a multiplicity of 2 for the (001) Miller index and 4 for the (100) Miller index (b).

1.2.1 Powder X-ray Diffractometer

Powder X-ray diffractometers consist of 5 main components including an X-ray source, goniometer, sample stage, detector and X-ray beam optics. X-rays are produced by the acceleration of electrons toward the X-ray tube anode material (e.g. Cu, Mo, Ag, etc) resulting in characteristic X-ray emission lines. The goniometer for the PANalytical X'Pert PRO diffractometer used in this study has a sample stage (e.g. spinner, capillary, high T furnace) and arms to which the X-ray source, detector and beam optic modules are fitted. The goniometer gearing is designed for the use of Bragg-Brentano θ-2θ parafocusing reflection geometry (figure 1.4). Transmission geometry is an alternative instrument geometry suitable for materials with low linear absorption coefficients. The

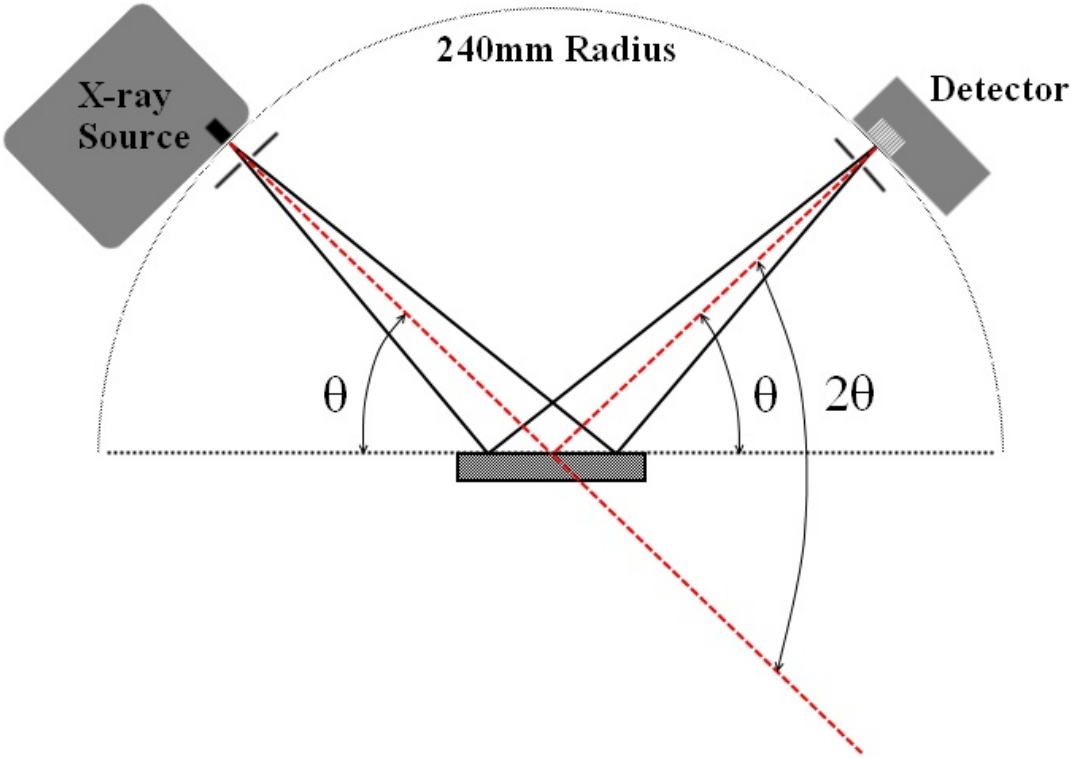

Figure 1.4. Illustration of a Bragg-Brentano θ-2θ geometry powder X-ray diffractometer.

PANalytical X'Celerator real time multiple strip (RTMS) linear position sensitive detector ($2\theta \approx 2^{o}$) contains 128 elements allowing for detection and spatial 2θ resolution of incoming X-rays. This ultimately allows for powder diffraction patterns to be plotted with photon counts on the y-axis and Bragg angle, 2θ on the x-axis. Incident and diffracted X-ray beam optics are used to control beam divergence and filtering of undesired X-ray wavelengths.

1.2.2 Rietveld Refinement

Provided a structural model is known for a crystalline material full pattern Rietveld refinement can be used to fit the model to experimental data. Rietveld refinement employs nonlinear least squares regression analysis in which progressive refinement of both instrumental and structural parameters through consecutive least squares cycles allows for minimization of the residuals, Φ, between the calculated and observed diffraction patterns (equation 1.5). Observed (Y_i^{obs}) and calculated (Y_i^{calc}) intensities are weighted based on photon count ($w_i = Y_i^{-1}$) as a function of 2θ steps (i).[1]

$$\Phi = \sum_{i=1}^{n} w_i (Y_i^{obs} - Y_i^{calc})^2 \qquad \textbf{1.5.}$$

Parameters which can be refined include zero point shift, sample displacement, scale factor, unit cell parameters, peak shape (e.g. pseudo-voight), peak asymmetry, background, atomic coordinates, Debye-Waller factor, site occupancy factor and U,V,W half-width parameters (equation1.6). In equation 1.6, H is the full width at half maximum dependent on 2θ angle with U,V,W being variables measured in $2\theta(^{o})$.[1]

$$H = (U \tan^2 \theta + V \tan \theta + W)^{1/2} \qquad \textbf{1.6.}$$

Figures of merit (e.g. R_p, R_{wp}, R_{exp}, χ^2, R_B) are important measures of refinement quality. R_p is the profile residual, R_{wp} is the weighted profile residual, R_{exp} is the expected profile residual, χ^2 is the goodness of fit, R_B is the Bragg residual. In addition to the parameters defined above, I_i^{obs} and I_i^{calc} are the observed and calculated integrated intensity at 2θ steps (i), n is the number of data points, p is the total number of parameters refined and m is the number of Bragg reflections (equation 1.7 – 1.11).[1]

$$R_p = \frac{\sum_{i=1}^{n} \left| Y_i^{obs} - Y_i^{calc} \right|}{\sum_{i=1}^{n} Y_i^{obs}} \times 100\% \qquad \textbf{1.7.}$$

$$R_{wp} = \left[\frac{\sum_{i=1}^{n} w_i (Y_i^{obs} - Y_i^{calc})^2}{\sum_{i=1}^{n} w_i (Y_i^{obs})^2} \right]^{1/2} \times 100\% \qquad \textbf{1.8.}$$

$$R_{\exp} = \left[\frac{n-p}{\sum_{i=1}^{n} w_i (Y_i^{obs})^2} \right]^{1/2} \times 100\% \qquad \textbf{1.9.}$$

$$\chi^2 = \left[\frac{R_{wp}}{R_{\exp}} \right]^2 \qquad \textbf{1.10.}$$

$$R_B = \frac{\sum_{i=1}^{m} \left| I_i^{obs} - I_i^{calc} \right|}{\sum_{i=1}^{m} I_i^{obs}} \times 100\% \qquad \textbf{1.11.}$$

The profile residual (R_p) and weighted profile residual (R_{wp}) differ by the weighting scheme ($w_i = 1/Y_i^{obs}$) applied to observed intensities in R_{wp}. This results in the smallest

observed intensities receiving the highest weighting. Thus R_{wp} results in a more even weighting of intensity differences (Y_i^{obs}-Y_i^{calc}) from both the largest and smallest observed intensities contributing to the residuals. The expected profile residual is similar to the weighted profile residual with the exception that the residual between observed and calculated intensity is replaced by the difference between the number of data points and refined parameters. Therefore R_{exp} is a measure of refinement quality independent of residual intensity and is heavily influenced by Y_i^{obs}. The presence of Y_i^{obs} in the denominator for all of R_p, R_{wp} and R_{exp} can lead to misleadingly low figures of merit in the presence of very high diffraction pattern backgrounds. The Bragg residual (R_B) is similar to the profile residual (R_p) with the exception that integrated observed and calculated intensities are used. Additionally the goodness of fit χ^2 is derived from R_{wp} and R_{exp}. Both R_B and χ^2 are important since they do not contain denominators depending on observed intensity thus making them reliable measures of refinement quality even in the presence of large background intensity.

1.3. Thermal Analysis

Several thermal analysis techniques are available to help characterize crystalline materials. Among these techniques are thermogravimetric analysis (TGA), differential thermal analysis (DTA) and differential scanning calorimetry (DSC). Modern instruments such as the Linseis L81 thermal analyzer shown in figure 1.5 allow for simultaneous TGA/DTA/DSC analysis. Mainly TGA will be introduced here since DTA and DSC were not performed during this research. TGA is based on precisely monitoring the changes in mass of a sample with microgram resolution over a programmable heating profile.

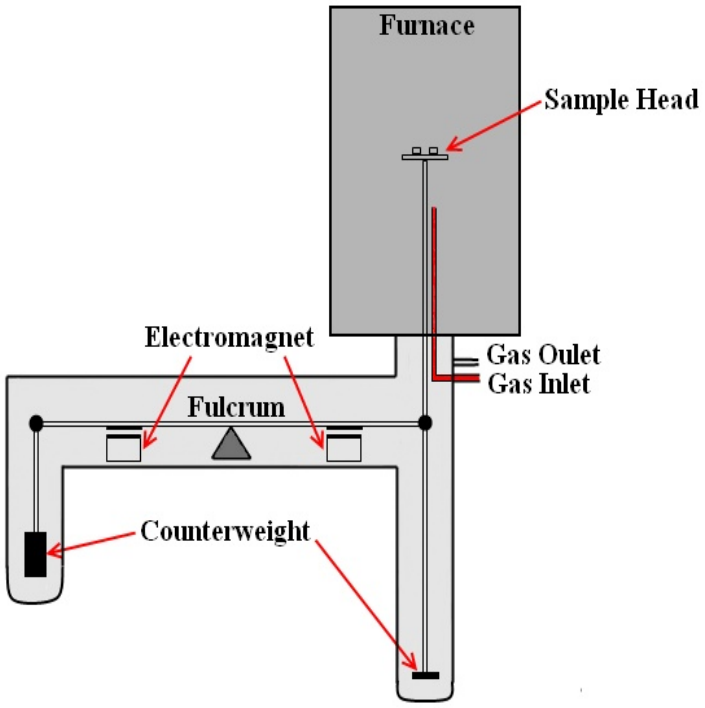

Figure 1.5. An illustration of the Linseis L81 thermal analyzer.

A compensation weighing system is used which consists of a fulcrum, two counter weights, two electromagnets and a sample head. This design ensures that all components are stationary during measurement with mass changes related to the current applied to the electromagnets. Oxidation and reduction reactions are examples of reactions that can be followed by quantifying oxygen loss or uptake by a material. Control of the sample environment during heating is essential thus there is a gas inlet/outlet allowing desired reaction conditions to be achieved. Buoyancy correction by subtraction of a background experiment collected with either empty crucibles or crucibles with inert material (e.g. Al_2O_3) is essential for accurate data analysis. DTA measures the difference in temperature (ΔT) between sample and reference (e.g. empty crucible or inert material) which can be measured in ^{o}C or μV. Resultant DTA peaks are either endothermic or

exothermic depending on the nature of the phase transition. Using a combination of thermal techniques such as TGA/DTA/DSC allows for thorough understanding of materials behaviour during heat treatment under specific reaction conditions.

1.4. Magnetism

The magnetic dipole moment (μ) results from the spin of electrons and orbital angular momentum. Typically consideration of only spin contributions is adequate for light (3d) transition metals (equation 1.12). Quenching of orbital angular momentum results from limitations imposed on orbital motion in ions due to interactions with the crystal field of nearby ions. In equation 1.12 (g) represents the gyrometric ratio which is 2 for free electrons and S represents the total spin quantum number.[2]

$$\mu_s = g[S(S+1)]^{1/2} \quad \textbf{1.12.}$$

A magnetic dipole moment influences the materials magnetization and magnetic susceptibility. The magnetization (M) of a material depends on the materials magnetic susceptibility per unit volume (χ_v) and on the applied magnetic field (H, [A/m]) as shown in equation 1.13.[3]

$$M = \chi_v H \quad \textbf{1.13.}$$

Since H can be controlled experimentally differences in magnetic response arise from magnetic susceptibility. Ultimately the value of a materials magnetic susceptibility depends on the magnetic ion energy states available for electrons to be thermally distributed among. Several factors can cause splitting of quantum energy states (e.g. m_l quantum numbers) in free ions including the presence of a crystal field, spin-orbit coupling, application of a magnetic field (e.g. Zeeman effect) or electron-electron

repulsion. Therefore progression from the consideration of magnetic properties in individual ions to extended structures can be challenging since interactions between ions in a crystal lattice can influence magnetic properties (e.g. cooperative magnetism).

1.4.1. Paramagnetism

Paramagnetism is a property of dilute magnetic systems in which magnetic moments do not interact cooperatively. The Curie Law (equation 1.14) is used to describe the relationship between susceptibility and temperature for a paramagnetic system. Plotting $1/\chi$ vs. T for paramagnetic materials produces a characteristic linear positive slope through the origin with slope 1/C shown in figure 1.6.

$$\chi = \frac{C}{T} \qquad \textbf{1.14.}$$

The magnetic susceptibility of paramagnetic systems is heavily dependent on temperature as thermal agitation limits the ability of moments to align at high temperature. It should also be noted that diamagnetic corrections (temperature independent) are typically applied to paramagnetic susceptibilities to account for the small contribution of paired core electrons. From the Curie Law the effective magnetic moment can be calculated using equation 1.15.[3]

$$\mu_{eff} = 2.828(\chi T)^{1/2} \qquad \textbf{1.15.}$$

1.4.2. Cooperative Magnetism and Exchange Interactions

Ferromagnetic, antiferromagnetic and ferrimagnetic states are examples of cooperative magnetic behaviour. The Curie-Weiss law shown in equation 1.16 can be

used to identify materials that have temperature dependent transitions from a paramagnetic state to an antiferromagnetic or ferromagnetic state.

$$\chi = \frac{C}{(T+\theta)} \qquad \textbf{1.16.}$$

Plotting $1/\chi$ vs. T will produce an overall linear fit of the high temperature limit with slope 1/C and have a positive or negative y-intercept indicating antiferromagnetic or ferromagnetic overall exchange respectively (figure 1.6).. Characteristic χ vs. T plots for a paramagnet, antiferromagnet and ferromagnet are shown in figure 1.6.

Cooperative magnetism is the result of interactions between ions with unpaired valence electrons . These interactions can either be classified as direct or indirect. Direct interactions result from orbital overlap of magnetic ions whereas indirect interactions involve mediating non-magnetic ions such as oxide (O^{2-}) in transition metal oxides. Goodenough and Kanamori established a set of rules that allow for qualitative prediction

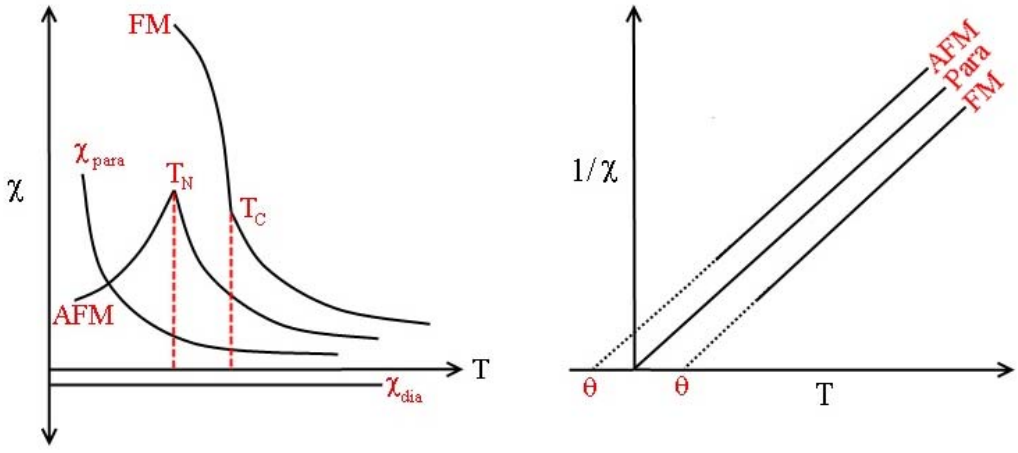

Figure 1.6. Left – General magnetic susceptibility trends for a paramagnet, antiferromagnet (AFM), ferromagnet (FM) with transition temperatures indicated. Right – Curie plot for a paramagnet and Curie-Weiss plots for AFM and FM showing the positive and negative y-intercept respectively.

of the nature of magnetic coupling (e.g. ferromagnetic, antiferromagnetic) based on magnetic ion electron configuration and the orientation of interacting orbitals.[4,5,6]

The most common types of indirect interactions are double exchange and super exchange. Double exchange is observed between two magnetic centers of differing oxidation state (e.g. Mn^{3+}/Mn^{4+}) mediated by non-magnetic oxygen.[7,8] The interaction can be described as a redox process where the more electron rich center (Mn^{3+}) effectively transfers an electron to O^{2-} creating a hopping effect resulting in O^{2-} reducing Mn^{4+} to Mn^{3+} (figure 1.7). This interaction results in antiferromagnetic coupling when the interacting d-orbitals are oriented at 180^{o}. Super exchange is an interaction which occurs between magnetic centers of identical electron content (e.g. Mn^{4+}/Mn^{4+}).[9,10,11] This interaction effectively involves a single electron transfer from an oxygen 2p orbital to each d-orbital equivalent to $1e^{-}$ reduction of the magnetic centers (figure 1.8).

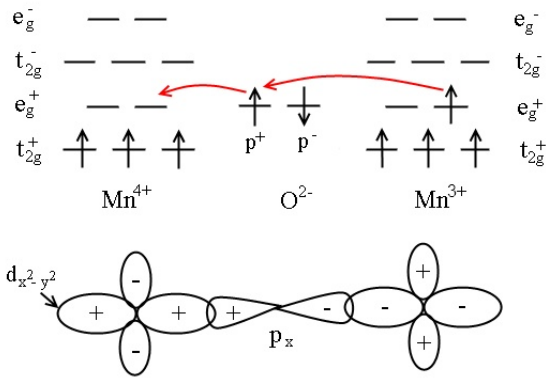

Figure 1.7. Double exchange mechanism for 180° interaction between a d-orbital mediated by an oxygen 2p orbital. Notation (+) and (-) for t_{2g} and e_g indicates spin up and down electrons respectively.

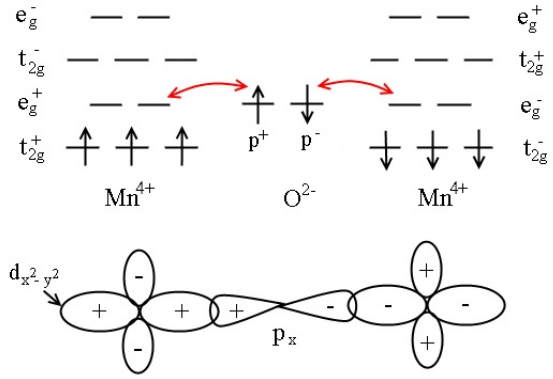

Figure 1.8. Super exchange mechanism for 180° interaction between a d-orbital mediated by an oxygen 2p orbital. Notation (+) and (-) for t_{2g} and e_g indicates spin up and down electrons respectively.

This interaction results in ferromagnetic coupling for interactions where the d-orbitals are oriented at 180°. Detailed evaluation of magnetic interactions is beyond the scope of this research and thus only the simplest forms of super exchange and double exchange have been mentioned.

1.4.3. SQUID Magnetometer

A SQUID magnetometer allows for examination of magnetic properties including magnetization and magnetic susceptibility using a programmable sequence of heating or cooling (2-400K) and application of a magnetic field (0±7T). Resultant data can be used to evaluate magnetic transition temperatures (e.g. T_N, T_C) and for determination of the materials magnetic moment. Additionally inspection of a material's magnetization as a function of applied magnetic field allows for understanding of a ferromagnetic materials hysteresis. The fundamental operation of this instrument is based on two superconducting loops. The first loop is a superconducting magnet which can operate between 0±7T. The second loop contains a SQUID (Superconducting Quantum Interference Device) which contains highly sensitive Josephson junctions and is coupled to a gradiometer. A sample transport system allows for the sample to be moved through the detection coil and as a result the magnetic moment of the sample induces an electric current in the gradiometer coil which results in a voltage output from the SQUID proportional to the magnetic moment as shown in figure 1.9.

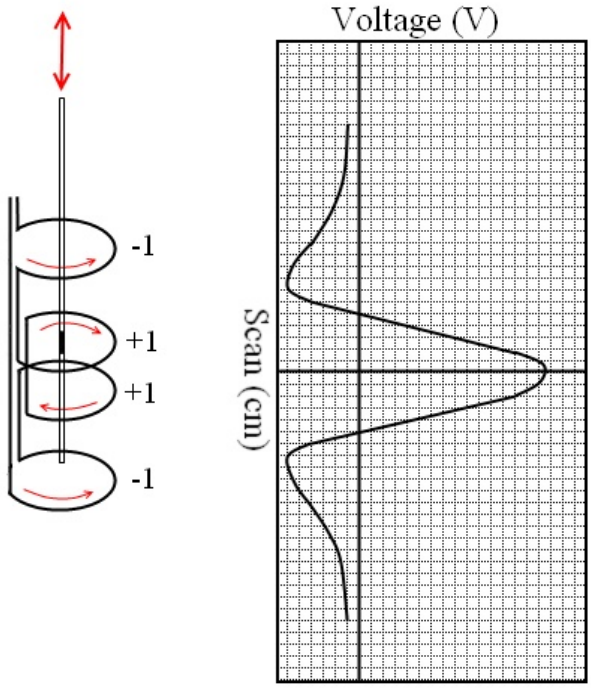

Figure 1.9. Left – Sample movement through the gradiometer with (+1) and (-1) indicating the direction of the coil windings. Right – A representation of the voltage function expected as a function of scan position for a secondary gradiometer.

Part II – Literature Review and Motivation for Project

1.5. Transition Metal Oxides

Transition metal oxides are host to a diverse array of magnetic, electronic, optical, thermal and mechanical properties. These properties can be appreciated on a much deeper level by studying a material's structure-property relationship. In the case of a crystalline material this may involve characterization using diffraction techniques (e.g. X-rays, neutrons, electrons) which can be utilized to provide both structural and property information, including additional property measurement techniques such as thermal analysis, magnetometry, conductivity or mechanical testing. An obvious motivation for understanding structure-property relationships is seen from applications which are observed in daily life such as energy (e.g. photovoltaics, batteries) or data storage (e.g. hard drives) materials as well as many components in modern electronic devices. It should however be realized that much academic research is driven by the intriguing challenge to understand material structure and properties from a fundamental perspective and that this is important for continued scientific progress. Another fundamental importance is the ability to synthesize novel materials. Conventional crystalline transition metal oxides typically result from high temperature (>1000^{o}C) preparation methods. However, advances in experimental techniques allow for progress from thermodynamically controlled synthesis to low temperature kinetically controlled approaches which mirror molecular synthesis. Thus there is very close connectivity between the method used to process a material, the resultant structure-property relation and ultimately potential applications.

1.6. Low Temperature Topotactic Solid-State Chemistry

The fundamental interest in low temperature solid-state chemistry for extended solids is to gain insight into reaction mechanisms and enhance control over product formation under kinetic restrictions. Beginning in the mid 1960's the concept of 'soft chemistry' techniques began and has grown to be governed by two basic principles (i) reactions are carried out at low temperatures (<500^{o}C) and (ii) the final product retains significant connectivity from the starting material making the reactions topotactic in nature.[12] The first reactions of this type were dominated by ambient electrolytic solid-solution reactions involving insertion of solution phase metal cations (alkali, alkali-earth, rare-earth) between the carbon sheets of graphite.[13] This work marked the beginning for redox intercalation reactions which was expanded to intercalation of a variety of cations and molecules into layered chalcogenides (MX_2, M=metal, X=chalcogen).[14,15] In 1977 Murphy characterized reversible solid-solution redox intercalation-deintercalation of VS_2 with lithium (Li_xVS_2).[16] Following the establishment of redox induced intercalation-deintercalation reactions in 1980 was hydration/dehydration reactions which also satisfied requirements (i, ii).[17] A good example of this technique is shown for potassium tetratitanate in figure 1.10. Stirring $K_2Ti_4O_9$ in water for 3 days produces hydrated/protonated phases $K_{2-x}H_xTi_4O_9{\cdot}nH_2O$ ($0<x<2$; $n<x$) with stoichiometry x depending on solution pH and temperature.[17,18] Dehydration of $KHTi_4O_9{\cdot}nH_2O$ ($n<1$) by heating at 500^{o}C results in the production of $K_2Ti_8O_{17}$ which is topologically related to $K_2Ti_4O_9$. $K_2Ti_4O_9$ has a structure composed of edge sharing TiO_6 octahedra sections connected by 3 corners, with potassium ions between the sheets.[17] The structure of

$K_2Ti_8O_{17}$ differs only by the presence of 4 corner sharing positions between the edge sharing octahedra sections to produce a staggered pattern.

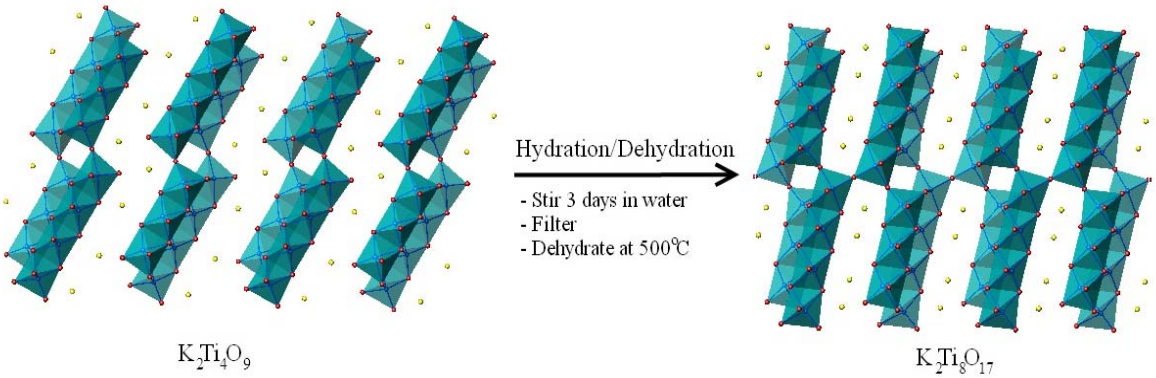

Figure 1.10. Hydration/dehydration applied to monoclinic [a = 18.98Å, b = 3.776Å, c = 12.05 Å, β = 106.8°] $K_2Ti_4O_9$ producing monoclinic [a = 15.678(2)Å, b = 3.775(1)Å, c = 11.951(1)Å, β = 95.67] $K_2Ti_8O_{17}$. Both crystal structures are described by space group C2/m. Red – oxygen, blue – titanium, yellow – potassium. Turquoise TiO_6 octahedra.[19,20,21]

Solid-solid topotactic reductions were first carried out in the mid 1990's using electropositive metals (e.g. Al, Zr) as reducing agents.[22,23] Although these were topotactic reactions they still required relatively high reaction temperatures (~500-900°C) thus not fulfilling requirements i, ii for an ideal soft chemistry technique. Sealing a sample of the rhombohedral perovskite $LaNiO_3$ with Al powder in an evacuated ampoule and heating (850-950°C, 16hr) produced a variety of oxygen defect $LaNiO_{3-x}$ ($0.08<x<0.5$) phases.[22] Reaction temperatures and aluminum concentration determined the final product stoichiometry. The first publication involving the use of a metal hydride (NaH) reducing agent was reported by Hayward in 1999.[24] This work described the reaction of a 2-fold stoichiometric excess of NaH reacted with $LaNiO_3$ in a sealed evacuated ampoule at ~200°C for 3 days to produce the infinite layer (Ni-square planar coordination) tetragonal

$LaNiO_2$ oxygen defect perovskite.[24] This solid-solid reduction method is superior to the metal (Al) reduction approach in terms of low temperature reactivity and reduction control as the entire $LaNiO_{3-x}(0.5<x<1)$ was characterized. This work marked the beginning for the use of metal hydrides as solid state reductants and resulted in many successful works over the following decade which demonstrates new levels of mechanistic control in solid-state chemistry.

1.7. The Hydride Anion

The hydride anion (H^-) is among the simplest in the periodic table having only one proton and two electrons which results in many of its interesting properties. The minimal nuclear charge present to attract the $1s^2$ electrons results in extensive polarizability of the valence electrons. This can present challenges in characterizing the ionicity or covalency of metal-hydride bonds. Metal hydrides of groups I and II are generally considered to be ionic hydrides with H^- becoming increasingly more ionic moving down the groups. Magnesium and beryllium have electronegativities comparable to that of transition metals and are often grouped among transition metal hydrides due to increased covalency.[25] The 4 crystal structures common to group I and II metal hydrides are shown in figure 1.11. Group I metal hydrides crystallize in the rock salt structure while CaH_2, SrH_2, BaH_2 crystallize in the cobalt silicide structure. MgH_2 forms the rutile structure type and BeH_2 an orthorhombic structure containing corner sharing BeH_4 tetrahedra.

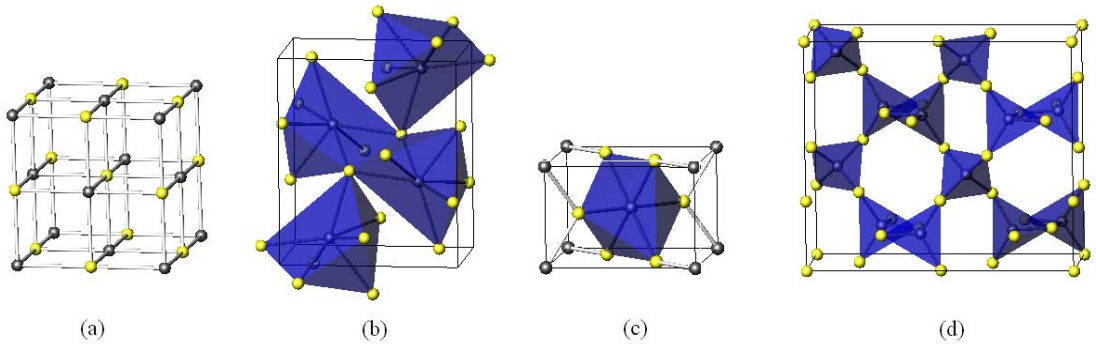

Figure 1.11. Cubic (*Fm-3m*) rock-salt structure LiH, NaH, KH, RbH, CsH (a) orthorhombic (*Pnma*) $CoSi_2$ structure CaH_2, SrH_2, BaH_2 (b) tetragonal *($P4_2/mnm$)* rutile structure MgH_2 (c) orthorhombic (*Ibam*) BeH_2.[26,27,28,29,25]

Properties of several group I and II metal hydrides relevant to this research are shown in table 3.4. Properties such as cation electronegativity, enthalpy of formation (ΔH_f^o) and decomposition temperature (T_{dec}) are important indicators of metal hydride stability and reactivity (table 3.4).[30] Decomposition of metal hydrides takes place according to equation 1.17.

$$MH_{x(s)} \rightarrow M_{(s)} + {}^{x}/_{2}\, H_{2(g)} \qquad \textbf{1.17.}$$

There is generally close correlation between metal hydride enthalpy of formation (ΔH_f^o) and decomposition temperatures (table 3.4). There is a less easily distinguishable relationship to cation electronegativity such that more highly ionic M-H bonds are stronger and typically have higher T_{dec} values and more highly negative enthalpies of formation. Another interesting relationship is that of cation electronegativity to the effective H^- radius with the H^- radius generally increasing as the bond becomes more ionic. This is easily observed from the H^- radius of 1.47Å and 1.30 in NaH and MgH_2 respectively (table 3.4). These radii are comparable to those of more electron rich

halogens such as Cl^- and F^-.[31] The polarizability and degree of ionic character for the M-H bond is relevant to current uses of the hydride ion as a solid state reductant.

1.8. Metal Hydride Reductants

Prior to discussing current literature focusing on the use of metal hydrides to reduce transition metal oxides it should be realized that such reductants have been used in organicsynthesis since the 1940's.[32,33,34] The role of metal hydride reductants in organic chemistry will briefly be considered. Over the last 70 years a vast amount of knowledge has been gained to establish reaction conditions (e.g. metal hydride, solvent, temperature) that can be used to reduce targeted functional groups in complex molecules. A selection of metal hydrides are used in organic chemistry with alkali borohydrides (e.g. $NaBH_4$), alkali aluminum hydrides (e.g. $NaAlH_4$) and metal alkoxyaluminum hydrides [e.g. $LiAlH_3(OCH_3)$] being among the most common.[35,36] Typically these reactions proceed mechanistically with the hydride anion attacking the most positive atom of a functional group (e.g. carbonyl carbon). Many interesting comparisons can be made between this work with the future for metal hydrides as solid state reductants. A common goal among both inorganic solid state chemists and organic chemists is the desire to carry out step-wise mechanistically controlled reactions. Such a synthetic approach for solid state inorganic synthesis is inherently kinetically hindered. Also the lack of specific functional groups further complicates the potential for a step-wise approach in the solid state. It should not be forgotten however that 70 years ago organic chemists faced a similar synthetic challenge.

The suitability of metal hydrides as low temperature solid state reductants is explained by the highly negative standard redox potential estimated at -2.25V for the H_2/H^- couple (table 1.1).[31] This value is comparable to the high reduction potential of many electropositive group I and II metals. Therefore H^- is more reactive at low temperatures than conventional gas reductants such as CO and H_2 which can require temperatures in excess of 1000°C. In addition to the favorable reduction potential of H^- its high polarizability is anticipated to be favorable during ion diffusion.

Table 1.1. Standard reduction potentials (E^o) for select group I, II elements and conventional gas reductants.[31,37]

Redox Couple	Standard Reduction Potential, E^o (V)
Li/Li+	-3.05
Mg/Mg^{2+}	-2.37
$H_2/2H^-$	-2.25
CO_2/CO	0.104
$2H^+/H_2$	0

The past 12 years of literature supporting the use of metal hydrides to reduce transition metal oxides has focused exclusively on the use of NaH, LiH and CaH_2 reductants.[24,38,39,40] This technique has allowed for the synthesis of many novel oxygen defect phases from a variety of structures and starting materials. The majority of known reduced oxygen defect structures are manganate, cobaltate and ferrate materials. Common starting material structures for reduction include perovskite structures (e.g. ABO_3: $SrFeO_3$[41], $La_{1-x}Sr_xMnO_3$[42], $NdNiO_3$[43], $BaMnO_3$[39], $YMnO_3$[44], $Ba_{0.5}Sr_{0.5}MnO_3$[40]), 2-dimensional perovskite structures (e.g. A_2BO_4: $La(Sr,Ba)MnO_4$[45], $LaSrCoO_4$[46],

$A_3B_2O_7$: $YSr_2Mn_2O_7$[47], $Sr_3Fe_2O_7$[48], $Sr_3Co_2O_7$[49]) and other structure types including pyrochlore $Y_2Ti_2O_7$ [50]), oxyhalide $Sr_3Fe_2O_5Cl_2$[51] and $Sr_7Mn_4O_{15}$ [52,53] Perovskite related structures (ABO_3, A_2BO_4) have been highly successful in producing unique oxygen defect structures. The synthesis of these phases demonstrates a level of synthetic and mechanistic control unattainable using conventional high temperature methods. Topotactic reduction of transition metal oxides allows for tuning of the transition metal oxidation state and oxygen vacancy pattern. This is a powerful tool to control transition metal electronic configuration and the magnetic exchange interactions present via oxygen bonding. Thus metal hydride reductions are an effective method to access novel magnetic structures and to modify electronic and magnetic properties.

To emphasize the capability of metal hydride reductants some recent successful reductions from literature will be discussed. Among the most interesting reduction products recently is that of ferrate materials. The literature clearly shows that in nature and under synthetic conditions the presence of square planar Fe^{2+} is very rare with only the mineral gillespite ($BaFeSi_4O_{10}$) containing Fe^{2+} in a truly square planar coordination.[54] Recently metal hydride reductions have allowed for controlled reduction of ferrates such as $Sr_3Fe_2O_5Cl$ and $SrFeO_3$ to phases containing square planar Fe^{2+} (figure 1.12).[51,41] The n = 2 Ruddlesden-Popper phase ferrate oxyhalide $Sr_3Fe_2O_5Cl_2$ contains apex sharing iron (Fe^{3+}) square based pyramids. Reduction with LiH at 350^{o}C results in deintercalation of the apex sharing oxygen producing square planar Fe^{2+} layers. This example is particularly interesting as it also shows that metal hydrides can selectively reduce multi-anion (oxyhalide) materials. Original work by Tsujimoto showed that the

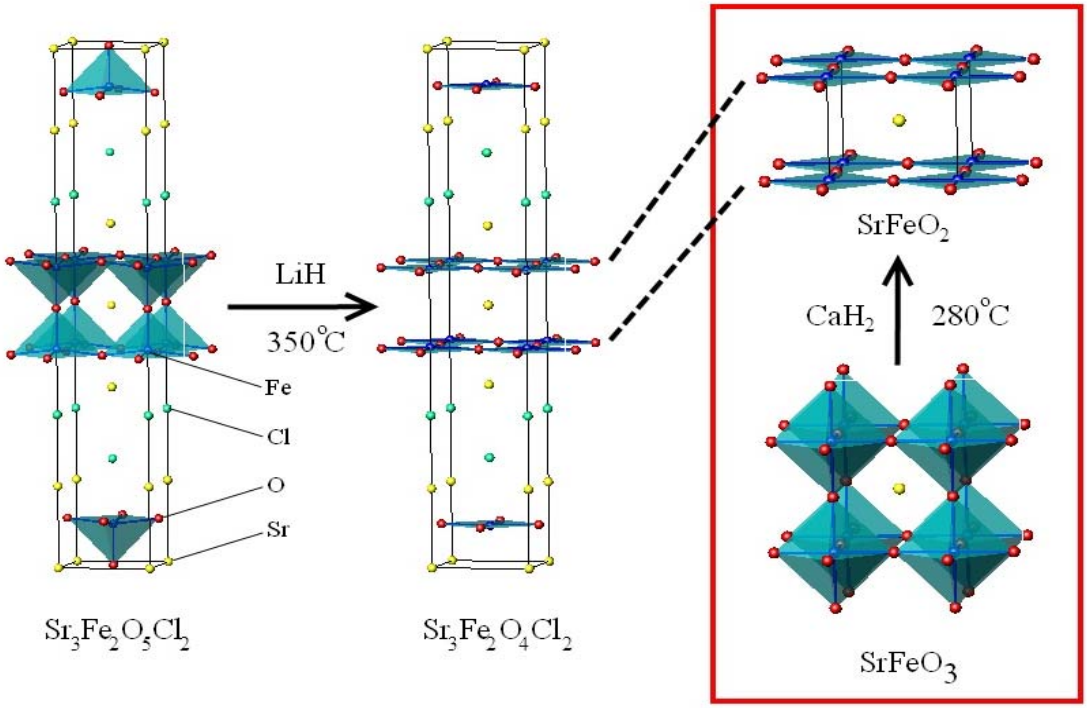

Figure 1.12. Reduction of tetragonal $Sr_3Fe_2O_5Cl_2$ (*I4/mmm*) to $Sr_3Fe_2O_4Cl_2$ with LiH at 350°C (4x24hr). Red inset – reduction of cubic $SrFeO_3$ (Pm3-m) to tetragonal $SrFeO_2$ (*P4/mmm*) with CaH_2 at 280°C (7 days).

three dimensional perovskite $SrFeO_3$ containing corner sharing Fe^{4+} iron octahedra can be reduced using CaH_2 at 280°C in which apical oxygen are deintercalated to again produce the infinite layer structure. A second example is the reduction of $BaMnO_3$ to $BaMnO_2$ using LiH at 350°C (figure 1.13).[39] $BaMnO_3$ is a hexagonal perovskite containing face sharing octahedra (Mn_2O_9 units) which share corners. Reduction results in an ordered deintercalation of oxygen producing edge sharing tetrahedra (Mn_2O_6 units) sharing corners with corner sharing tetrahedra (Mn_2O_7 units). This example demonstrates the deintercalation of oxygen from face sharing positions. It is anticipated that the location of oxygen vacancies in metal hydride reduction products is largely dependent on structure.

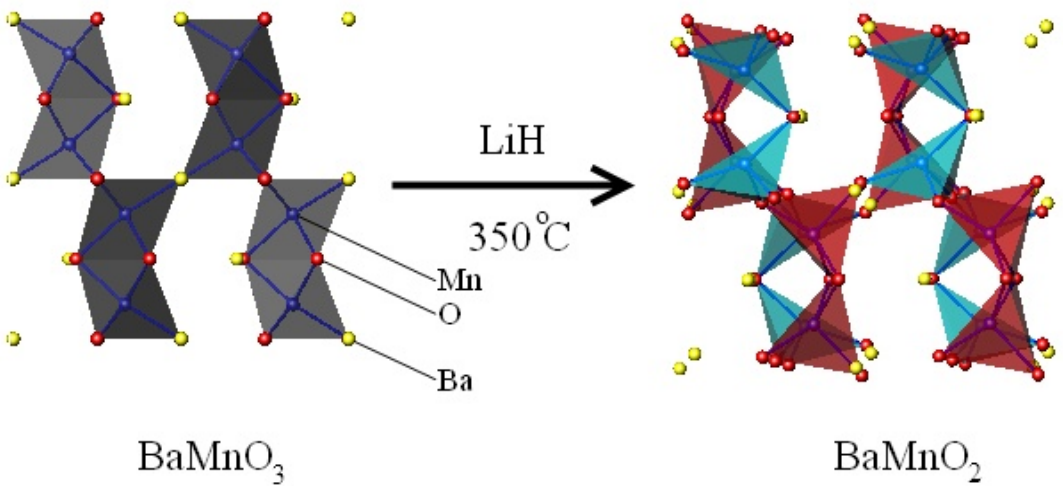

Figure 1.13. Reduction of hexagonal $BaMnO_3$ (*$P6_3/mmc$*) to orthorhombic $BaMnO_2$ (*Pnma*) with LiH at 350°C (2days). Gray Mn_2O_9 units, red Mn_2O_6 units, aqua Mn_2O_7 units.

1.8.1. Reduction/Insertion Reactions

A technique which has followed from the success of metal hydride reductions is the reduction/insertion reaction. Transition metal oxide electronic and magnetic properties are heavily dependent on the metal-oxygen-metal interaction.[55] Thus oxygen defect structures from metal hydride reduction provide an opportunity for insertion of a secondary anion which may significantly alter the materials magnetic and electronic properties. Current literature has demonstrated the ability to insert H^- and F^- into phases previously reduced using metal hydrides to produce oxide-hydrides and oxide-fluorides respectively. Transition metal oxide-halides have been well characterized in literature with products resulting from conventional high temperature (T >800°C) reactions. However often the halide anions in these structures (e.g. $Sr_3Fe_2O_5X_2$ [X = Cl,Br], $Sr_3Co_2O_5Cl_2$, Sr_2MO_3Cl [M = Co,Mn], $Sr_4Mn_3O_8Cl_2$) do not take part in transition metal bridging interactions.[56,57,58,59] This can be readily seen by inspection of $Sr_3Fe_2O_5Cl_2$ in

figure 1.12 where apical chloride anions do not bridge Fe^{3+} cations. Oxide-hydrides in comparison to oxide-halides have not been explored in literature using conventional high temperature methods. This is due to the inherent challenge to avoid reduction using H^- and due to the thermal instability of hydride anions.

Hayward has demonstrated the ability to carry out a metal hydride reduction of $Sr_7Mn_4O_{15}$ followed by fluorination to yield $Sr_7Mn_4O_{13}F_2$ (figure 1.14).[53] $Sr_7Mn_4O_{15}$ crystallizes in a monoclinic (*P2₁/c*) unit cell with face sharing MnO_6 octahedra (Mn_2O_9 units).[60] Reduction with CaH_2 at 300°C (2days) results in deintercalation of the corner sharing O^{2-} of the Mn_2O_9 units producing $Sr_7Mn_4O_{13}$ which contains isolated Mn_2O_7 units. It should be contrasted that the reduction of $BaMnO_3$ which also contained Mn_2O_9 units resulted in deintercalation of face sharing oxygen atoms. Stoichiometric fluorination

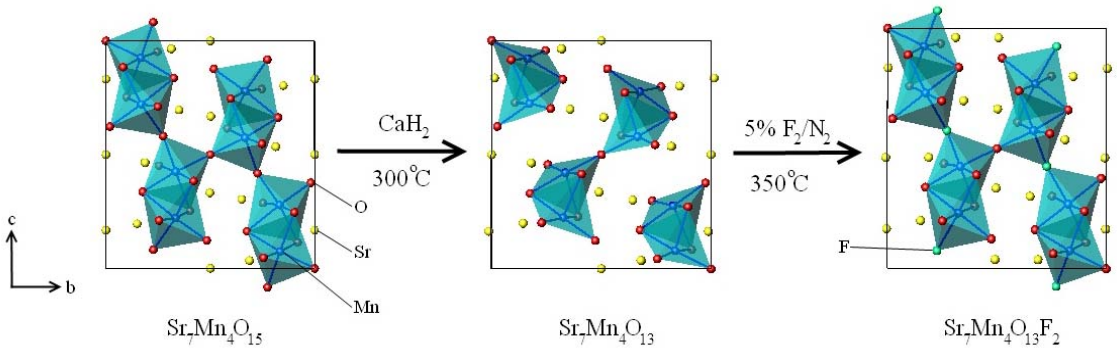

Figure 1.14. Topotactic reduction/fluorination of monoclinic (*P2₁/c*) $Sr_7Mn_4O_{15}$ to yield $Sr_7Mn_4O_{13}F_2$.

of the reduced phase required heating $Sr_7Mn_4O_{13}$ in static F_2/N_2 at 350°C producing monoclinic (*P2₁/c*) $Sr_7Mn_4O_{13}F_2$. It is clear in figure 1.14 that $Sr_7Mn_4O_{13}F_2$ unlike $Sr_3Fe_2O_5Cl_2$ (figure 1.12) contains fluoride anions that act to bridge the transition metal ($Mn^{3+/4+}$).

The most interesting materials in current literature resulting from the reduction/insertion approach are transition metal oxide-hydrides. Low temperature reactions of certain cobalt oxide phases with metal hydrides have occasionally been shown to produce oxide-hydrides under carefully controlled reaction conditions. There is currently no generic procedure that can be followed to produce oxide-hydrides using metal hydrides as this synthetic chemistry is in its infancy. $LaSrCoO_3H_{0.7}$ was the first reported oxide-hydride synthesized using metal hydrides.[46] Its synthesis required the same method used in literature to carry out metal hydride reductions. Tetragonal $LaSrCoO_4$ was heated in a sealed evacuated environment with CaH_2 at 450^{o}C to produce orthorhombic $LaSrCoO_3H_{0.7}$ (figure 1.15.).[61] Figure 1.15 shows that deintercalation of equatorial oxygen atoms in sheets parallel to the c-axis have been replaced with hydride anions. The O^{2-} and H^- strongly couple $Co^{1+/2+}$ giving rise to an antiferromagnetic ordering temperature significantly above room temperature (T_N=350K). This transition temperature is comparatively high considering $LaSrCoO_{3.5}$ has a Néel temperature of 110K.[62] Further study has characterized the in-situ formation of this phase and presented detailed analysis of the electronic properties.[63] Following this work several $LnSrCoO_{3+x}H_y$ (Ln = Pr, Nd; $0.08<x<0.21$; $0.58<y<0.80$) phases have also been synthesized and show a dependence of H^- insertion on the presence of H_2 pressure (p = 9-18atm).[64] The hydride anions in the orthorhombic (*Immm*) $PrSrCoO_{3.16}H_{0.68}$ phase occupy equatorial positions to produce a structure very similar to $LaSrCoO_3H_{0.7}$ (figure 1.15). Antiferromagnetic ordering temperatures for these oxyhydride products ranged from 375-410^{o}C with values increasing with H^- stoichiometry. Most recently a partially reduced orthorhombic (*Immm*) $Sr_3Co_2O_{5.8}$ phase resulting from high temperature

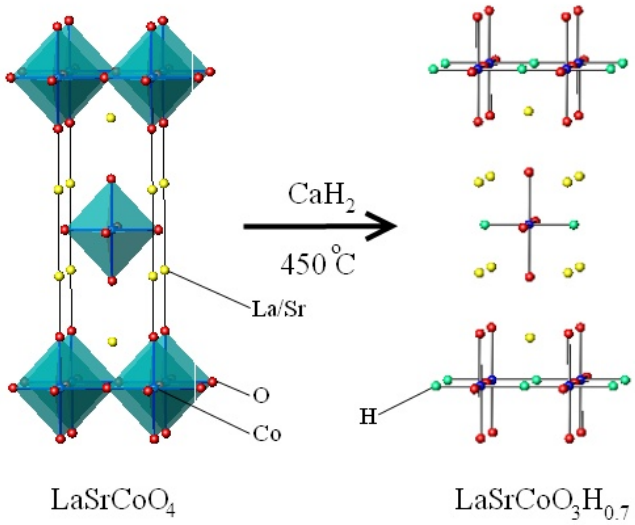

Figure 1.15. Topotactic reduction/hydride insertion of tetragonal (*I4/mmm*) $LaSrCoO_4$ with CaH_2 at 450°C (2x4days) to produce orthorhombic (*Immm*)$LaSrCoO_3H_{0.7}$.

synthesis was reacted with CaH_2 at low pressure with an elaborate heating procedure (24hr – 240°C, 2x24hr – 250°C, 24hr – 255°C) and regrinding between heating periods to produce a phase mixture including orthorhombic $Sr_3Co_2O_{4.33}H_{0.84}$ and a secondary partially reduced phase.[49] Consistent with the two other examples of oxyhydrides the hydride anions occupy equatorial positions however unexpectedly no transition to an ordered magnetic structure was observed. It is clear that oxyhydride materials are interesting however their exploration is currently limited by synthetic challenges. Metal hydrides appear to be a promising route to synthetic understanding.

1.8.2. Challenges and Limitations of Current Literature

As shown above the use of metal hydrides has introduced a revolutionary mechanistic approach to solid state reductions/insertions. Current literature is successful in characterizing many novel structures using this technique. However current literature

lacks proof of the solid state metal hydride reduction mechanism and assessment of metal hydride reactivity. Addressing these two issues will be essential for continued development of this chemistry. The conditions in which metal hydride reductions take place are complex and understanding the influence of reductants such as H_2 and gas phase equilibria/pressure is important for a more detailed understanding of the reaction mechanism. Knowledge of metal hydride reactivity as reductants is essential as current literature provides no rational for the choice of reductant used.

1.9. Manganates

1.9.1. The Perovskite Structure

The perovskite structure with general formula ABX_3 originates from the mineral perovskite, $CaTiO_3$.[65] $CaTiO_3$ was initially published as a cubic perovskite structure with space group *Pm-3m* made of corner sharing BO_6 octahedra with a central 12-coordinated AO_{12} polyhedron (figure 1.16). The majority of perovskite structures however are not

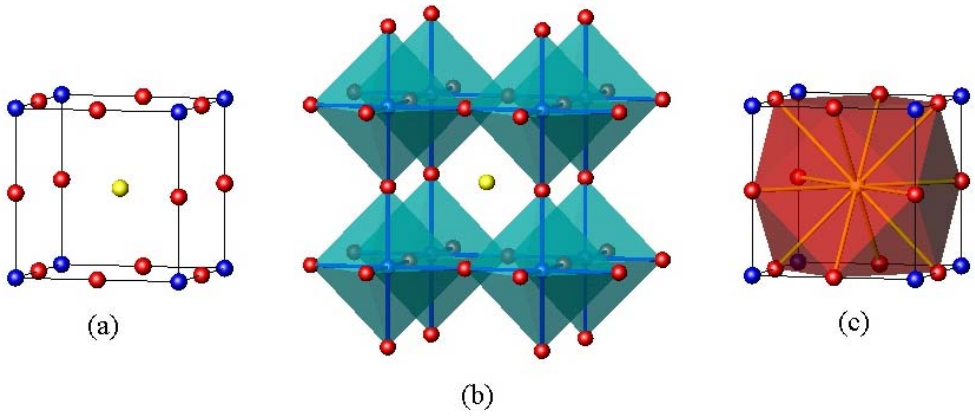

Figure 1.16. The ideal $CaTiO_3$ cubic (*Fm-3m*) perovskite structure showing the unit cell contents (a) corner sharing TiO_6 octahedra (b) CaO_{12} polyhedra. Red – oxygen, blue – titanium, yellow – strontium.[65]

cubic and instead crystallize in lower symmetry lattices due to structural distortions.[66] It turns out that $CaTiO_3$ is indeed an orthorhombic perovskite.[67] Goldschmidt developed a tolerance factor (equation 1.18) that allowed for insight into the type of perovskite that a given ABX_3 phase may adopt based on ionic radii (R – respective ionic radii).[68]

$$t = (R_X + R_A) / \sqrt{2}(R_X + R_B) \qquad \textbf{1.18.}$$

Tolerance factors of $t \approx 1$ are most stable and most likely to crystallize in a cubic perovskite indicating that the A-X bond distance $\sim\sqrt{2}$ times larger than the B-X bond distance creating the ideal cubic condition. Tolerance factors <1 indicate that cation B is relatively too large in comparison to cation A which often results in buckling/tilting of octahedra to optimize A-cation bonding. A tolerance factor >1 implies that the A cation is too large relative to the B-cation and puts the octahedral connectivity under tension which in turn can cause octahedral distortions and cation displacements. Distortions in non-cubic perovskites are generally the result of octahedral rotation/tilting or octahedral distortion due to Jahn-Teller effects.[69,70] A significant amount of literature is dedicated to describing distortion geometries of non-cubic perovskites and the development of relationships between distortion observed and structure symmetry.[71]

1.9.2. K_2NiF_4 Structure Series

The K_2NiF_4 structure was first reported by Balz in 1953.[72] Later in 1955 several isostructural A_2BO_4 phases were reported including Sr_2TiO_4 and Sr_2MnO_4.[73] The A_2BO_4 crystal structure is shown in figure 1.17 having a tetragonal cell described with space group *I4/mmm*. This structure type contains 2-dimensional layers of corner sharing BO_6 octahedra separated by AO rock salt layers, thus making this a 2-dimensional layered

structure. As shown in figure 1.17 the rock salt intergrowth layers result in a reduction of A-cation coordination from 12 in the ideal cubic perovskite to 9 in the A_2BO_4 phase. It is important also to note the geometrical relationship between the rock salt (a_R) and ideal cubic perovskite (a_P) lattice parameters such that $a_R = \sqrt{2}a_P$ with (a) denoting the respective unit cell parameter. There have been a number of approaches to develop a tolerance factor for A_2BO_4 structures with less consistency in approach compared to that established by Goldschmidt for perovskites. Some works simply use the Goldschmidt formula developed for perovskites while analysis of cation ratios has also been proposed by Ganguli.[74,75] A more mathematically complex equation has also been proposed by Chen.[76] For purposes of this research a tolerance factor developed by Poix will be used which is shown in equation 1.19.[77] Here the tolerance factor t is calculated using β_B which is the sum of oxygen and B cation radii, and ψ_A can be found using equation 1.20 where V represents unit cell volume. K_2NiF_4 structures result when $1.02 < t_{poix} < 0.85$.[77]

$$t = \frac{\psi_A \sqrt{2}}{2\beta_B} \qquad \textbf{1.19.}$$

$$0.99615V^{1/3} = \beta_B + \psi_A \sqrt{2} \qquad \textbf{1.20.}$$

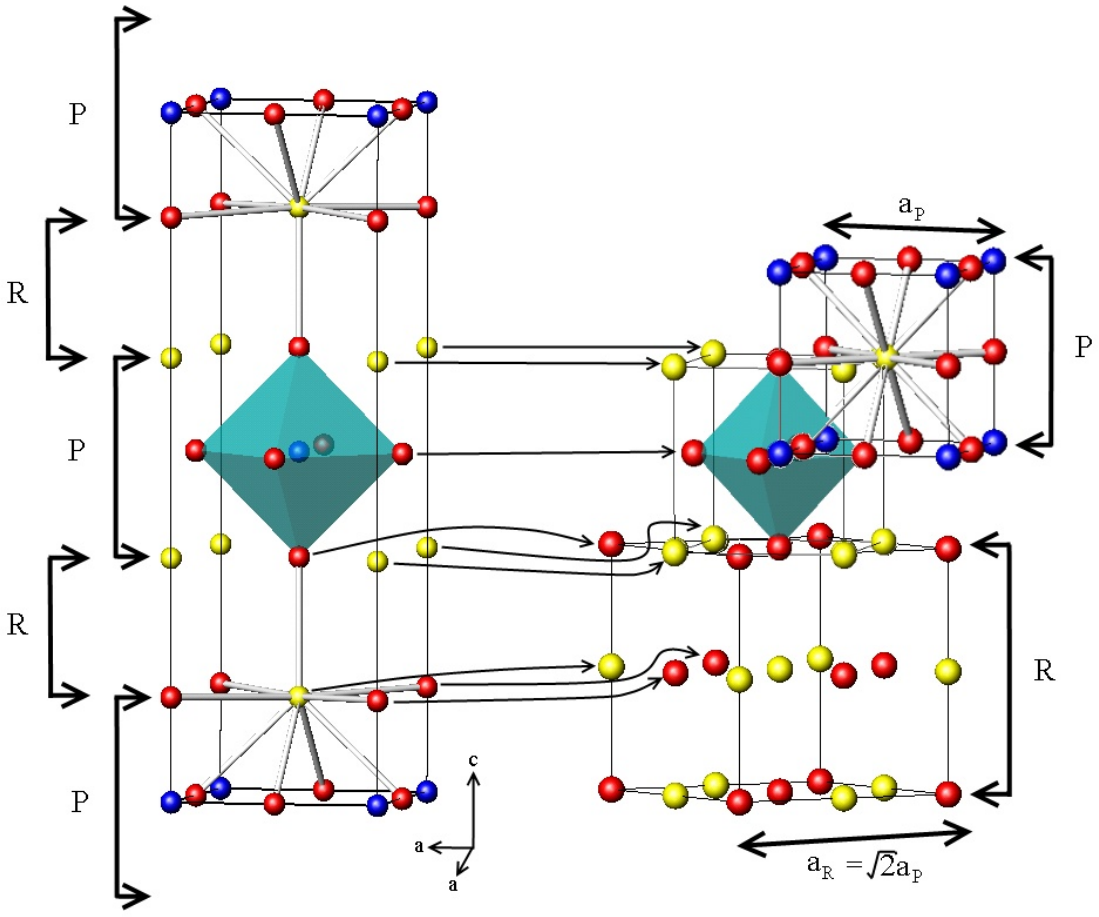

Figure 1.17. Structural description of the K_2NiF_4 (A_2BO_4) structure type. Left – A_2BO_4 structure containing perovskite and rock-salt layers. Right – emphasis of the origin and orientation of perovskite and rock-salt structural components. Red – fluorine, blue – B cation, yellow – A cation, turquoise BO_6 octahedra.[78,65,79]

1.9.3. Ruddlesden-Popper Series

In 1957 Ruddlesden and Popper began exploring further novel A_2BO_4 phases which led to the synthesis and characterization of novel $Sr_3Ti_2O_7$.[80,81] $Sr_3Ti_2O_7$ had a structure similar to that of the characterized A_2BO_4 phases with the exception that perovskite layers were double in thickness (figure 1.18b). Thus in this structure strontium atoms centered in the perovskite layers retain the SrO_{12} coordination while strontium atoms of the rock-salt layers have 9-fold coordination similar to A_2BO_4 phases. Ruddlesden and Popper established a structural trend among $SrTiO_3$, Sr_2TiO_4, $Sr_3Ti_2O_7$ and $Sr_4Ti_3O_{10}$ in 1963 by establishing the $A_{n+1}B_nO_{3n+1}$ series where n indicates the number of corner sharing perovskite layers to be separated by rock-salt layers.[82] The $Sr_{n+1}Ti_nO_{3n+1}$ series is shown in figure 1.18 for n = 1,2,3 and for the pure cubic perovskite end member (n = ∞). A particularly interesting feature of Ruddlesden-Popper (RP) structures is the flexibility in oxygen stoichiometry with several published oxygen deficient and excess phases. This observation is the result of interstitial tetrahedral (OA_4) oxygen vacancies in the rock-salt layers. This interstitial site has been characterized for $La_2NiO_{4.18}$ which contains occupied oxygen interstitial sites as shown in figure 1.19.[83] Excess oxygen occupying interstitial sites has also been characterized in $La_4Co_3O_{10.3}$.[84] Occupation of the interstitial site as shown for $La_2NiO_{4.18}$ in figure 1.19 is accompanied by localized displacement of adjacent NiO_6 apical oxygen sites to maximize their distance from the interstitial oxygen site. In addition to allowing for excess oxygen content, the interstitial sites provide a potential mechanistic advantage for oxide ion mobility. Thus in both partially reduced and fully or excessively oxidized phases oxide

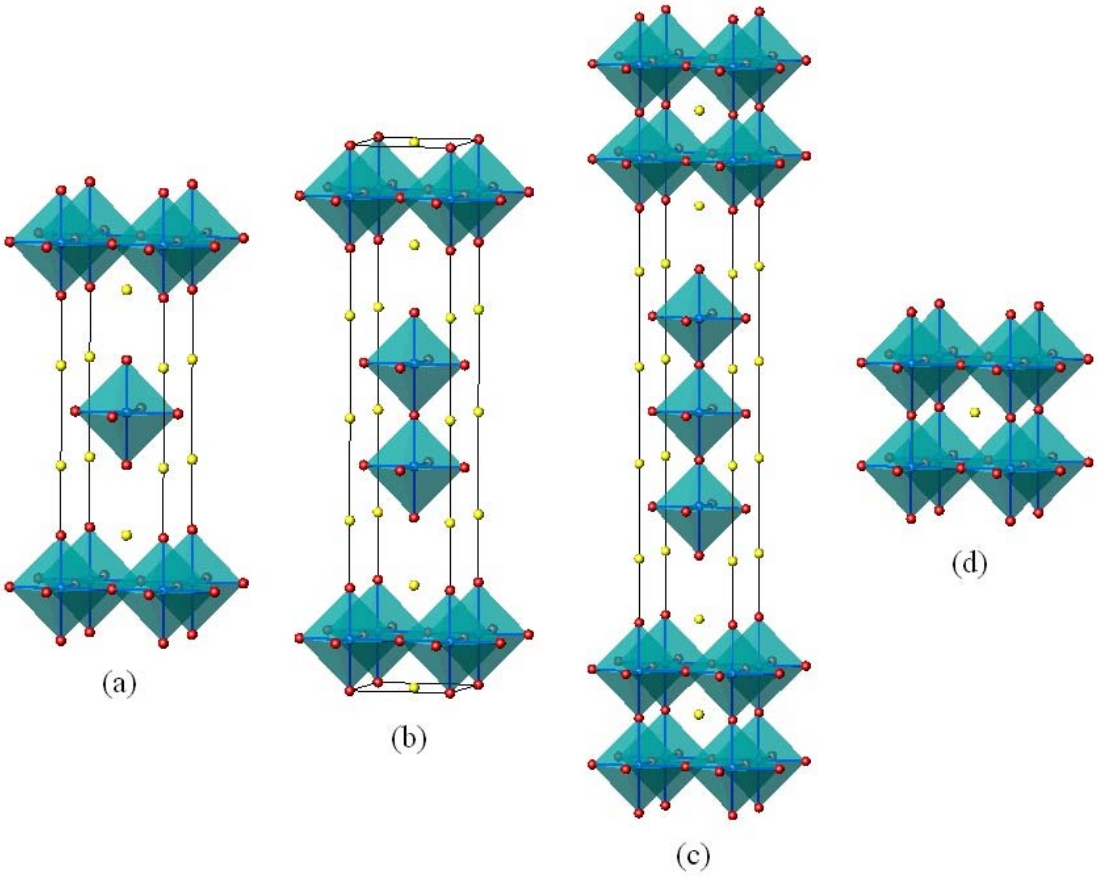

Figure 1.18. $Sr_{n+1}Ti_nO_{3n+1}$ Ruddlesden-Popper structure series. Sr_2TiO_4 [n = 1] (a), $Sr_3Ti_2O_7$ [n = 2] (b) $Sr_4Ti_3O_{10}$ [n = 3] (c) $SrTiO_3$ [n = ∞]. Blue – Ti, yellow – Sr, red – O.[78,81,82,65]

ion mobility may be contributed to by a vacancy mechanism, interstitial mechanism or a combination of both. Some studies of Ruddlesden-Popper phases have been reported focusing on oxide ion mobility and the mechanisms involved.[85,86,87,88]

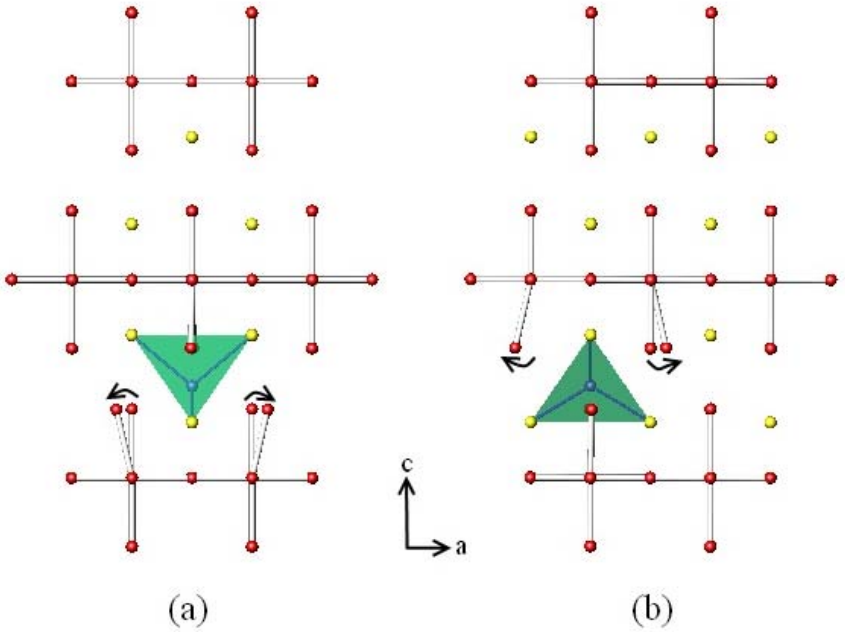

Figure 1.19. Illustration of $La_2NiO_{4.18}$ focusing on the light green tetrahedron outlining the location of an interstitial site (purple – interstitial oxygen, red – oxygen, yellow - La). Arrows are shown to indicate the local disorder resulting from occupation of an interstitial site. (a) and (b) differ by 90° rotation of the unit cell about the c-axis.[83]

1.10. $Sr_{2-x}Ca_xMnO_4$ (0<x<2) System

The $Sr_{2-x}Ca_xMnO_4$ (0<x<2) system is made of phases that crystallize in ideal and distorted n=1 RP phases dependent on composition (x).[89] Compositions of $x \leq 0.5$ such as Sr_2MnO_4 [a = 3.7907(3)Å, c = 12.4944(11)Å] crystallize in the ideal tetragonal cell with space group *I4/mmm* (figure 1.20).[90] Increased concentrations of calcium with $x > 0.5$ result in a cooperative rotation of the MnO_6 octahedra about the c-axis to more favorably

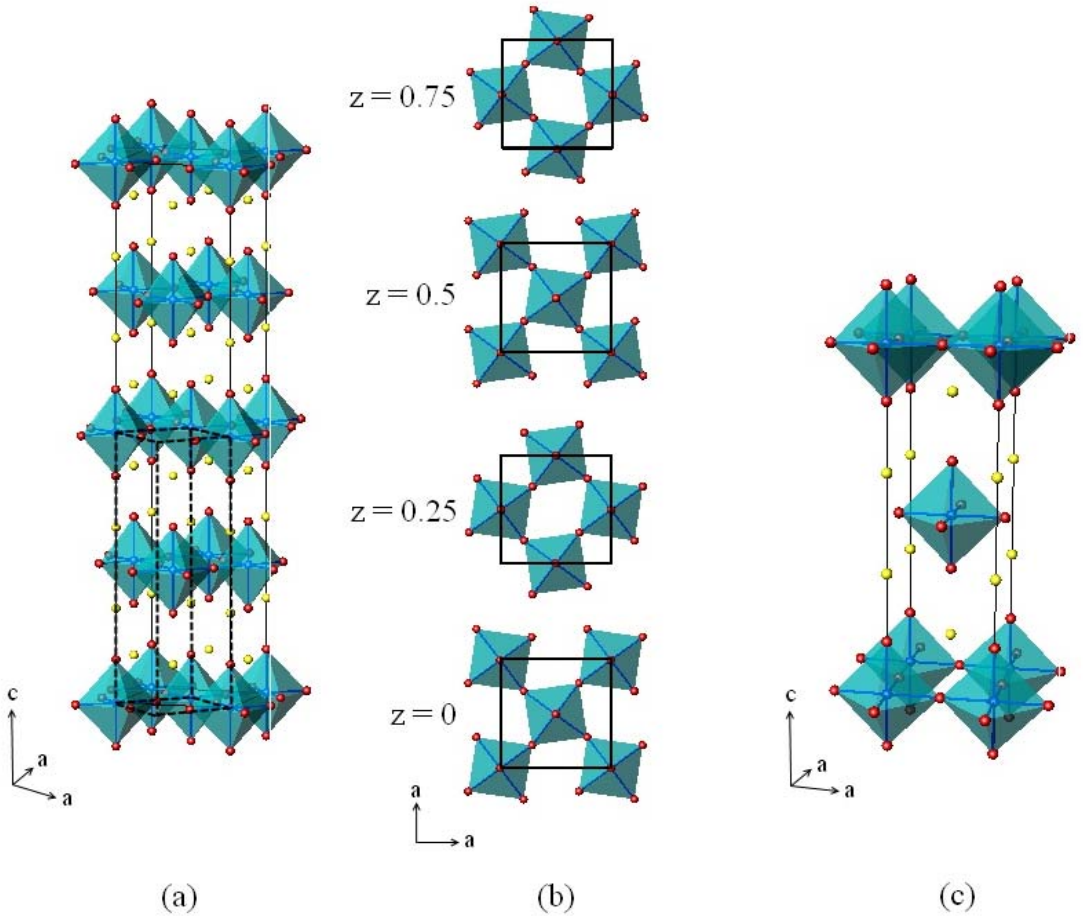

Figure 1.20. $Sr_{2-x}Ca_xMnO_4$ system - tetragonal (*I4/acd*) superstructure for compositions of x > 0.5 including the dashed ideal unit cell (a) superstructure cooperative rotation of MnO_6 octahedra about the c-axis as a function of the z-coordinate axis (b) ideal tetragonal (*I4/mmm*) for compositions of x≤ 0.5 (c).[89]

accommodate calcium in calcium rich members such as Ca_2MnO_4 [a = 5.183(1)Å, c = 24.117(4)Å] producing an n=1 RP tetragonal superstructure with space group I_1/acd.[91] The ideal tetragonal cell (a,c) is related to the super cell (a',c') such that $a' = \sqrt{2}a$ and $c' = 2c$ as can be depicted from figure 1.20a.[89]

1.10.1. $(Sr/Ca)_2MnO_{4-x}$ Phases

Beyond characterization of the $Sr_{2-x}Ca_xMnO_4$ ($0<x<2$) system there has been no reported work on reductions of the strontium-calcium solid solutions. However reduced phases of the end members Sr_2MnO_4 and Ca_2MnO_4 have been explored in literature using conventional methods including hydrogen reduction and single step high temperature synthesis. Figure 1.21 shows that Ca_2MnO_4, orthorhombic (*Pnma*) $CaMnO_3$ and cubic (*Fm-3m*) $SrMnO_3$ perovskite based phases can all be reduced using hydrogen gas to the same oxygen defect perovskite layer.[89,91,92,93,94] The oxygen defect layer consists of corner sharing square based pyramids (MnO_5) arranged in a 6-member elongated hexagon pattern.[93] Oxygen in these phases is removed from the equatorial positions of the original MnO_6 octahedra. Heating Ca_2MnO_4 in $10\%H_2$/He for >100hrs produces an orthorhombic [a = 5.30(1)Å, b = 10.05(1)Å, c = 12.24(1)Å] $Ca_2MnO_{3.5}$ phase having space group *Bbcm* (figure 1.21).[95,91] Higher reaction temperatures cause over-reduction to a Ca_2MnO_3 rock-salt structure. No intermediate Ca_2MnO_{4-x} ($0<x<0.5$) phases have been published. Since $Ca_2MnO_{3.5}$ is topologically related to the fully oxidized structure this makes Ca_2MnO_4 appealing for metal hydride reduction attempts aiming to access intermediate reduced phases. However the significant reduction of Ca_2MnO_4 in $10\%H_2$ at 300^oC is an indication that H^- will likely over-reduce the material at moderately low temperatures.

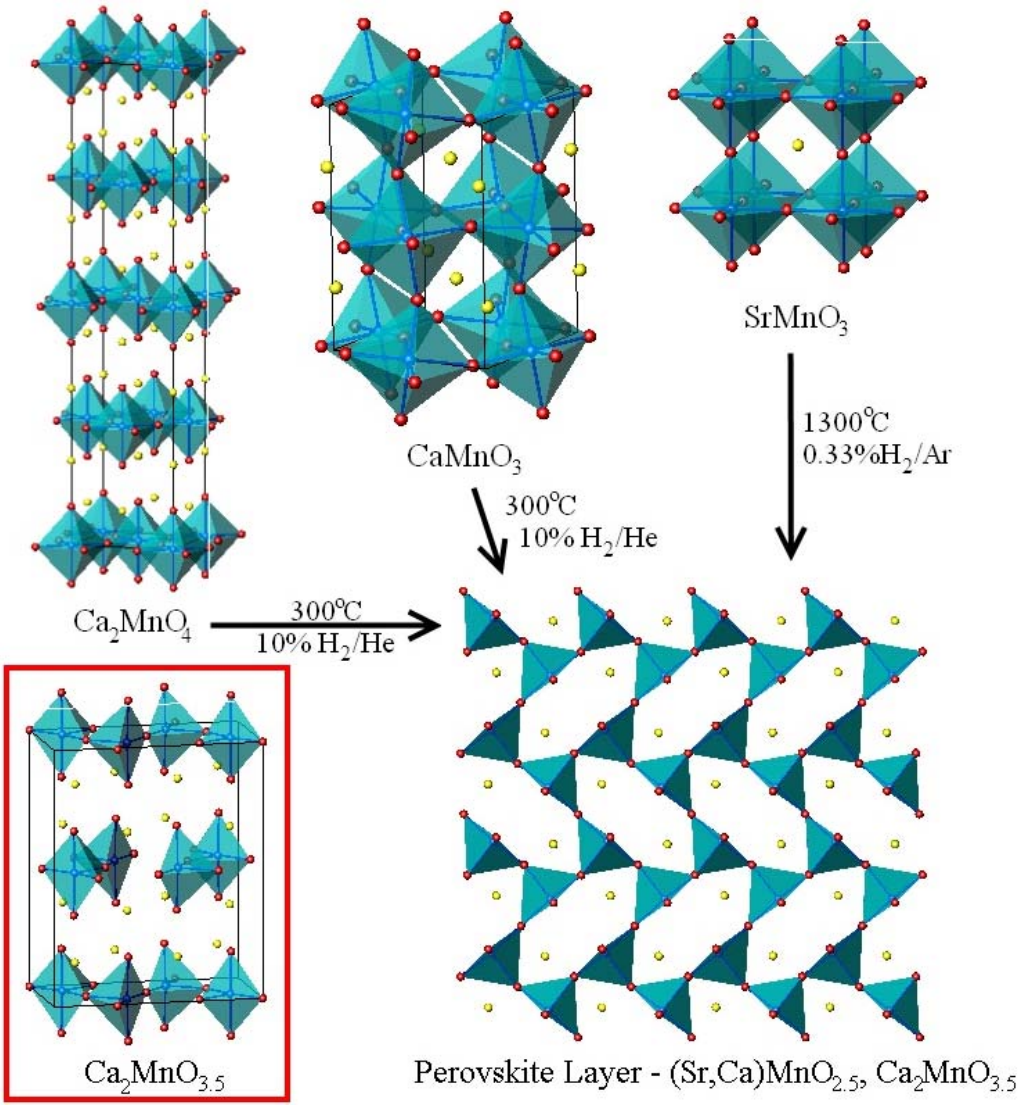

Figure 1.21. The topotactic reduction of Ca_2MnO_4, orthorhombic (Pnma) $CaMnO_3$, cubic (*Fm-3m*) $SrMnO_3$ to the common oxygen defect perovskite layer in $(Sr,Ca)MnO_{2.5}$ and $Ca_2MnO_{3.5}$. Outlined in red is the orthorhombic (*Bbcm*) $Ca_2MnO_{3.5}$ phase emphasizing the offset oxygen defect perovskite layers. [89,91,92,93,94]

Reduced phases of Sr_2MnO_4 are more common in literature than those of Ca_2MnO_4. Typically these phases have been produced using high temperature direct synthesis however gas reductants have also been used. There is no literature providing a systematic method for the synthesis of Sr_2MnO_{4-x} ($0<x<0.5$) phases. $Sr_2MnO_{3.84}$ has been reported by Kriegel to result from heating SrO and $Sr_7Mn_4O_{15}$ at 1500°C in argon for 1hr.[96] Additionally the synthesis of $Sr_2MnO_{3.71}$ required heating $MnCO_3$ and $SrCO_3$ for 3 heating sessions (1000°C,12hr, air; 1200°C, 12hr, air; 1500°C, 3hr, Ar) with intermediate grinding.[97] Both $Sr_2MnO_{3.84}$ and $Sr_2MnO_{3.71}$ retain the ideal tetragonal (*I4/mmm*) unit cell of Sr_2MnO_4 shown in figure 1.22a. Oxygen loss in these phases occurs from the equatorial (0, 0.5, 0) oxygen position producing a random statistical occupancy of ~92% and ~86% of the equatorial sites in $Sr_2MnO_{3.84}$ and $Sr_2MnO_{3.71}$ respectively. Corner sharing square based pyramids result from these oxygen defects. Synthesis of more highly oxygen deficient $Sr_2MnO_{3.64}$ resulted from heating Mn_2O_3 and $SrCO_3$ at 1350°C for 24hrs in N_2. This phase crystallizes in a monoclinic ($P2_1/c$) unit cell [a = 6.84057(30)Å, b = 10.77945(43)Å, c = 10.77423(43)Å, β = 113.211(4)] as shown in figure 1.22b with the O4 oxygen site only 23% occupied.[98] In the same work $Sr_2MnO_{3.64}$ was reduced to $Sr_2MnO_{3.5}$ by heating in 10%H_2/N_2 at 550°C for 8hr.[98] $Sr_2MnO_{3.5}$ is the first reduced phase of Sr_2MnO_4 which has ordered oxygen vacancies such that the monoclinic O4 site is completely vacant. Figure 1.22c shows the defect perovskite layer of $Sr_2MnO_{3.5}$ containing corner sharing square based pyramids. Note the presence of the 8 member MnO_5 elongated hexagonal units in similarity to the 6 member feature in the $Ca_2MnO_{3.5}$ defect perovskite layer (figure 1.21.). A similar synthesis of $Sr_2MnO_{3.5}$ was reported

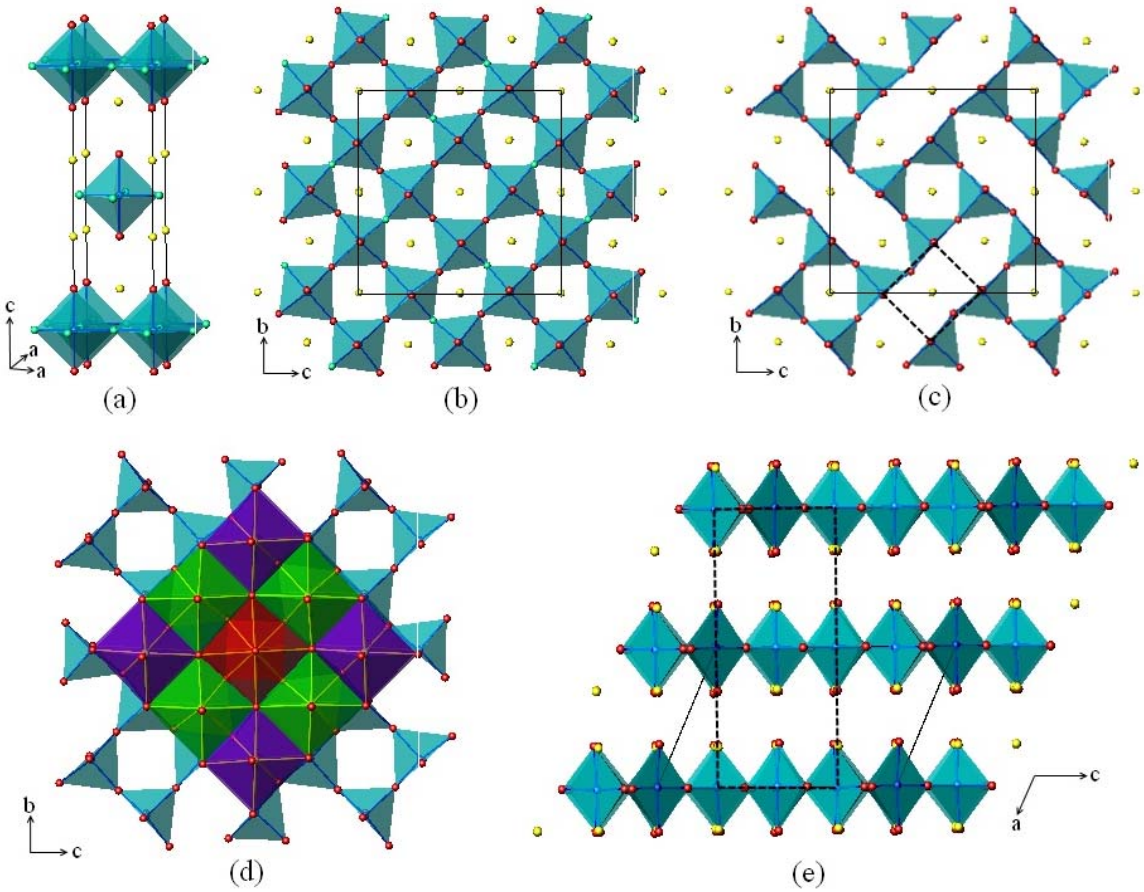

Figure 1.22. Tetragonal (*I4/mmm*) $Sr_2MnO_{3.84}/Sr_2MnO_{3.71}$ with disordered occupation of ~92% and ~86% of the light green oxygen site (a) Monoclinic ($P2_1/c$) $Sr_2MnO_{3.65}$ with disordered occupation of the light green oxygen site (b) Oxygen vacancy ordered monoclinic ($P2_1/c$) $Sr_2MnO_{3.5}$ including a dashed outline of the fully oxidized tetragonal unit cell (c) Sr-O coordination polyhedra in $Sr_2MnO_{3.5}$; Red – 9 coordinate face sharing polyhedra, Green – 8 coordinate face sharing polyhedra, Purple – 7 coordinate face sharing polyhedra. Not all strontium atoms are shown for clarity (d) The relationship between the monoclinic unit cell (solid) and the original tetragonal fully oxidized unit cell (dashed) (e). Yellow – strontium, red – oxygen, blue – manganese, light green = disordered oxygen vacancy site.[99,96,97,98,100]

from heating Sr_2MnO_4 in 10%H_2/He at 600°C for 1.5hr.[100] Fluorination of $Sr_2MnO_{3.5}$ has been reported to result from heating the material at 200°C in static 10%F_2/N_2 atmosphere for 2hr heating periods to produce a mixed product of $Sr_2MnO_{3.5}$ and $Sr_2Mn(OF)_4$.[101,102] The $Sr_2Mn(OF)_4$ with F ≈ 0.4 was not homogeneously fluorinated as indicated by the presence of monoclinic and tetragonal oxyfluoride compositions.[101] Overall it is clear that the synthesis of currently known Sr_2MnO_{4-x} phases is dominated by high temperature reactions with the exception of the moderate temperatures used to reduce to $Sr_2MnO_{3.5}$. The observation of a topotactic range of oxygen stoichiometry in the range of 3.5-4.0 makes this system a good candidate for metal hydride reduction. Additionally comparison of reaction conditions between the described methods of reduction of Sr_2MnO_4 and Ca_2MnO_4 makes it clear that more aggressive reduction conditions are required to reduce Sr_2MnO_4. Thus the structural stability of Sr_2MnO_4 is anticipated to be beneficial for the success of metal hydride reduction attempts.

Magnetic properties have been investigated for select Ruddlesden-Popper phases and oxygen defect structures discussed. The magnetic structure of Sr_2MnO_4 (figure 1.23) was reported by Bouloux to have an antiferromagnetic transition temperature of 170(5)K.[99] The magnetic structure requires a doubling of the crystallographic unit cell a-axis with antiferromagnetic alignment of magnetic moments parallel to the c-axis.[99] The magnetic structure of $Sr_2MnO_{3.5}$ (figure 1.23) has been reported to contain 4-member MnO_5 corner sharing ferromagnetic clusters which align in an overall antiferromagnetic arrangement.[100] The structure shown in figure 1.23 when proceeding to the next perovskite layer along the a-axis the opposite direction of magnetic moments for the clusters is observed. An earlier publication by Gillie shows some structural

contradictions in addition to revealing a differing interpretation of magnetic susceptibility data. The differing interpretations have led to conflicting T_N values of 126K and ~280K by Kato and Gillie respectively.[98,100] One major question in the reliability of Gillie's work arises from collection of neutron diffraction data for $Sr_2MnO_{3.64}$ followed by reporting a magnetic structure for $Sr_2MnO_{3.5}$.[98] The magnetic structure of Ca_2MnO_4 (figure 1.23c) results in antiferromagnetic alignment of moments parallel to the (001) plane with a transition temperature of ~114K.[103]

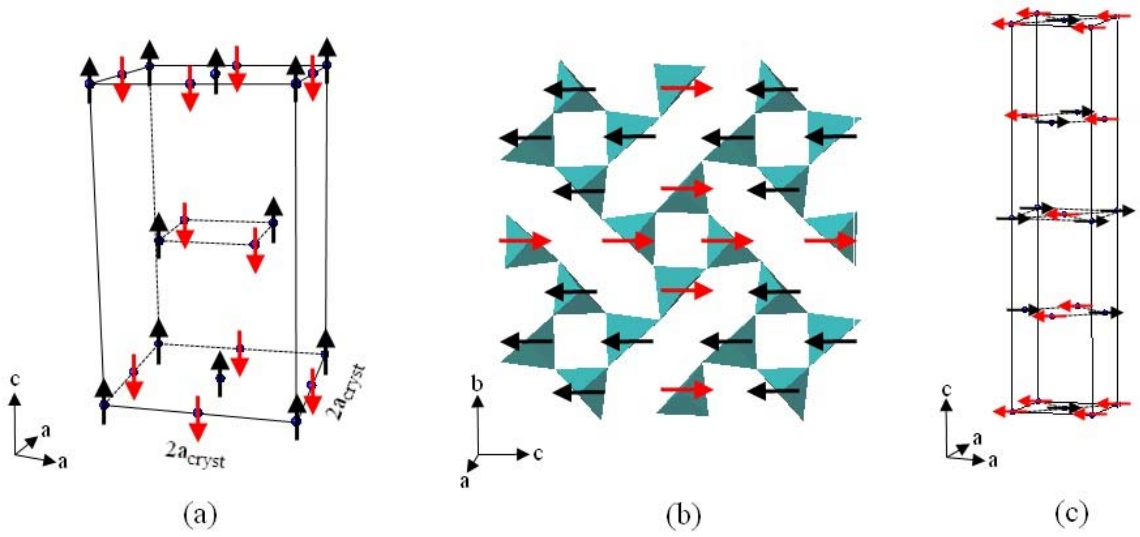

Figure 1.23. Magnetic structure of Sr_2MnO_4 (a) $Sr_2MnO_{3.5}$ (b) Ca_2MnO_4 (c).[99,100,103]

1.11. Scandium Vanadate

The scandium vanadate system $ScVO_{4-x}$ ($0<x<1$) has been well characterized in literature and is particularly interesting from a synthetic point of view.[104,105] $ScVO_4$ crystallizes in the tetragonal [a = 6.7804(1)Å, c = 6.1345(1)Å] zircon structure with space group $I4_1/amd$. This structure consists of edge sharing VO_4 tetrahedra and ScO_8 polyhedra.[106,107] Synthesis of all reported oxygen deficient $ScVO_{4-x}$ structures as shown in figure 1.24 require an initial reduction in CO/Ar (1:3) at 600°C to $ScVO_3$ which crystallizes in the cubic [a = 9.6182(1)Å] bixbyite structure with space group *Ia-3*.[108] The $ScVO_3$ bixbyite structure contains edge sharing VO_6 and ScO_6 octahedra with Sc^{3+} and V^{3+} disordered among the two cation sites.[105] An oxidative approach must be taken to access intermediate reduced phases. Topotactic oxidation to $ScVO_{3.5+x}$ ($0<x<0.22$) can be achieved by heating $ScVO_3$ in air at specific temperatures between 300-500°C.[109] Oxidation of $ScVO_3$ at 350°C for 4hrs in air results in production of $ScVO_{3.5}$. Increasing the temperature to a maximum of ~500°C yields more oxidized $ScVO_{3.5+x}$ ($0<x<0.22$) phases. All $ScVO_{3.5+x}$ ($0<x<0.22$) phases crystallize in a cubic defect fluorite structure with space group *Fm-3m*.[109,108] This structure can be viewed as a face centered cubic lattice of Sc^{3+}/V^{4+} with oxygen located in tetrahedral holes. Sc^{3+}/V^{4+} are disordered on the 4a cation site with each cation statistically occupying half the sites. In addition the oxygen 8c site is only 87.5% and 92.5% occupied in $ScVO_{3.5}$ and $ScVO_{3.70}$ respectively. Further oxidation of the defect fluorite structure is possible by a heat treatment at 500°C for 12hrs in O_2 flow to yield an oxygen defect zircon structure of composition $ScVO_{3.94}$ with 98.5% occupancy of the oxygen site.[109] This oxidation is not topotactic as complete structural reorganization is required. Topotactic oxidation from $ScVO_{3.94}$ to $ScVO_4$ has

been reported taking place at 1100°C in oxygen flow. A striking feature of the $ScVO_{4-x}$ ($0<x<1$) phases is the oxidative route required. Although $ScVO_{3.5+x}$ can be reduced to $ScVO_3$ as shown in figure 1.24, $ScVO_4$ cannot be reduced to $ScVO_{3.94}$ nor can $ScVO_{3.94}$ be reduced to $ScVO_{3.5+x}$ using conventional gas reductants. Most surprising is that $ScVO_{3.94}$ which has the same structural topology as $ScVO_4$ cannot be synthesized by reduction. This proposed reduction is particularly attractive as a method for testing the application of metal hydrides as reductants. It is anticipated that the strong reduction potential of hydride anions and their low temperature reactivity could promote a single step reduction from the fully oxidized zircon structure to the $ScVO_{3.94}$ defect structure.

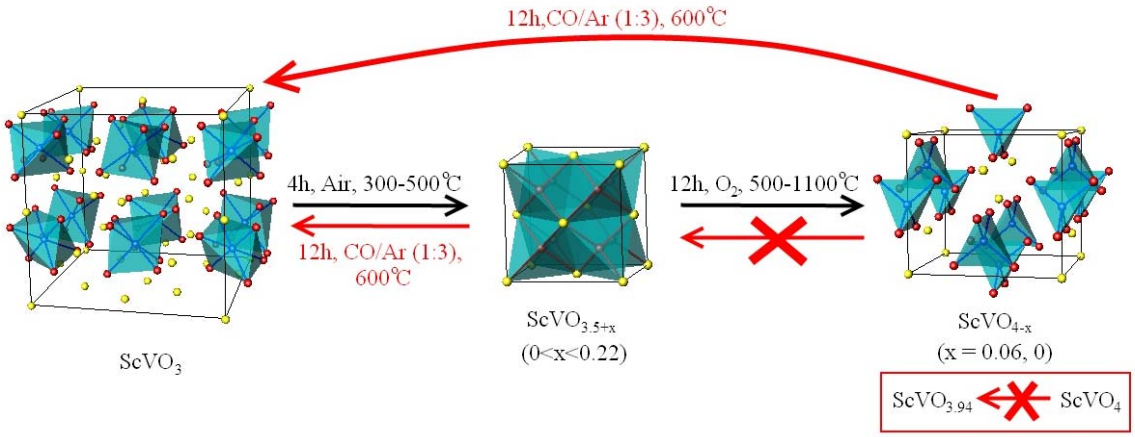

Figure 1.24. A schematic of the synthetic methods used to produce $ScVO_{4-x}$ ($0<x<1$) phases. Red crossed arrows indicate currently unavailable reaction pathways. $ScVO_3$ - blue and yellow cation sites are disordered with Sc^{3+}/V^{3+}. $ScVO_{3.5+x}$ – yellow disordered Sc^{3+}/V^{4+} site. $ScVO_{4-x}$ ($x = 0.0$, 0.06) – yellow Sc^{3+}, blue $V^{4+/5+}$. Red – oxygen in all structures. [108,109,104,107]

2. EXPERIMENTAL METHODS

2.1. Starting Material Preparation

2.1.1. Manganates

Polycrystalline bulk samples (approx. 6g) of $Sr_{2-x}Ca_xMnO_4$ ($x \approx 0, 0.1, 0.4, 1.5, 1.8, 2$) and $Sr_{2-x}Ba_xMnO_4$ ($x \approx 0.02, 0.04$) were prepared using high temperature solid state synthesis according to equation 2.1 [A = Ca or Ba]. Stoichiometric quantities of $SrCO_3$ (Alfa Aesar, 99.99%), $CaCO_3$ (CERAC, 99.95%) or $BaCO_3$ (Alfa Aesar, 99.95%) and Mn_2O_3 (CERAC, 99.9%) were ground in an agate mortar with acetone and heated according to sample composition. Sr/Ca solid solutions with $x \leq 1.5$ and Sr/Ba solid solutions were heated for 72 hours (24hrs, regrind, 48hrs) in static air at 1300°C followed by heating for 30min in static air at 1650°C and quenching to room temperature. Sr/Ca solid solutions with $x > 1.5$ only required a single heating for 72hours.[89,99]

$$(4-2x)SrCO_{3(s)} + (2x)ACO_{3(s)} + Mn_2O_{3(s)} + \tfrac{1}{2}O_{2(g)} \rightarrow 2Sr_{2-x}A_xMnO_{4(s)} + 4CO_{2(g)} \qquad \textbf{2.1}$$

It should be noted that performing the second heat treatment for Sr_2MnO_4 at 1500°C in flowing argon was later adopted to yield a product free of $Sr_7Mn_4O_{15}$ impurity.[96] Sr_2MnO_4 typically has 1-2% of $Sr_3Mn_2O_7$ impurity and Sr/Ba solid solutions contain approximately 1% of $Sr_7Mn_4O_{15}$ impurity while all remaining starting materials were found to be phase pure by powder X-ray diffraction. The Sr/Ba solid solutions could only be synthesized with ≤ 2% barium. Specific compositions of the prepared black polycrystalline samples are provided in the appendix in table A.1.

2.1.2. Scandium Vanadate

Bulk polycrystalline samples (approx. 4g) of $ScVO_4$ were prepared by high temperature solid state synthesis according to equation 2.2. Stoichiometric amounts of NH_4VO_3 (CERAC, 99.9%) and Sc_2O_3 (Alfa Aesar, 99.995%) were ground in an agate mortar with acetone and heated for 12 hours at 1000°C in air resulting in a phase pure white product characterized by powder X-ray diffraction.[104]

$$Sc_2O_3 + 2NH_4VO_3 \rightarrow 2ScVO_4 + 2NH_3 + H_2O \qquad \textbf{2.2}$$

2.2. Reduction Reactions

2.2.1. Metal Hydride Reductions

A solid state reduction of a chosen starting material is carried out using NaH (Sigma Aldrich, 90-95%), LiH (Sigma Aldrich, 95%), MgH_2 (Alfa Aesar, 98%), CaH_2 (Sigma Aldrich, 90-95%), SrH_2 (CERAC, 99.5%) or BaH_2 (CERAC, 99.7%). Typically 200mg of starting material is ground in an agate mortar with a four fold stoichiometric (x = 0.5) excess of the metal hydride reductant with respect to equations 2.3-2.6 in an N_2 filled MBraun Unilab glovebox (O_2 < 1ppm). The reaction mixture is then transferred to a Pyrex ampoule and sealed under vacuum (p<0.001mbar). To ensure safety ampoule volumes are made large enough that the maximum possible pressure in the ampoule is 2atm. The ampoules are heated at a specific temperature between 100°C and 600°C for 24 hours. Reaction products were stored in glass vials in air. Excess hydride was removed by stirring the products for about 20 minutes in approximately 10mL of 0.1M NH_4Cl in methanol, generating H_2 gas and dissolving the metal oxide and hydroxide reduction byproducts.[50] Once the hydride removal was completed (H_2 generation ceased) the

solution was filtered and washed with 6x10mL of methanol. It should be noted that this filtering process does not successfully remove insoluble MgO.

Metal hydride reductions of the manganates are anticipated to proceed according to equation 2.3 and 2.4 [A = Sr, Ca, Sr/Ca, Sr/Ba; Y = Li, Na; Z = Mg, Ca, Sr, Ba].

$$A_2MnO_4 + (x)\text{‘Y’}H \rightarrow A_2MnO_{4-x} + (x)H^+ + (x)O^{2-} + (x)\,Y^+ \qquad \textbf{2.3}$$

$$A_2MnO_4 + (^x/_2)\text{‘Z’}H_2 \rightarrow A_2MnO_{4-x} + (x)H^+ + (x)O^{2-} + (^x/_2)\,Z^{2+} \qquad \textbf{2.4}$$

Metal hydride reductions of $ScVO_4$ are anticipated to proceed according to equations 2.5 and 2.6 [Y = Li, Na; Z = Mg, Ca, Sr, Ba].

$$ScVO_4 + (x)\text{‘Y’}H \rightarrow ScVO_{4-x} + (x)H^+ + (x)O^{2-} + (x)Y^+ \qquad \textbf{2.5}$$

$$ScVO_4 + (^x/_2)\text{‘Z’}H_2 \rightarrow ScVO_{4-x} + (x)H^+ + (x)O^{2-} + (^x/_2)Z^{2+} \qquad \textbf{2.6}$$

It should be noted that in equations 2.3 and 2.6 the production of NaOH is observed when reducing with NaH. Also reduction of Sr_2MnO_4 using LiH according to equation 2.3 prompted a study investigating the reduction of Sr_2MnO_4 as a function of mol % LiH.

2.2.2. Modified Reductions of Sr_2MnO_4

Modified reduction experiments were carried out to understand the influence of H^-, H_2 and vacuum on the reduction of Sr_2MnO_4.

Variable concentration hydrogen atmosphere (100%H_2, 50%H_2-50%Ar) flowing through a tube furnace was used to reduce 200mg samples of Sr_2MnO_4 at specific temperatures between 100^{o}C and 600^{o}C for 24 hours according to equation 2.7. To contrast with these results are variable volume/constant pressure reductions using CaH_2

which involve modifying procedure *2.2.1.* For each reaction temperature (100-600^{o}C) the ampoule volumes are such that a maximum of 1atm H_2 pressure can be produced if all H^- decomposes to H_2.

$$Sr_2MnO_4 + xH_2 \rightarrow Sr_2MnO_{4-x} + xH_2O \qquad \textbf{2.7}$$

Static and dynamic vacuum reactions were contrasted. Sr_2MnO_4 samples (approx. 200mg) were heated at specific temperatures between 100^{o}C and 600^{o}C for 24 hours in vacuum sealed Pyrex ampoules to observe the effects of oxygen equilibrium on reduction according to equation 2.8. Dynamic vacuum reductions were attempted by following the procedure in *2.2.1* with the exception that products were heated under dynamic vacuum to remove any evolved H_2. These reactions were not successful as no reaction was observed, even when up to a 5-fold stoichiometric excess of metal hydride was used.

$$Sr_2MnO_4 \xrightarrow{\Delta,\ \text{Low P}} Sr_2MnO_{4-x} + {}^{x}/_{2}O_2 \qquad \textbf{2.8}$$

The combined influence of vacuum and hydrogen atmosphere on Sr_2MnO_4 reduction was evaluated using thimble reactions.[24] These reactions require modifying procedure *2.2.1* by having the metal hydride and starting material in separate glass holders or "thimbles" within a sealed ampoule (figure 2.1). These reactions proceed according to a combination of equation 2.7 and 2.8.

Figure 2.1. An illustration of an ampoule used for a thimble reaction.

The final reduction study was concerned with $CO:CO_2$ (1:9, 3:7, 7:5, 9:1, 10:0) in-situ powder X-ray diffraction reductions of Ca_2MnO_4 and Sr_2MnO_4, according to equation 2.9 (A = Sr, Ca). The samples were ground in acetone and mounted on a platinum heating element which was heated from 25°C to 700°C, collecting data every 25°C using Cu $K\alpha_{1,2}$ (λ = 1.540598Å, 1.544426Å) radiation over the 2θ range 10-90° with 0.0167° steps. Each reduction reaction required mounting a new sample.

$$A_2MnO_4 + xCO \rightarrow Sr_2MnO_{4-x} + xCO_2 \qquad \textbf{2.9}$$

2.3. Powder X-ray Diffraction

Powder X-ray diffraction experiments were carried out on a PANalytical X'Pert Pro diffractometer in Bragg Brentano geometry using Cu $K\alpha_{1,2}$ (λ = 1.540598Å, 1.544426 Å) radiation equipped with a diffracted beam Ni-filter and a RTMS (Real Time Multiple Strip) X'Celerator detector with 128 detector strips. The PreFIX (Pre-aligned Fast Interchangeable X-ray Modules) design allows for customization of the instrument

to one's experimental needs without the need for re-alignment. This includes the selection of sample stage and incident beam optics including soller slits, mask, divergence slit, anti-scatter slit and the diffracted beam anti-scatter slit, soller slits and β-filter. All reported unit cell dimensions and structural refinements were carried out using the Rietveld package FullProf 2008.[110]

2.3.1. MPD Spinner

In MPD (Multi-Purpose Diffractometer) sample spinner mode room temperature diffraction patterns are collected with powder samples mounted on a 30mm diameter (511) cut silicon zero background holder typically over the 2θ range of 10-120^{o} with 0.0083^{o} steps. Samples are either ground as an acetone slurry and mounted on the sample holder or they are mounted as a dry powder on top of a thin film of grease.

2.3.2. Capillary Spinner

The capillary spinner sample stage is designed to hold a goniometer head which can hold glass capillaries containing air sensitive polycrystalline samples. Pyrex capillaries (0.3mm diameter) were filled with air sensitive sample and sealed with liquid wax in an MBraun Unilab glovebox (O_2<1ppm). An experiment scanning over the 2θ range 10-120^{o} with 0.0167^{o} steps takes approximately 15 hours since only a very small fraction of the X-ray beam is occupied by the capillary. The capillary is aligned in the X-ray beam using an alignment microscope and adjusting the goniometer so that the capillary is centered in the microscope cross hairs. The incident beam divergence slit and anti-scatter slits were set at ¼^{o} and ½^{o} respectively. The diffracted beam anti-scatter

shield containing a 3.4^{o} anti-scatter slit was equipped with an additional anti-scatter extension to limit stray radiation from entering the detector.

2.3.3. In-situ Powder X-ray Diffraction

Non-ambient in-situ powder X-ray diffraction experiments were carried out on the PANalytical X'Pert Pro diffractometer mentioned in section *2.3* equipped with an Anton Paar HTK2000 high temperature camera with a platinum strip heater. Powder samples are ground as an acetone slurry and mounted as a thin layer on the platinum heating element and the sample is heated incrementally and data are collected at each temperature step. Temperatures and atmospheric conditions (eg. air, CO, inert gas) used depend on the specific experiment.

2.4. Thermogravimetric Analysis

Thermogravimetric analysis for oxygen deficient phase oxidation was carried out on a Linseis L81 thermal analyzer. These experiments involve heating approximately 50mg of sample and Al_2O_3 reference in flowing oxygen (6L/min) atmosphere from room temperature to approximately 800^{o}C at a rate of 25^{o}C/min followed by cooling to room temperature at 60^{o}C/min. A buoyancy correction is applied to the data by subtracting a background experiment carried out under the same experimental conditions with both samples being Al_2O_3 references. Several TGA oxidation experiments were carried out externally on a Netzsch STA 409 thermobalance heating to 700^{o}C at a rate of 5^{o}C/min. All TGA data in figure 3.7 were carried out externally.

2.5. Magnetic Susceptibility Measurements

A Quantum Design Magnetic Property Measurement System (MPMS) was used to measure magnetic susceptibilities for oxygen defect Sr_2MnO_{4-x} phases. The magnetometer consists of a sample transport system, a gradiometer coil coupled to a SQUID (Superconducting Quantum Interference Device) which contains highly sensitive Josephson junctions, and a superconducting magnet (0±7T). The temperature control system allows for sample temperatures from 2-400K. All data collections used a 5cm sample movement through the gradiometer coil with the sample (approx. 50mg) mounted in a gelatin capsule within a plastic straw. All measurements required both zero field cooled (ZFC) and field cooled (FC) data. ZFC measurements required cooling the sample to 2K, turning on the magnet to 1000Oe and measuring the magnetic susceptibility on warming to 400K. FC measurements require the sample to be cooled with the magnetic field turned on followed by data collection beginning at 2K once thermal stability is achieved.

3. RESULTS AND DISCUSSION – PART I

3.1. Ruddlesden-Popper Starting Materials

For all synthesized Ruddlesden-Popper phases (*2.1.1*) room temperature X-ray diffraction patterns were collected to assess phase purity and to examine the unit cell volume evolution as a function of composition. The Rietveld plot of $Sr_{0.211(3)}Ca_{1.789(4)}MnO_4$ (Table A1) is shown in figure 3.1.

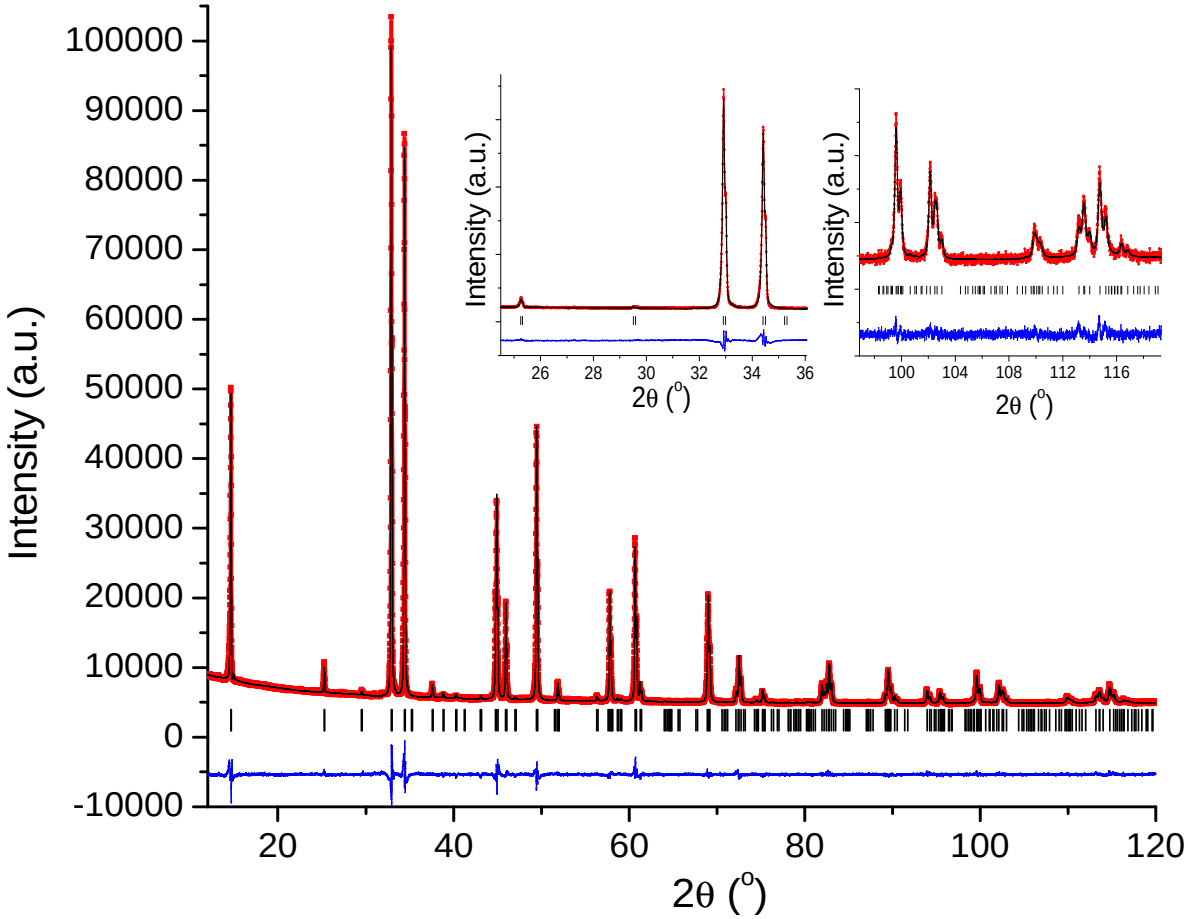

Figure 3.1. Powder X-ray diffraction Rietveld refinement of $Sr_{0.211(3)}Ca_{1.789(4)}MnO_4$, Cu $K\alpha_{1,2}$ (λ = 1.540598Å, 1.544426 Å). The red symbols are experimental data, the best fit and difference are shown as black and blue lines respectively. The black tick marks correspond to Bragg positions.

Table 3.1. Refined unit cell parameters (upper table) and atomic coordinates (lower table) resulting from Rietveld refinement of powder X-ray diffraction data for $Sr_{0.211(3)}Ca_{1.789(4)}MnO_4$.

Number of Reflections	120
Number of Parameters	36
R_p (%)	1.81
R_{wp} (%)	2.69
R_B (%)	2.79
χ^2	4.55
Space Group	$I4_1/acd$
a (Å)	5.2088(2)
c (Å)	24.1917(8)
V (Å^3)	656.35(4)

Atom	Site	x	y	z	SOF[a]
Ca	*16d*	0	1/4	0.55106(8)	0.894(4)
Sr	*16d*	0	1/4	0.55106(8)	0.106(4)
Mn	*8a*	0	1/4	3/8	0.5
O1	*16d*	0	1/4	0.4551(2)	1.0
O2	*16f*	0.210(8)	0.471(9)	1/8	1.0

[a] Site occupancy factors were only refined for strontium, calcium.

In total 36 parameters were refined including the scale factor, background, zero point, peak shape, peak asymmetry, unit cell parameters, Debye-Waller factors, atomic coordinates and site occupancy factors for calcium and strontium. These parameters were consistently refined for all starting materials. The resultant unit cell volume of $Sr_{2-x}A_xMnO_4$ (A = Ca,Ba) phases develop linearly as a function of x as shown in figure 3.2. Doping the strontium site in Sr_2MnO_4 with barium results in a linear increase in unit cell volume in contrast calcium doping results in a linear decrease. The almost linear unit cell volume evolution provides confidence in the accuracy of the refined unit cell volumes. Barium doping in Sr_2MnO_4 is limited to $x \leq 0.04$ due to the large size of Ba^{2+} which does not match the A-site in the A_2MnO_4 structure (see table 3.2). This is indicated by the

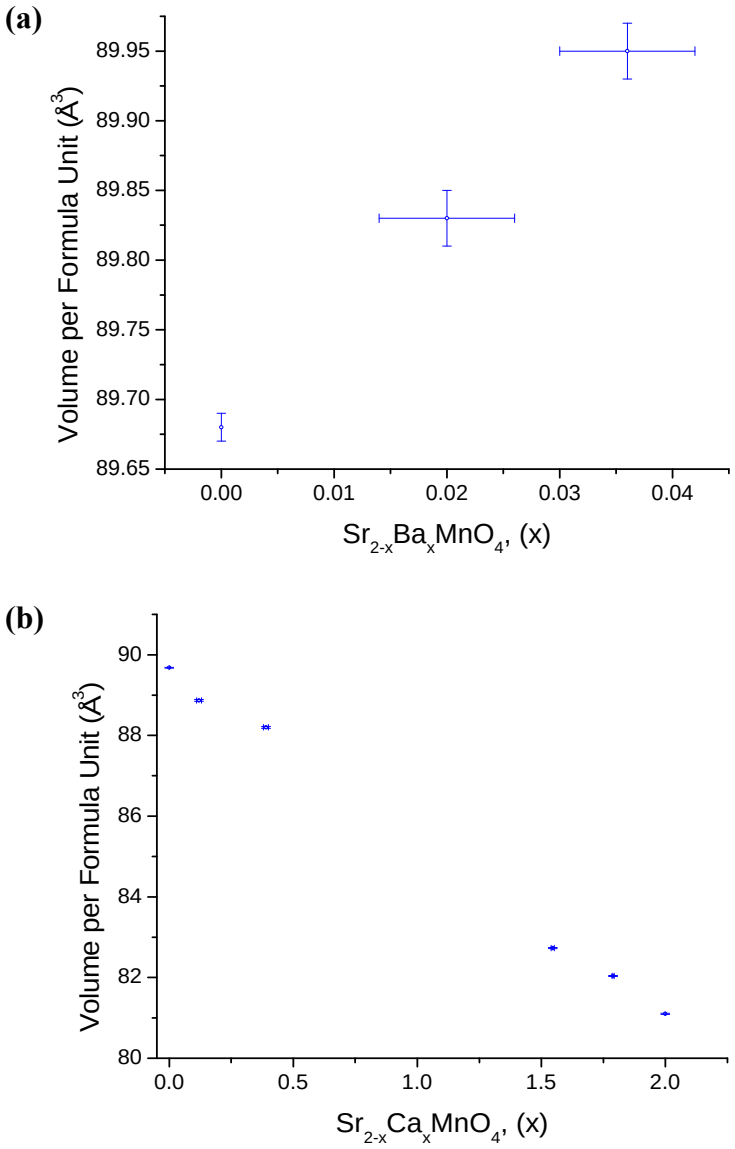

Figure 3.2. Unit cell volume evolution per formula unit for (a) strontium/barium and (b) strontium/calcium solid solutions.

tolerance factor (t) being greater than 1. This is also the reason why Ba_2MnO_4 has never been reported. The tolerance factor for Sr_2MnO_4 is nearest to unity indicating nearly ideal crystallographic matching between the SrO rock-salt layer and the $SrMnO_3$ perovskite layer.

Table 3.2. Ionic radii[a], unit cell volume and Poix tolerance factors for the starting material solid solution end members. [77,111]

A_2BO_4	A-cation Radii[c] (Å)	B-cation Radii[c] (Å)	Unit Cell Volume ($Å^3$)	Tolerance Factor (t)
Ca_2MnO_4	1.18	0.53	162.19(2)	0.91
Sr_2MnO_4	1.31	0.53	179.35(2)	0.96
Ba_2MnO_4	1.47	0.53	209.36(5)[b]	1.03

[a] The ionic radius of 6 coordinate O^{2-} used for the tolerance factor calculation was 1.4Å.
[b] The unit cell volume of the theoretical Ba_2MnO_4 was obtained by extrapolation of figure 3.2a.
[c] The A-cation site is 9-coordinate and the B-cation site is 6-coordinate.

3.2. Preliminary Starting Material Reductions

Preliminary reductions of a variety of the synthesized starting materials were carried out using NaH and CaH_2 (figure 3.3). The goal for these reactions was to identify a starting material which could be reduced topotactically and controllably at low temperatures (100-600^oC) and was structurally stable such that decomposition was minimal. It was expected that such qualities would make a starting material a good candidate for accessing novel oxygen deficient metastable states and potentially oxyhydrides.

Examination of figure 3.3 reveals information about the ability of NaH and CaH_2 to reduce the Ruddlesden-Popper starting materials and also illustrates the stability of the starting materials under reducing conditions at moderately low temperatures. A unit cell volume increase will coincide with a reduction of Mn^{4+} to Mn^{3+}. This allows for trends to

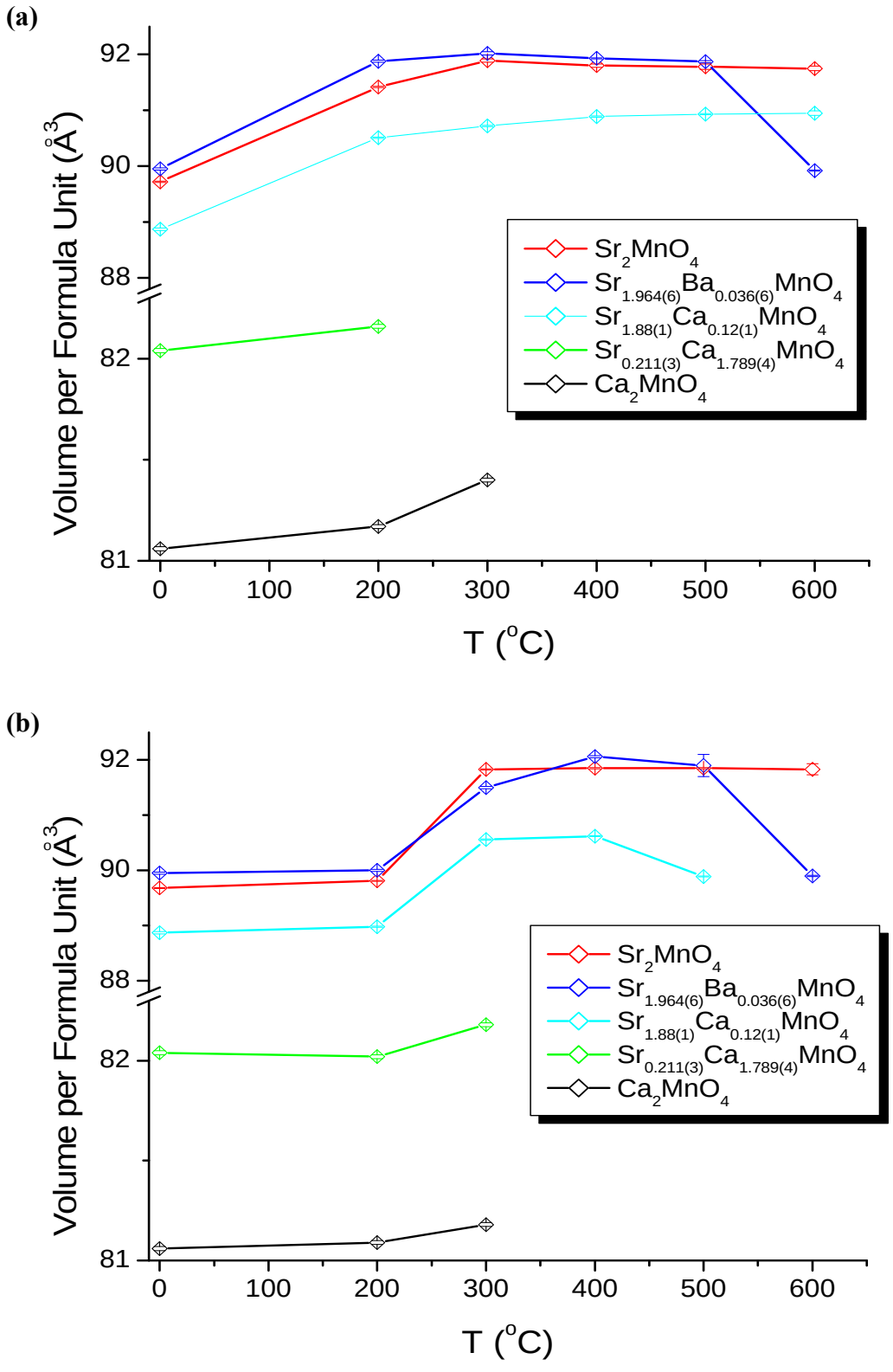

Figure 3.3. Volume per formula unit of select starting materials as a function of reaction temperature reducing with (a) NaH and (b) CaH_2. Volumes corresponding to 0°C represent unreduced starting materials.

be established by monitoring refined unit cell volumes as a function of reduction temperature. The calcium richest $Sr_{2-x}Ca_xMnO_4$ ($x \approx 1.8, 2.0$) phases reduce to the least extent based on the minor increase in positive slope between data points with increasing temperature. The calcium rich phases decompose/over-reduce beyond 300°C to phases including but not limited to $Ca_{0.747}Mn_{0.253}O$, $Ca_{0.241}Mn_{0.759}O$, $Ca_{0.9}Mn_{0.1}O$, $Sr_7Mn_4O_{15}$, $SrMnO_3$ and MnO. The structural instability and the minimal reduction over the explored temperature range make the calcium rich phases less suitable for further investigation. The three $Sr_{2-x}(Ca/Ba)_xMnO_4$ ($x \approx 0.1, 0.04, 0$) strontium rich phases in figure 3.3 show a smooth trend of data points as a function of temperature typically throughout the entire range. This is an indication that the strontium rich phases are more structurally stable under reducing conditions as compared to the calcium rich phases. The reduction of strontium rich phases is also much more extensive than calcium rich phases, accompanied by volume increases in the order of $2Å^3$ per formula unit. The strontium rich phase which appeared to have the desired characteristics for a more thorough investigation using metal hydride reductants is Sr_2MnO_4. Reduction of the strontium rich phases using NaH and CaH_2 results in maximum volumes being reached for the respective phases (figure 3.3). However at low temperatures (~ 200°C) striking differences in NaH and CaH_2 reactivity are observed. At this temperature NaH produces a reduced phase while CaH_2 does not. The results observed for the Sr/Ba preliminary reductions (figure 3.3) are very similar to that of Sr_2MnO_4 with the exception of an unexpected result at 600°C. Both 600°C products using NaH and CaH_2 refined to give lattice parameters and respective unit cell volumes nearly within error to that of the starting material with no signs of decomposition. This is an indication that no reduction

took place and also that no barium leached out of the structure. The reason for this result is not clear. The final starting material tested was $Sr_{1.88(1)}Ca_{0.12(1)}MnO_4$ (figure 3.3) which appears to reduce controllably over most of the temperature range using both NaH and CaH_2. The exception being the 600°C product using CaH_2 which results in decomposition to products listed above for the previous Sr/Ca phase decomposition. It should also be noted that the 500°C reduction product for $Sr_{1.88(1)}Ca_{0.12(1)}MnO_4$ is the only refined unit cell volume (figure 3.3) which arises from anisotropic unit cell parameter changes (a-axis = -0.05(1)%; c-axis = +1.25(1)%) with respect to the starting material. The evolution of unit cell dimensions for $Sr_{1.88(1)}Ca_{0.12(1)}MnO_4$ being reduced with NaH and CaH_2 is shown in figure 3.4. The purpose of this figure is to show that the unit cell parameters for $Sr_{1.88(1)}Ca_{0.12(1)}MnO_4$ reduced with NaH increase isotropically which is representative of all preliminary reactions with the exception of the 500°C CaH_2 reduction product. The fact that the 600°C CaH_2 reaction with $Sr_{1.88(1)}Ca_{0.12(1)}MnO_4$ led to complete decomposition could indicate that the anisotropic unit cell dimension changes observed at 500°C is the beginning of structural decomposition.

The preliminary reduction trends for Sr_2MnO_4 (figure 3.3) are easily understood with all reductions taking place isotropically and controllably between 100-600°C with minimal decomposition. Sr_2MnO_4 has been used to carry out a comprehensive investigation of the reduction abilities of several group I and II metal hydrides along with the synthesis of novel Sr_2MnO_{4-x} phases.

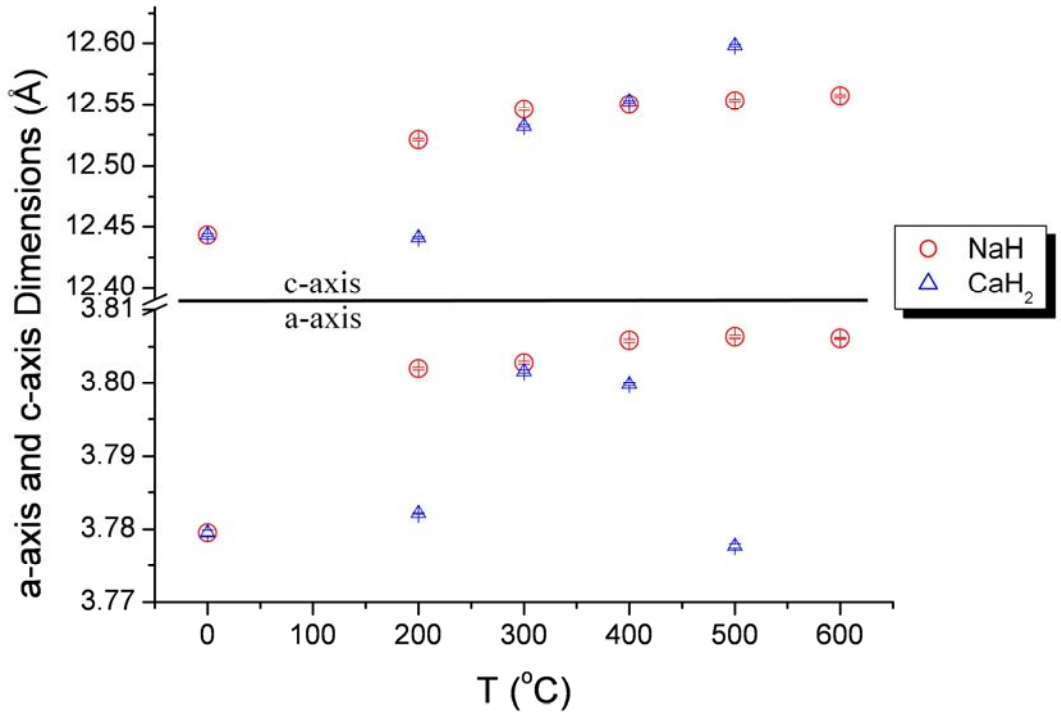

Figure 3.4. Unit cell dimension evolution for the reductions of $Sr_{1.88(1)}Ca_{0.12(1)}MnO_4$ with NaH and CaH_2. 0°C data points correspond to the starting material lattice parameters.

Preliminary reactions also provided valuable information about NaH and CaH_2 as reductants. Comparison of figure 3.3 (a) and (b) reveals clearly that reactions using CaH_2 at 200°C result in no reduction while using NaH results in partial reduction for all starting materials tested. This is an indication that NaH is a more effective reducing agent than CaH_2 at low temperatures. Detailed interpretation of metal hydride reactivities will be discussed in proceeding sections.

3.3. Sr_2MnO_4 Metal Hydride Reductions

Figure 3.5 contains the reduction trends for Sr_2MnO_4 with LiH, NaH, MgH_2, CaH_2, SrH_2 and BaH_2. This figure provides insight into the extent of reduction for Sr_2MnO_4 that can be achieved using metal hydrides between 100-600^oC and also which metal hydrides are most effective for accessing oxygen deficient phases. A clear observation in figure 3.5 is the apparent upper reduction limit reached by all metal hydrides at $\geq 500^oC$ corresponding to a reduced volume of approximately 91.75-91.95$Å^3$ per formula unit. This maximum volume range is consistent with the published volumes of 91.716(2)$Å^3$ and 91.96(1)$Å^3$ for $Sr_2MnO_{3.64(2)}$ and $Sr_2MnO_{3.5}$ respectively.[98] NaH is a particularly interesting reducing agent as it is the only metal hydride able to carry out a significant reduction between 150-200^oC. Since low temperature reactivity is ideal for carrying out topotactic reductions it is anticipated that this is the reason for NaH being such a common reducing agent in published work. BaH_2, CaH_2 and LiH all have very similar reduction trends with the exception of the 400^oC LiH product. These metal hydrides all give rise to an abrupt reduction to the maximum extent at 300^oC. The 400^oC LiH product initially appeared as though it may have resulted from experimental error, however it was reproduced several times. It was realized that this product results from anisotropic unit cell dimension changes (a-axis = -0.35%, c-axis = +1.4%) during reduction. This is the only anisotropic unit cell change observed in figure 3.5. It should be recalled that the anisotropic unit cell change for the 500^oC reduction product of

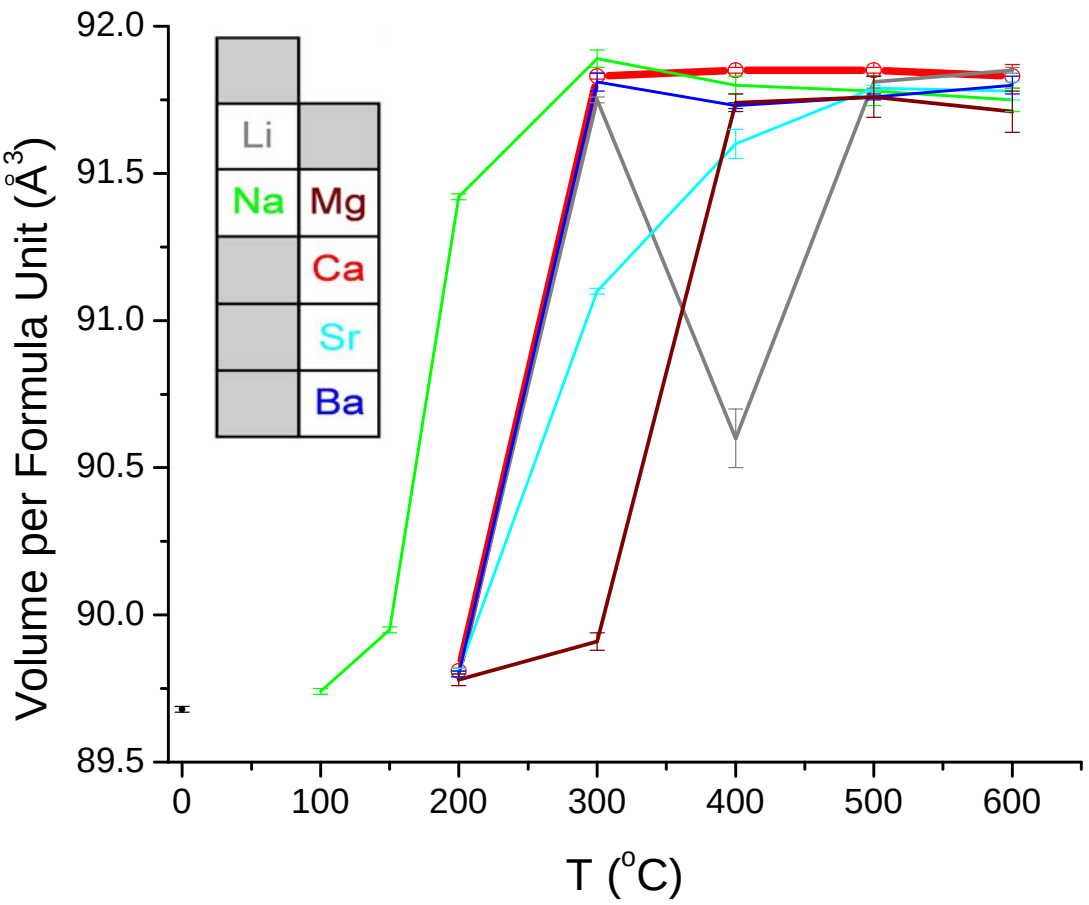

Figure 3.5. Volume per formula unit (Sr_2MnO_4) as a function of reductant (LiH, NaH, MgH_2, CaH_2, SrH_2 and BaH_2) and temperature (100-600°C). The data point at 0°C corresponds to the unreduced starting material.

$Sr_{1.88(1)}Ca_{0.12(1)}MnO_4$ with NaH (figure 3.4) was proposed to be caused by the beginning of decomposition as the higher temperature product decomposed. This is not the case for the anisotropic unit cell changes produced using LiH at 400°C (figure 3.5). For this reason it appears likely that this structural change could be the result of H^- or Li^+ insertion. This will be investigated in more detail in section *3.6*. Figure 3.5 revealed that magnesium hydride has a reduction trend very similar to CaH_2, LiH and BaH_2 except it is shifted to higher temperature by approximately 100°C. Therefore MgH_2 is the least

reactive reductant as a function of temperature. The final reduction trend for SrH_2 is particularly interesting and distinct compared to all the metal hydrides tested as its data points appear to follow a smooth curve to reach the maximum reduced volume. While there is a significant amount of literature supporting the use of NaH[24], CaH_2[38]and LiH[39,40] as solid state reductants, using SrH_2, MgH_2 or BaH_2 has not been published.

To help identify the metal hydrides that will allow for the most controllable reduction as a function of temperature table 3.3 shows the temperature interval required for each metal hydride to reduce Sr_2MnO_4 to the maximum extent. Most notably NaH and SrH_2 have the largest temperature intervals of 200°C and 300°C respectively, which reflects their gentler slope as a function of temperature. Carrying out targeted synthesis of specific oxygen deficient phases was anticipated to be most successful using NaH and SrH_2.

Table 3.3. The approximate temperature intervals over which each metal hydride is able to achieve maximum reduction with respect to figure 3.5.[a]

Metal Hydride	Approx. ΔT for Maximum Reduction (°C)
LiH	**100**
NaH	**200**
MgH_2	**50**
CaH_2	**100**
SrH_2	**300**
BaH_2	**100**

[a] *Note that for MgH_2 the ΔT is approximately 50°C since there is very minimal reduction at 200°C and 300°C.*

Explanation of the observed reactivity differences among the group I and II metal hydrides tested appears to be rather complex. Current literature focusing on the use of metal hydrides as solid state reductants provides no distinction between metal hydride reactivity nor a rationale for the choice of metal hydride used. This is likely because there are several factors (table 3.4) that could influence metal hydride reactivity such as decomposition temperatures, metal hydride structure, electronic considerations such as cation electronegativity and bond strength, and thermodynamic factors such as enthalpy of formation (table 3.4). Another important factor independent of the metal hydride reductant is the stability and reduction potential of the material to be reduced. Using only Sr_2MnO_4 permits to compare the reactivities of the different metal hydrides.

Table 3.4. Important thermodynamic, structural and electronic parameters influencing group I and II metal hydride reactivity.[30,112,113,114,115,31]

MH	T_{dec} (^oC)	Unit Cell, Structure, Space Group	Cation χ	ΔH_f^o (kJ/mol$_H$)[a]	H^- Radius (Å)
LiH	720	Cubic, Rock-salt, *Fm-3m*	0.98	-90.5	1.36
NaH	425	Cubic, Rock-salt, *Fm-3m*	0.93	-56.3	1.47
MgH_2	327	Tetragonal, Rutile, *$P4_2/mnm$*	1.31	-37.65	1.30
CaH_2	600	Orthorhombic, $CoSi_2$, *Pnma*	1.00	-90.75	1.35
SrH_2	675	Orthorhombic, $CoSi_2$, *Pnma*	0.95	-90.15	1.36
BaH_2	675	Orthorhombic, $CoSi_2$, *Pnma*	0.89	-88.5	1.34

[a] *Comparisons of ΔH_f^o values for metal hydrides are made per mol equivalent of H.*

To emphasize the complexity of the parameters affecting reactivity some comparisons can be made. Decomposition temperatures of metal hydrides are influential on reactivity (equation 1.17). The enthalpy of formation (ΔH_f^o) for metal hydrides is an important measure of thermochemical stability and can be used to estimate T_{dec}, thus these two parameters are correlated as shown in table 3.4.[30] It is expected that H^- mobility is highest as T_{dec} is approached. It also has to be realized that when using these reductants in sealed ampoules, T_{dec} will be decreased since ampoules are sealed under vacuum. Another parameter that may influence reactivity is the metal cation electronegativity (χ). Although all group I and II metal hydrides are considered saline hydrides, small differences in electronegativity can influence the polarity of the MH bond. As the metal cation electronegativity increases this could in principle decrease the electron density around hydrogen making it less able to donate electrons. This is reflected in the effective H^- ionic radii shown in table 3.4 with the most highly electronegative cation (Mg) contributing to the smallest H^- radius (1.30Å).[31] However this relationship is not applicable to all cation electronegativies. There does appear to be a correlation between cation electronegativity (table 3.4) with the reduction trends in figure 3.5. Comparing NaH and MgH_2 which both have the lowest T_{dec} values, Mg has the highest cation electronegativity and appears least reactive as a function of temperature while Na has the lowest electronegativity and is most reactive as a function of temperature. Also LiH, CaH_2, BaH_2 and SrH_2 have cations with intermediate electronegativities (~1) which appear to be reflected by them having reactivity beginning at intermediate temperatures to that of NaH and MgH_2. Another consideration is that the H-M bond becomes longer and weaker moving down groups I and II although this influence on reactivity is not consistent in explaining the reactivity of

the metal hydrides observed. This could be an indication that bond strength is not a limiting factor for the reactivity of metal hydrides. This appears to be reinforced by the fact that there is no clear trend between metal hydride structure and reactivity.

Overall it is difficult to deduce the origin of specific reactivity differences for the metal hydrides. Cation electronegativity seems to provide some insight into reactivity however it is unclear whether this is coincidence resulting from the complex interplay of electronic, structural and thermodynamic factors.

3.4. Optimized Synthesis and Characterization of Sr_2MnO_{4-x} Phases

Optimized reaction conditions for NaH and SrH_2 reductants allowed for a variety of oxygen deficient phases to be synthesized. Table 3.5 outlines the reaction conditions used as predicted from the preliminary reactions in figure 3.5. The ability to extrapolate appropriate reaction temperatures from figure 3.5 necessary to synthesize desired oxygen stoichiometries reinforced the reliability and reproducibility of the preliminary data. Figure 3.6 shows a comparison of the volume per formula unit for previously published Sr_2MnO_{4-x} phases with those synthesized using SrH_2 and NaH. The previously published data had a rather poor linear fit and errors on oxygen stoichiometry were estimated since these were not published. The poor fit of the previously published $Sr_2MnO_{3.72(5)}$ and $Sr_2MnO_{3.84(5)}$ phases indicate that the estimated error bars may not be large enough and that some published values may lack accuracy.[96,97] Contrasting this with the reduced phases synthesized using SrH_2 and NaH the overall linear fit of the data is much better with the exception of the most oxygen rich phases. It should be noted that the metal hydride reductions allowed for the gaps in the original data to be filled, resulting in the

synthesis of a number of novel oxygen deficient phases. Thermogravimetric analysis (TGA) data for the reduced phases synthesized using NaH and SrH_2 are shown in figure 3.7. Conservative error estimates on oxygen composition have been made based on instrument performance. These experiments required heating samples in flowing oxygen to 800°C at 5°C/min. Mass gains were consistently analyzed beginning at 250°C with figure 3.7d being the only exception due to a small initial mass loss attributed to sample moisture. Analyzed TGA data for the Sr_2MnO_4 starting material showed a 0.02% mass increase from 250°C to 500°C. It should be noted that the TGA trace for the starting material is distinctly different in appearance from all the reduced phases. This apparently small mass gain

Table 3.5. Optimized reaction conditions using NaH and SrH_2 to synthesize Sr_2MnO_{4-x} ($0.02<x<0.35$) phases. Reduced product oxygen stoichiometries as determined by TGA.

Metal Hydride	T (°C)	Volume per Formula Unit (Å^3)	Composition
Starting	Material	89.69(1)	$Sr_2MnO_{4.00(1)}$
SrH_2	200	89.83(1)	$Sr_2MnO_{4.00(1)}$
NaH	150	89.94(1)	$Sr_2MnO_{3.99(1)}$
SrH_2	250	90.44(1)	$Sr_2MnO_{3.90(1)}$
SrH_2	260	91.09(1)	$Sr_2MnO_{3.78(1)}$
NaH	200	91.49(1)	$Sr_2MnO_{3.69(1)}$
SrH_2	500	91.79(1)	$Sr_2MnO_{3.63(1)}$

was not expected, however this could be an indication that oxidation to a Sr_2MnO_{4+y} phase is possible. An experiment was conducted previously in which the starting material was heated in oxygen (T>500°C) in a tube furnace and the product was refined to have a unit cell volume within error to the unheated starting material. This ruled out the possibility that the starting material is partially reduced. Consistent for the reduced phases the TGA oxidation process is observed to begin gradually between 250°C and

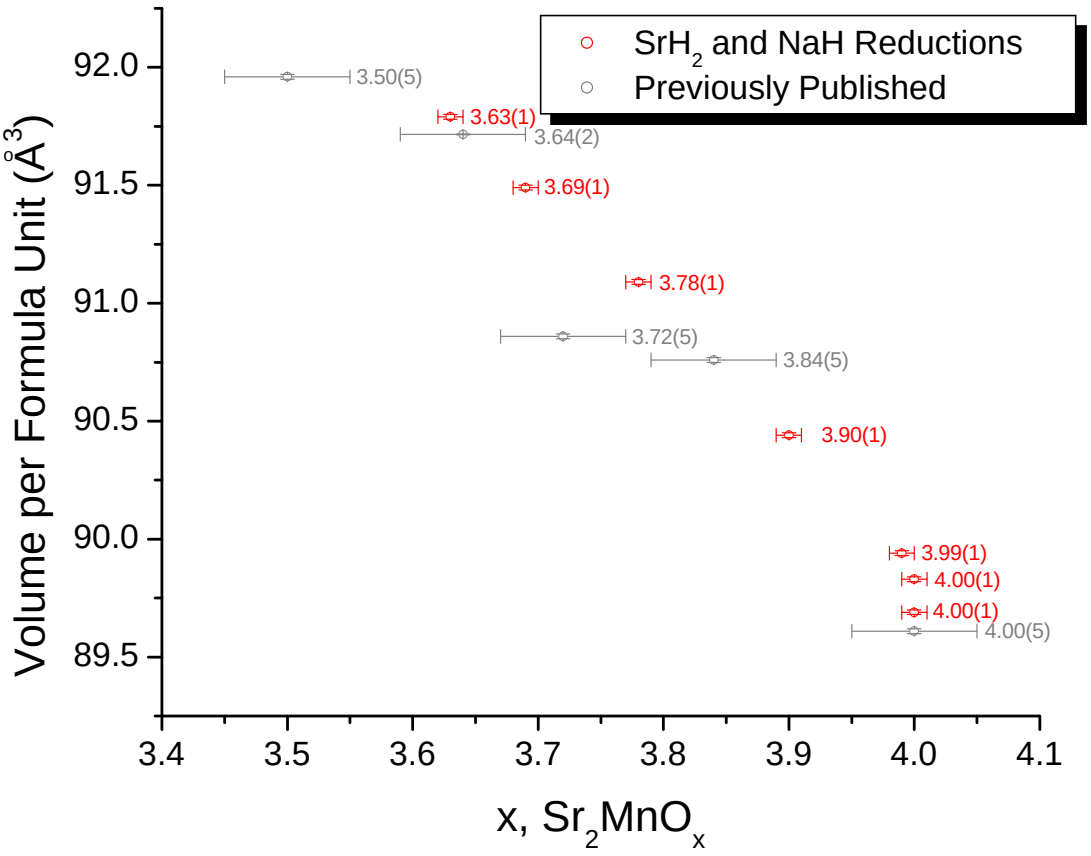

Figure 3.6. Volume per formula unit evolution comparing the known Sr_2MnO_{4-x} phases with those synthesized using SrH_2 and NaH.[117,97,98,99]

300°C with the most rapid mass gain between 350°C and 500°C. It is also clear in the TGA data that gradual oxygen loss takes place immediately after oxidation.

Literature indicates that $Sr_2MnO_{3.5}$ is monoclinic ($P2_1/c$) and that $Sr_2MnO_{3.72(5)}$, $Sr_2MnO_{3.84(5)}$ and Sr_2MnO_4 are tetragonal ($I4/mmm$). [117,97, 98,99] However literature discussing $Sr_2MnO_{3.64(5)}$ lacks clarity in its characterization with powder X-ray diffraction data refined on a tetragonal unit cell and neutron powder X-ray diffraction data refined on a monoclinic unit cell.[98] This introduces the question as to where the transition from monoclinic to tetragonal occurred for this system. Powder X-ray diffraction analysis of Sr_2MnO_{4-x} ($0<x<0.37$) phases resulting from SrH_2 or NaH reduction (table 3.5) allowed for investigation of novel structural details for this system. The phase $Sr_2MnO_{3.63(1)}$ synthesized using SrH_2 has been found to be monoclinic by X-ray diffraction while all less reduced phases are tetragonal. Notably, Gillie was not able to successfully characterize $Sr_2MnO_{3.64(5)}$ as monoclinic using powder X-ray diffraction.[98]Collection of powder X-ray diffraction data for $Sr_2MnO_{3.63(1)}$ over the 2θ range 10-120° using 0.0167° steps with 1500s counting times reveals clear monoclinic superstructure peaks between 18-22° (2θ). The powder X-ray diffraction Rietveld refinement for $Sr_2MnO_{3.63(1)}$ is shown in figure 3.8. Figure 3.9 shows a comparison of monoclinic $Sr_2MnO_{3.63(1)}$ with tetragonal $Sr_2MnO_{3.99(1)}$ and also the in-situ powder X-ray diffraction oxidation of $Sr_2MnO_{3.63(1)}$ emphasizing the phase transition from monoclinic to tetragonal at 350°C. This temperature is consistent with that of the oxidation temperatures observed in the TGA data (figure 3.7).

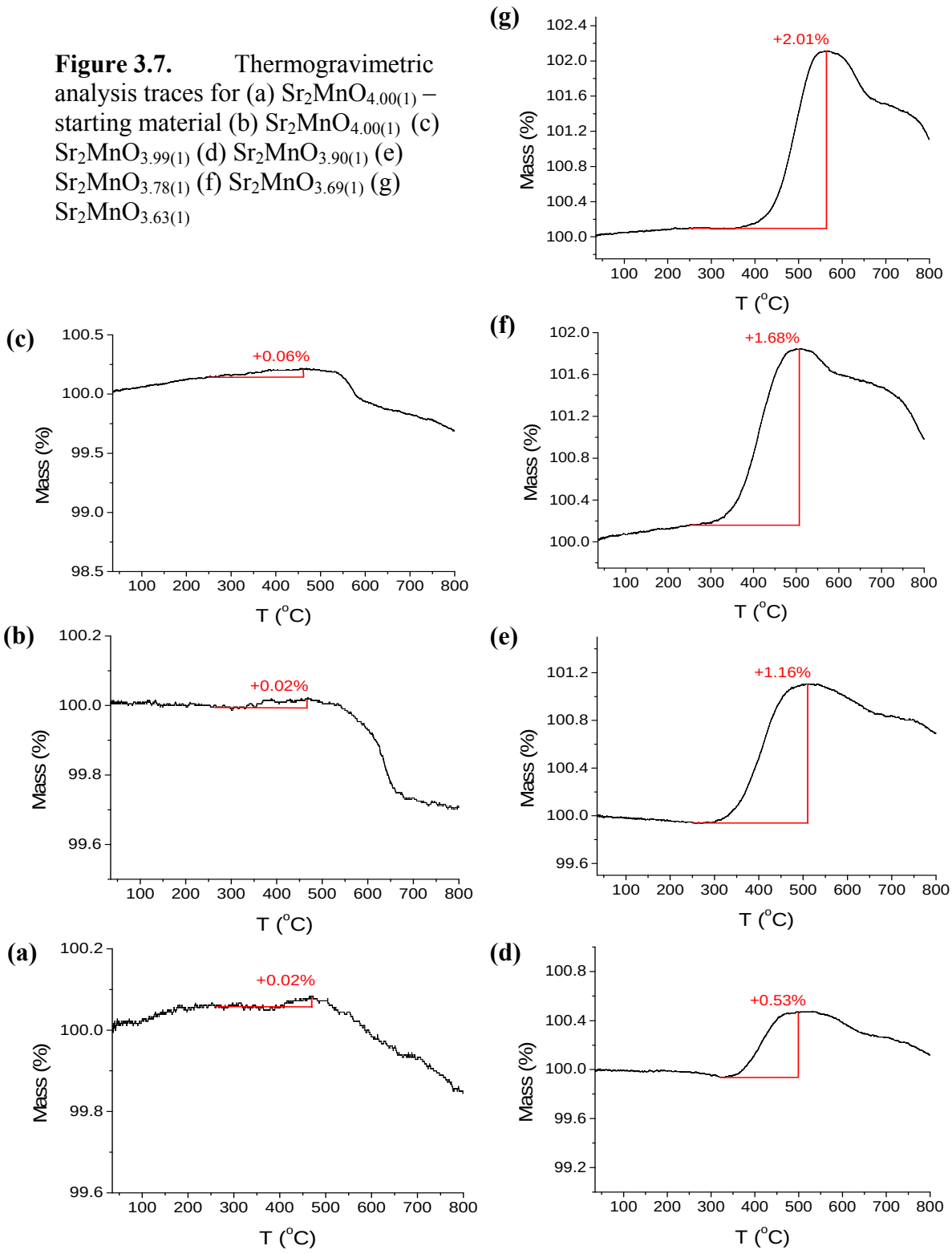

Figure 3.7. Thermogravimetric analysis traces for (a) $Sr_2MnO_{4.00(1)}$ – starting material (b) $Sr_2MnO_{4.00(1)}$ (c) $Sr_2MnO_{3.99(1)}$ (d) $Sr_2MnO_{3.90(1)}$ (e) $Sr_2MnO_{3.78(1)}$ (f) $Sr_2MnO_{3.69(1)}$ (g) $Sr_2MnO_{3.63(1)}$

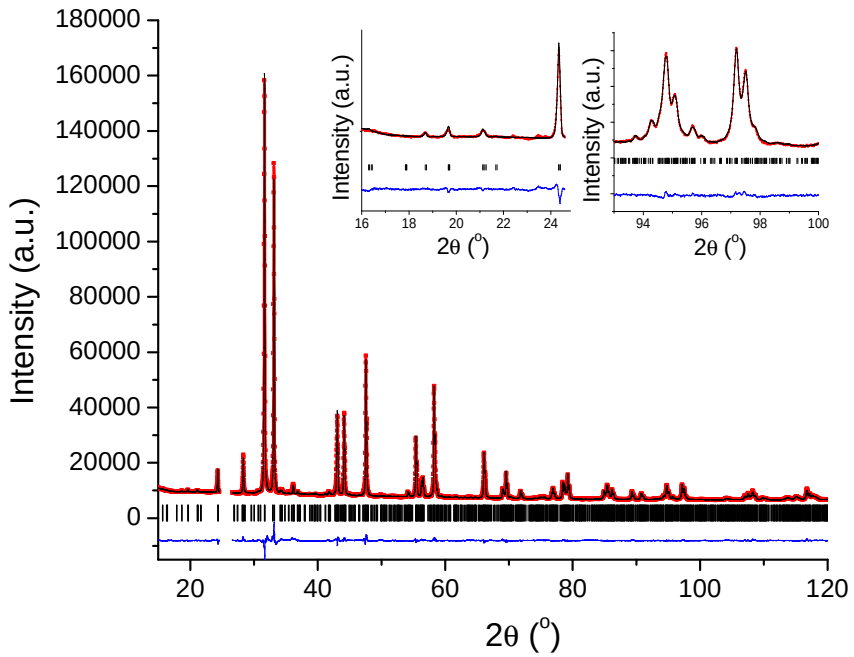

Figure 3.8. Monoclinic $Sr_2MnO_{3.63(1)}$ room temperature Rietveld plot. Powder X-ray diffraction data CuK$\alpha_{1,2}$ (Bragg R-factor = 4.20). Low angle (monoclinic superstructure peaks) and high angle insets. A broad peak unrelated to the monoclinic structure which appeared at 25.3° was excluded from the refinement.

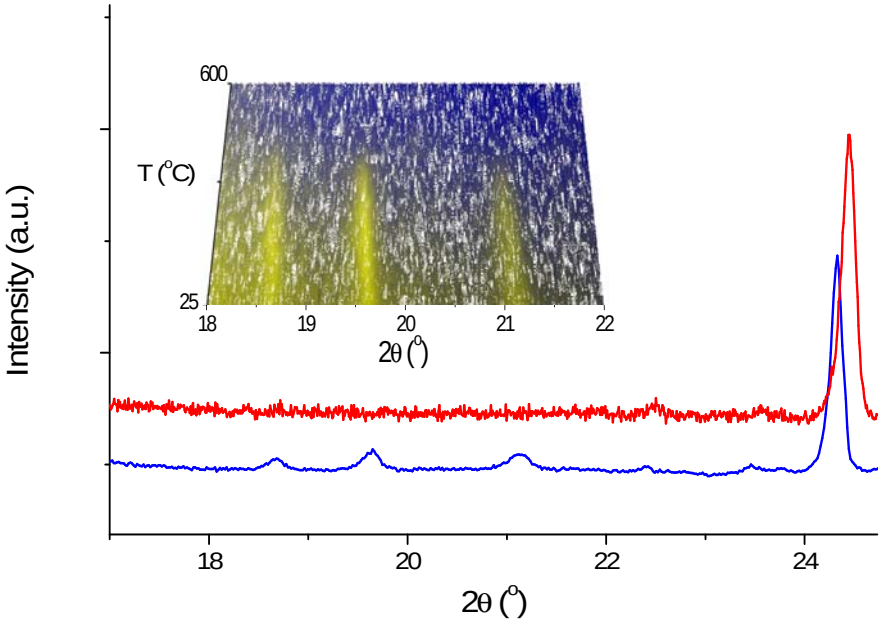

Figure 3.9. Powder X-ray diffraction patterns of monoclinic $Sr_2MnO_{3.63(1)}$ - blue, and tetragonal $Sr_2MnO_{3.99(1)}$ – red. Inset – powder X-ray diffraction contour plot of monoclinic $Sr_2MnO_{3.63(1)}$ oxidation in O_2 flow from 25°C to 600°C with 25°C increments. Intensities are shown as constant increments from blue = lowest intensity to yellow = highest intensity.

3.5. Magnetic Properties of Synthesized Sr_2MnO_{4-x} Phases

Bulk magnetic properties have been published previously for $Sr_2MnO_{3.5}$, $Sr_2MnO_{3.64}$ and Sr_2MnO_4. Sr_2MnO_4 has an antiferromagnetic ordering temperature of 170(5)K at which magnetic moments align along the c-axis with a doubling of the crystallographic a-axis (figure 1.23).[99] Literature describing the magnetic properties of $Sr_2MnO_{3.64}$ and $Sr_2MnO_{3.5}$ quote T_N values of 280K[98] and 126K[100] respectively while the data in both published papers look much the same. There appears to be a contradiction in the interpretation of the magnetic susceptibility data for these phases and it is not clear which interpretation is correct. Both papers however describe the same magnetic structure as containing ferromagnetic manganese clusters aligned antiferromagnetically within the perovskite layers of the monoclinic structure (figure 1.23). Shown in figure 3.11 are the resultant magnetic susceptibility data collected on five of the six phases reduced using NaH and CaH_2. Both field cooled and zero-field cooled data were collected on warming, ($2K \xrightarrow{2K} 30K \xrightarrow{5K} 100K \xrightarrow{10K} 400K$) in a 1000 Oe field. Tabulated antiferromagnetic transition temperatures are shown in table 3.6 for the reduced phases. All transition temperatures have been identified by determining the temperature at which a change of slope is observed in plots of $\frac{\partial(\chi T)}{\partial T}$ vs. T with an example shown for the $Sr_2MnO_{4.00(1)}$ starting material in figure 3.10. It should be noted that the second lower temperature change of slope is a feature that is not well understood for this system. It is clear that the T_N of 170(5)K observed for the $Sr_2MnO_{4.00(1)}$ starting material is in good agreement with the published value. The broadness of this transition should be noted such that only a small portion of data is collected for the paramagnetic regime due to temperature limitations of the SQUID magnetometer ($T_{max} = 400^oC$) which complicates

the analysis. For the intermediate reduced phases there does appear to be some fluctuation of the antiferromagnetic ordering temperature, emphasizing how only small concentrations of Mn^{3+} in the structure can significantly influence the magnetic properties. However the T_N of 180(3)K observed for $Sr_2MnO_{3.63(1)}$ is not consistent with the published value of 280K. The reason for this large deviation is not clear. Another aspect of the magnetic data resulting from the metal hydride reductions that differs from the published data is evidence for a low temperature magnetic transition at ~10-12K in several of the reduced phases (table 3.6). The evidence for this transition is only observed in the zero-field cooled data (figure 3.11a), most obviously for the composition $Sr_2MnO_{3.78(1)}$ having an average manganese oxidation state of 3.56+. In general the magnetic susceptibilities tend to increase systematically for phases with increasing Mn^{3+} concentration as expected.

Table 3.6. Summary of the magnetic data collected on Sr_2MnO_{4-x} phases resulting from MH reductions.

Sample	Avg. Mn Oxidation State	T_N (K)	Low T Transition (K)
$Sr_2MnO_{4.00(1)}$ – Starting Material	4+	170(5)	
$Sr_2MnO_{3.99(1)}$	3.98+	161(3)	12(2)
$Sr_2MnO_{3.90(1)}$	3.80+	181(3)	
$Sr_2MnO_{3.78(1)}$	3.56+	180(5)	12(2)
$Sr_2MnO_{3.69(1)}$	3.38+	170(3)	14(2)
$Sr_2MnO_{3.63(1)}$	3.26+	180(3)	10(2)

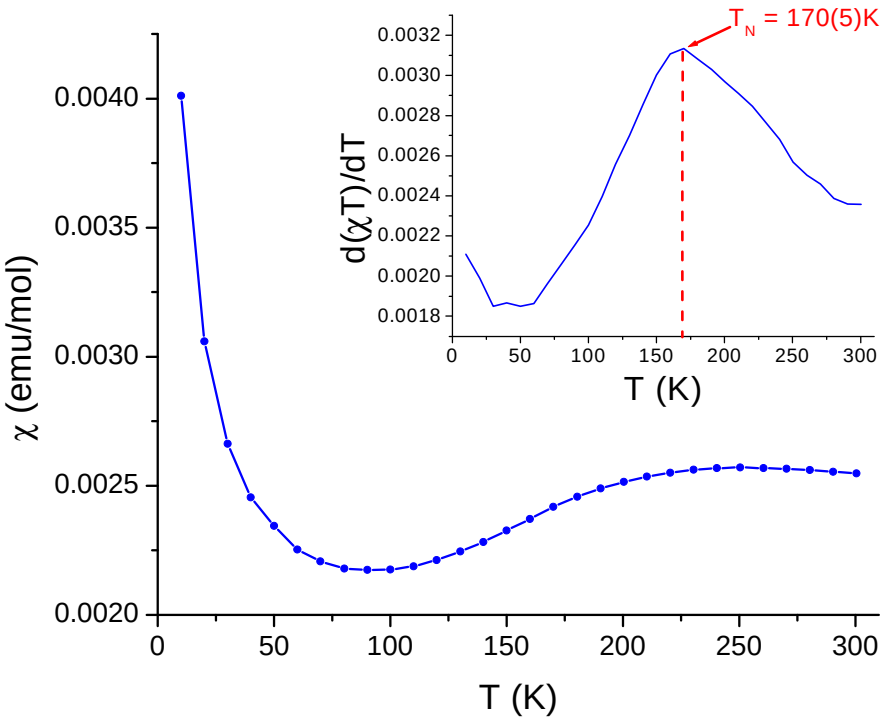

Figure 3.10. Zero field cooled magnetic susceptibility data for $Sr_2MnO_{4.00(1)}$ starting material using a 1000Oe magnetic field. Inset – $d(\chi T)/dT$ vs. T plot displaying the change in slope used to identify the T_N of 170(5)K.

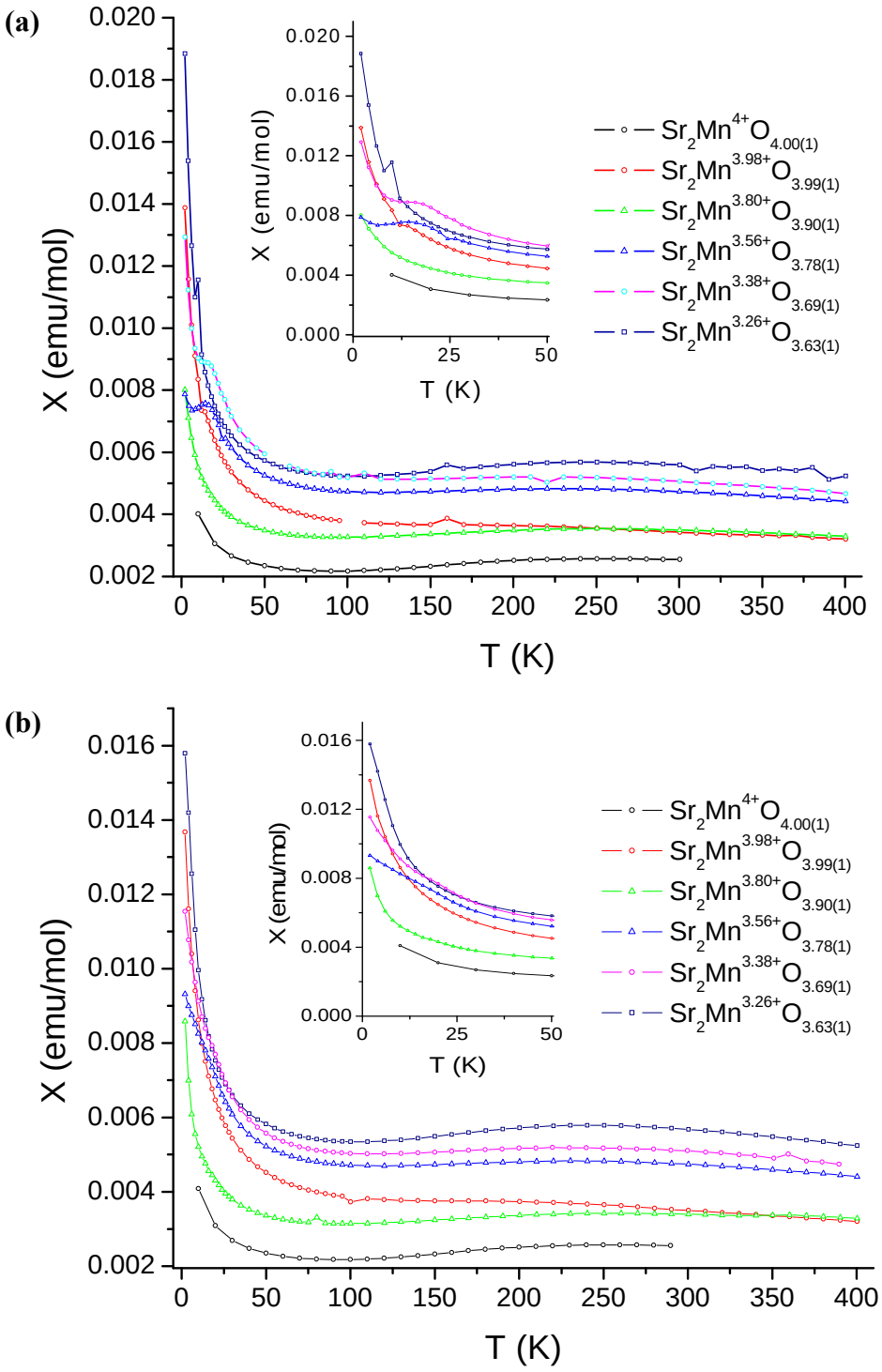

Figure 3.11. Zero-field cooled (a) and field cooled (b) magnetic susceptibility data for Sr_2MnO_{4-x} phases resulting from NaH and SrH_2 reduction using a 1000Oe field.

3.6. LiH Reduction of Sr_2MnO_4

The goal for re-investigating the LiH reductions of Sr_2MnO_4 is to gain insight into the anisotropic unit cell evolution upon reduction at 400°C as mentioned in section 3.3. Comparison of room temperature diffraction patterns for the 400°C reduced product with the Sr_2MnO_4 starting material is shown in figure 3.12. For the reduced phase it is clear that a significant number of peaks with Miller indices depending on the c-axis shift to lower 2θ angle ((103) reflection at 32°) indicating the c-axis expansion. It is also clear from the 33.5° (110) peak which depends on the a-axis that in the reduced phase this peak shifts to higher 2θ angle consistent with the a-axis contraction. It should be

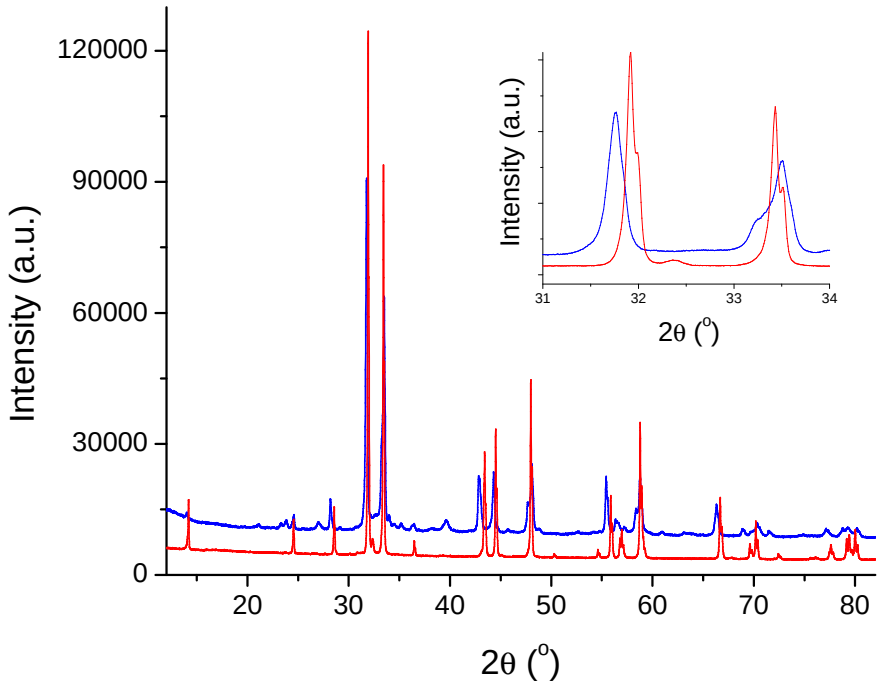

Figure 3.12. A comparison of room temperature powder X-ray diffraction data for the 400°C product of LiH reacting with Sr_2MnO_4 with the Sr_2MnO_4 starting material. The inset shows the comparison of the ~31.7° (103) and 33.5° (110) peaks shifting to lower and higher 2θ angle respectively.

noted that some $LiOH \cdot H_2O$ impurity is observed as a shoulder on the ~33.5° peak. There are a number of new peaks in the diffraction data which cannot be easily matched to impurities thus it is expected that the anisotropic unit cell dimension increase could be accompanied by a symmetry change. Attempts at indexing new peaks based on the original unit cell or a higher symmetry unit cell have not yet been successful. An in-situ powder X-ray diffraction oxidation experiment was performed on the 400°C LiH product (figure 3.13a) and compared to a previous in-situ oxidation of $Sr_2MnO_{3.69(1)}$ (figure 3.13b) resulting from isotropic unit cell expansion. Upon oxidation the LiH reduced phase (103) reflection shifts to higher 2θ angle and the (110) reflection shifts to lower 2θ angle consistent with expectation based on figure 3.12 indicating that this phase oxidizes back to the original Sr_2MnO_4 phase. The oxidized phase refined to give unit cell parameters within error to that of the starting material. Minor $LiOH \cdot H_2O$ and LiOH impurities were observed in the oxidized product. As shown in figure 3.13a this oxidation is distinctly different from the in-situ oxidation of $Sr_2MnO_{3.69(1)}$ which involves an isotropic shift of both main peaks to higher 2θ. Notably the oxidation of the LiH 400°C product occurs about 50°C lower than for $Sr_2MnO_{3.69(1)}$.

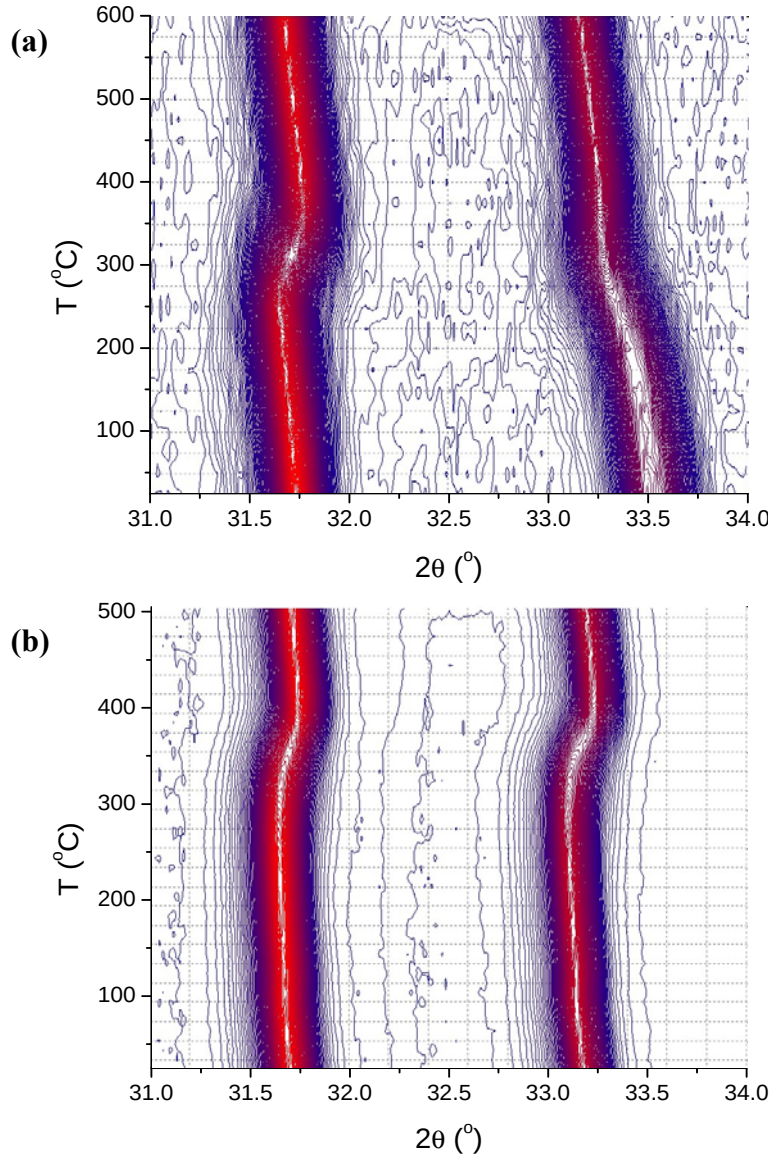

Figure 3.13. Powder X-ray diffraction contour plot for (a) the 400°C LiH reduction product focusing on the main 31.7° (103) and 33.5° (110) peaks and (b) the main peaks in $Sr_2MnO_{3.69(1)}$ reduced using NaH. Heating in O_2 flow from 25°C to 500 and 600°C respectively with 25°C increments. Intensities are shown as constant increments from blue = lowest intensity to red = highest intensity.

A systematic investigation of the LiH reactions with Sr_2MnO_4 was carried out by varying the mol % LiH while keeping the reaction temperature constant at 400^oC as shown in figure 3.14. A particularly interesting result from this figure is the observation that reductions having isotropic unit cell dimension increases can be carried out using a stoichiometric approach. This is revealed by the fact that from 0-240mol% LiH the reduction trend for the unit cell volume is comparable to that of preliminary reduction trends (figure 3.5.). This is also supported clearly by the isotropic behaviour of the (a) and (c) unit cell parameters over this LiH concentration range. The anisotropic unit cell changes begin for reactions in the range of 280-300mol% LiH. This is most easily observed by the gradual increase in c-axis length and a gradual decrease in a-axis length initiating at 280 mol% LiH and proceeding to 600mol% LiH. Notably the unit cell axistrends are mirrored by a very similar trend for Mn-O1 (equatorial) and Mn-O2 (apical) bond distances. These anisotropic unit cell changes are reflected by drastic changes in unit cell volume. The unit cell volume approaches that of Sr_2MnO_4 due to compensation of the a-axis compression and c-axis expansion. Calculation of the octahedral distortion index reveals an increasing value as the concentration of LiH increases. This is consistent with the increase and decrease in apical and equatorial bond lengths respectively, resulting from Jahn-Teller distortion of Mn^{3+} octahedra. A 800mol% LiH trial was carried out which resulted in complete decomposition of the starting material. It should be noted that those reaction products between 120-180mol% LiH were refined in the monoclinic unit cell consistent with ~$Sr_2MnO_{3.63.}$ All other products were refined in the original tetragonal cell as monoclinic superstructure peaks were not observed. The identified drastic LiH concentration dependence was unexpected.

Furthermore the two distinct plateaus observed in both unit cell volume and unit cell dimensions (figure 3.14) suggest the existence of at least 2 new stoichiometric phases that are accessible by solid state reduction. The potential for the products to be oxyhydrides appears unlikely as stirring and filtering the 400mol% product in warm water had no influence on the refined unit cell dimensions. Thus the most likely explanation for the observed trend is lithium intercalation.

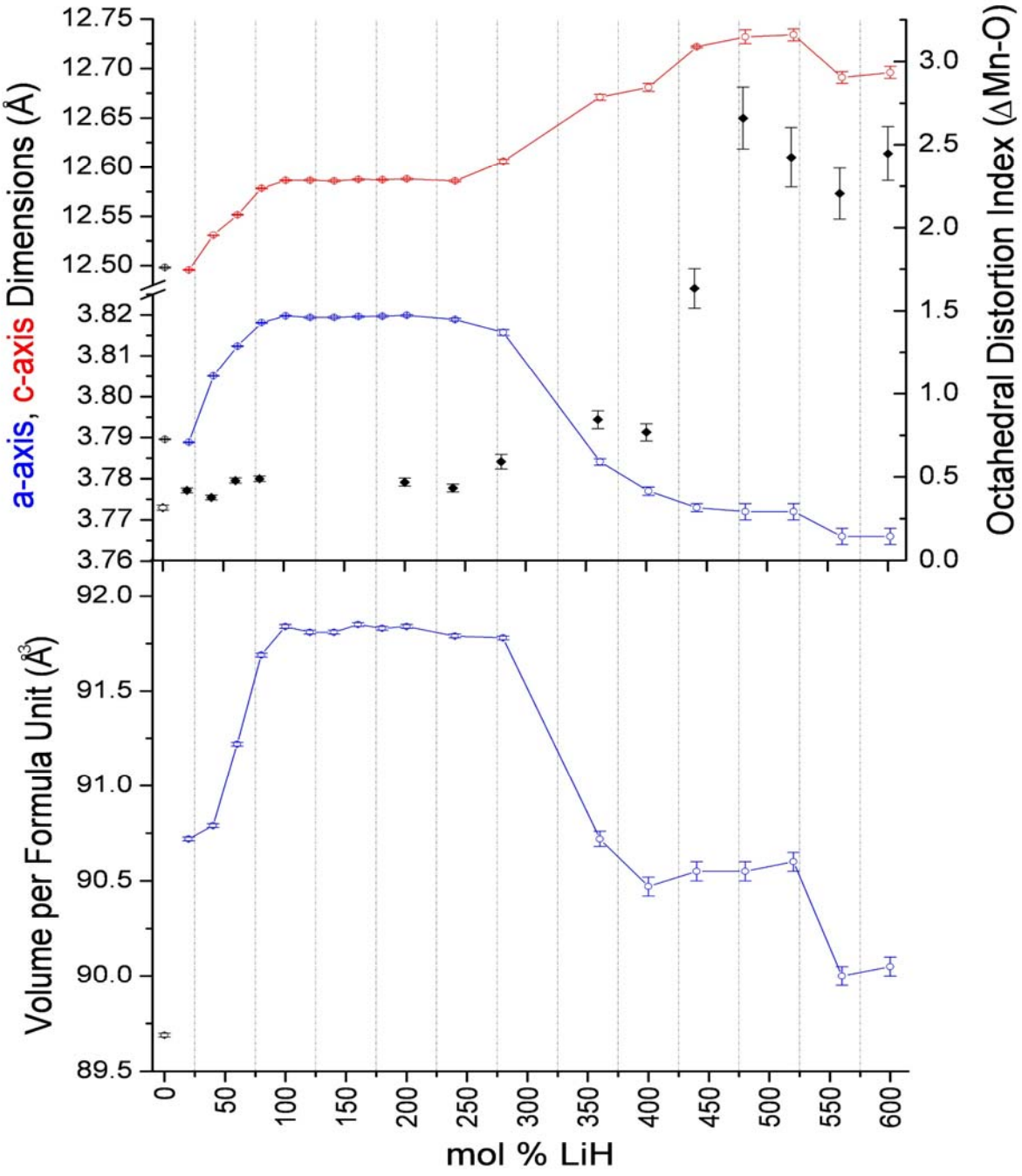

Figure 3.14. Lower - Volume per formula unit (Sr_2MnO_4) evolution as a function of mol % LiH (blue).Upper – a-axis and c-axis unit cell dimensions, and octahedral (MnO_6) distortion index as a function of mol % LiH. Note: unit cell axis parameters result from refinement of all products in a tetragonal setting. a-axis- blue, c-axis- red, distortion index- black. 0°C data correspond to the respective starting material (Sr_2MnO_4) values. Reaction T = 400°C. $\Delta = 1/n\sum_n[(r_i - r)/r]^2 1000$, Δ = octahedral distortion index, r_i = Mn-O bond length, r = average Mn-O bond length, $n = 6$.

3.7. Sr_2MnO_4: H^- vs. H_2 and Vacuum

It is important to realize that the environment within the sealed ampoules for the metal hydride reductions is not simple. In order to understand the reduction we need to consider oxygen partial pressure above the solid, hydrogen pressure above the solid and the presence of H^- anions in the solid state. This makes it difficult to prove that such reductions occur purely in the solid state. Current literature provides no insight into the influences of H_2 or static vacuum on metal hydride reductions. A variety of reactions have been performed with Sr_2MnO_4 to probe the factors influencing metal hydride reductions. The influence of hydrogen gas on reduction was investigated by carrying out reductions of Sr_2MnO_4 in flowing 100% H_2 (1atm H_2) and 50:50 (H_2(0.5atm) :Ar). These H_2 flow reactions can be compared to the influence of H_2 on sealed ampoule reductions. One such comparison can be made using a series of reductions of Sr_2MnO_4 with CaH_2 where ampoule volumes were varied as a function of temperature so that a maximum of 1atm H_2 pressure could be achieved (figure 3.15-green). Reductions of Sr_2MnO_4 carried out in a tube furnace in pure H_2 flow result in reduction beginning at 300^{o}C reaching a maximum at 400^{o}C and complete decomposition at 600^{o}C. Note that decomposition at 600^{o}C is also observed for the CaH_2 thimble reductions. The first observation to be made is that none of the preliminary reduction trends using any metal hydrides resulted in complete decomposition at 600^{o}C. Reductions in flowing 50:50 (H_2:Ar) vary from pure H_2 in that no reduction is observed at 300^{o}C and that no decomposition is observed at 600^{o}C. Looking now at the volume controlled CaH_2 (max p (H_2) = 1atm) reductions the trend is very similar to the preliminary CaH_2 reductions however it does not reduce to the

same maximum. In figure 3.15 most information can be gained by focusing on the reaction

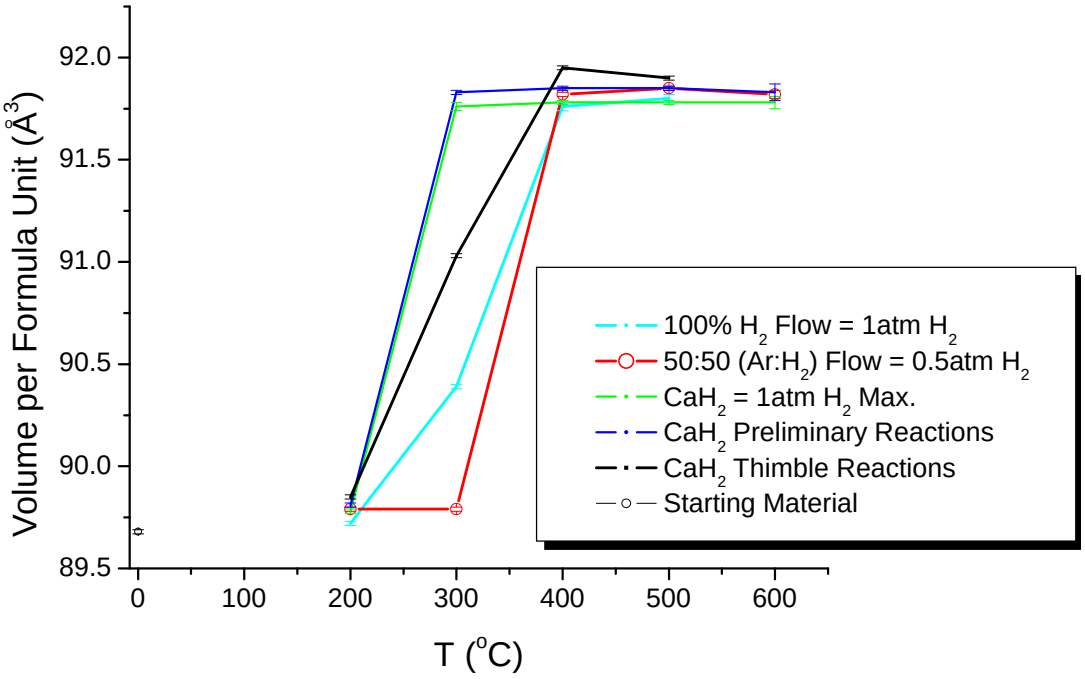

Figure 3.15. Volume per formula unit (Sr_2MnO_4) as a function of temperature focusing on the dependence of reduction on the presence of variable hydrogen atmosphere.

temperature of 300°C. There appears to be a relationship between hydrogen atmosphere and reduction such that reduction increases at 300°C in the order 50:50 (0.5atm) H_2 flow, 100% (1atm) H_2 flow, followed by the thimble reaction result (p_{max} = 1.3atm at 300°C). The fact that identical volume ampoules are used for both the preliminary CaH_2 reduction and the thimble reductions means that the maximum H_2 pressure is equivalent at 1.3atm at 300°C. Hence the more extensive reduction at 300°C for the preliminary reductions is a clear indication that a solid state component is dominating the reduction process.

Thimble reactions have allowed for the combined influence of H_2 and static vacuum on the reduction of Sr_2MnO_4 to be evaluated. Thimble reactions for Sr_2MnO_4 with NaH show a consistently small reduction independent of temperature (figure 3.16). Interestingly these results were found to be in very good agreement with reduction reactions of Sr_2MnO_4 under static vacuum as shown in figure 3.16. This confirms that all reductions of Sr_2MnO_4 using NaH regardless of temperature have a dominant solid state reduction component. This also brings up the fact that NaOH is commonly produced as a reaction by-product instead of the corresponding metal oxide. It is anticipated that this is the result of equation 3.1. Water could be present as a result of protons being produced by H_2 reducing Sr_2MnO_4. However the reduction of Sr_2MnO_4 with H_2 is shown to be minimal in figure 3.16.

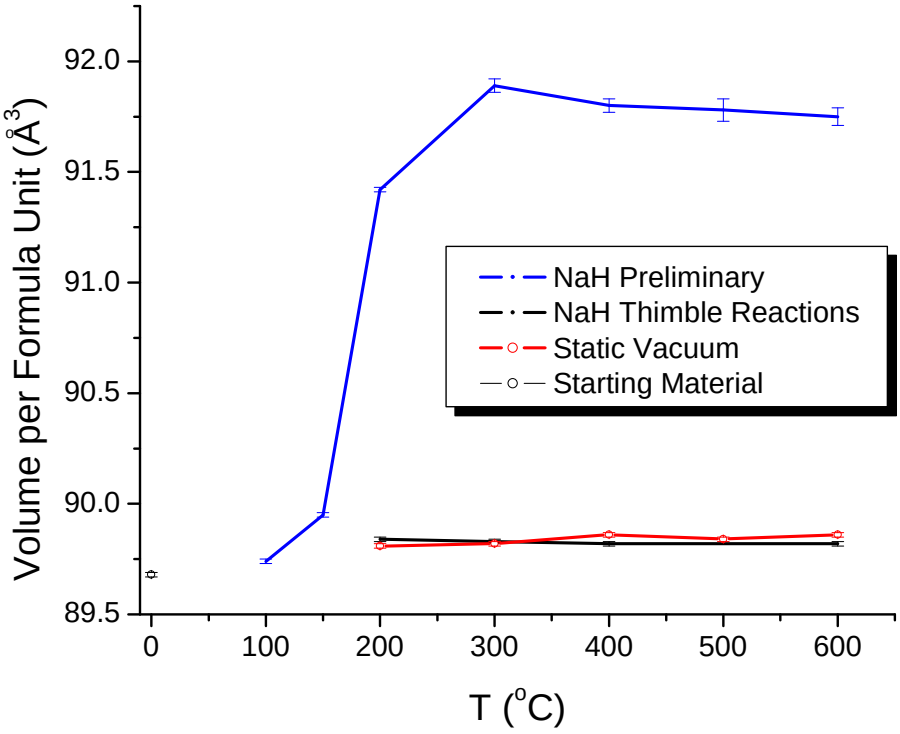

Figure 3.16. Volume per formula unit (Sr_2MnO_4) as a function of temperature focusing on the influence of NaH, H_2 and static vacuum on reduction.

$$Na^{+} + H_2O \rightarrow NaOH + H^{+} \qquad \textbf{3.1}$$

Figure 3.16 also indicates that the influence of static vacuum on the metal hydride reductions is less influential than H^- and H_2. Figure 3.17 compares the results for the LiH thimble reductions with the preliminary LiH reductions and flowing hydrogen reductions. A similar conclusion is drawn from figure 3.17 for LiH as was for figure 3.15 for CaH_2. This being the significant solid state component of reduction obvious by the maximum achieved at 300°C for the preliminary LiH reduction. In regards to the previous discussion of potential lithium insertion using LiH the 400°C reaction temperature in figure 3.17 clearly shows that either Li^+ or H^- insertion contribute directly to the small unit cell volume. A decreased unit cell volume is only observed for the preliminary reaction in which the starting material is in direct contact with LiH.

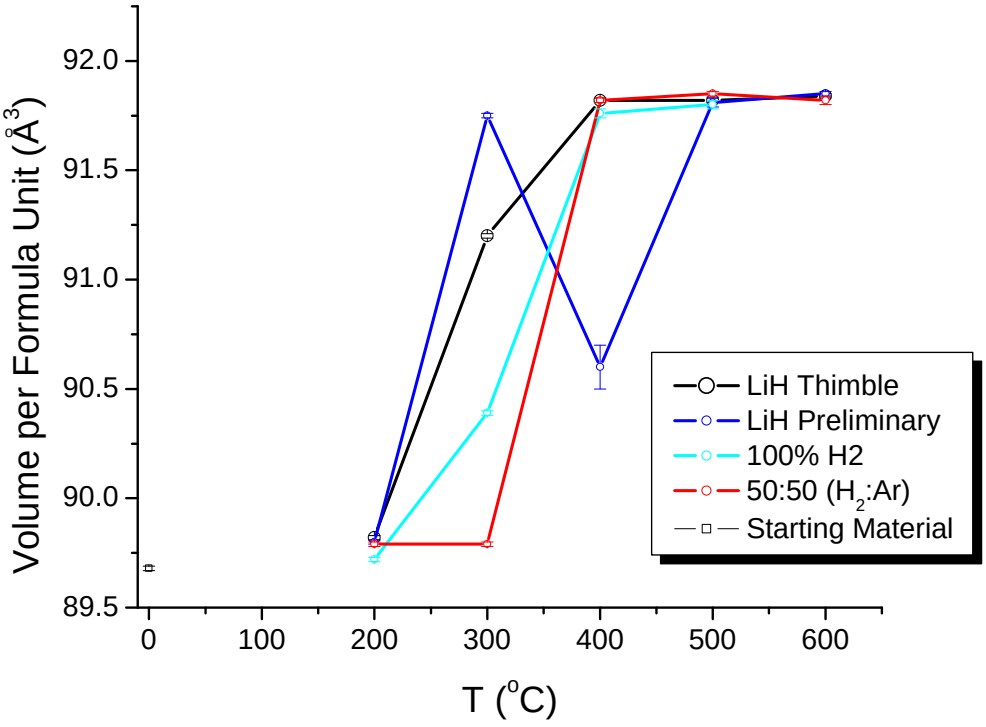

Figure 3.17. Volume per formula unit (Sr_2MnO_4) as a function of temperature focusing on the influence of LiH and H_2 on reduction.

An interesting finding resulted from the MgH_2 thimble reductions. As shown in figure 3.18 there is strong resemblance between the preliminary MgH_2 reduction trend with that of the MgH_2 thimble reactions and the 50:50 (H_2:Ar) flow reductions. This is very strong evidence that the preliminary reductions using MgH_2 are the result of H_2 reduction. It is important to note that this is the only metal hydride tested that shows evidence for H_2 being the dominant reducing agent. This is consistent with the fact that MgH_2 has the lowest decomposition temperature of all metal hydrides tested (table 3.4). It is also interesting to contrast that NaH has the next lowest decomposition temperature while it is the only metal hydride which conclusively shows strong evidence for purely solid state reductions throughout the entire temperature range. This emphasizes the challenges associated with understanding metal hydride reductions.

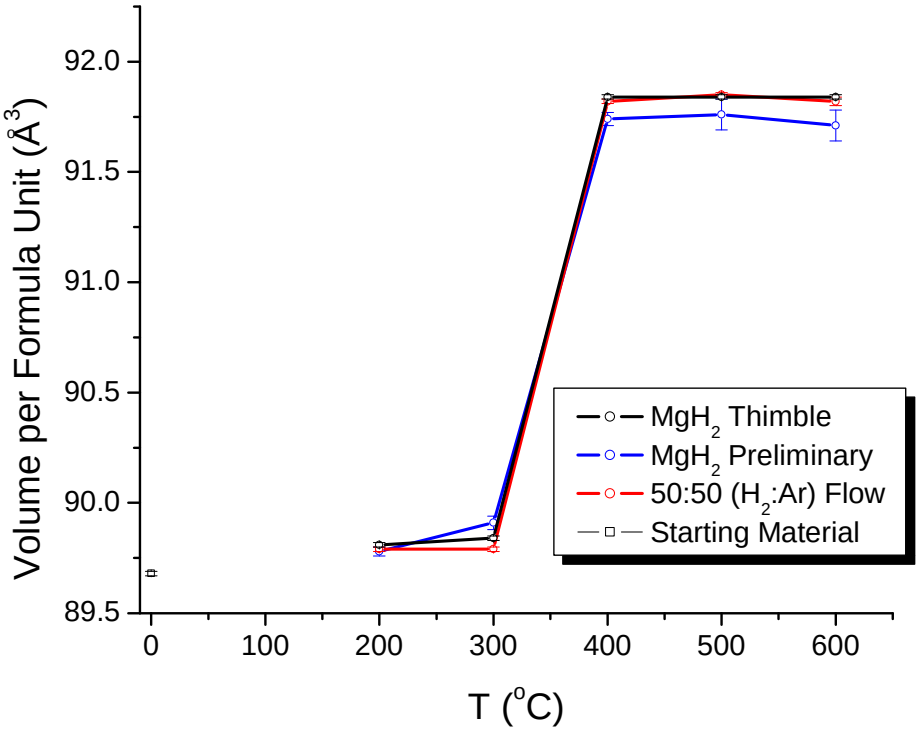

Figure 3.18. Volume per formula unit (Sr_2MnO_4) as a function of temperature focusing on the influence of MgH_2 and H_2 on reduction.

3.8. In-situ Reduction Study of Sr_2MnO_4 and Ca_2MnO_4

An in-situ powder X-ray diffraction reduction study was carried out on Sr_2MnO_4 and Ca_2MnO_4. Reductions of each starting material were carried out in $CO:CO_2$ (1:9, 3:7, 7:5, 9:1, 10:0) heating from room temperature to 700^oC collecting data at 25^oC increments. The carbon monoxide reductions proceed according to equation 12 (A = Sr, Ca).

$$A_2MnO_4 + xCO \rightarrow Sr_2MnO_{4-x} + xCO_2 \qquad \textbf{12}$$

As it was experimentally observed initially that Sr_2MnO_4 was a much more suitable starting material for metal hydride reductions than Ca_2MnO_4 it is anticipated that this in-situ study will reinforce this observation. A control experiment was carried out on each starting material using the same heating and measurement program in static air allowing for unit cell thermal expansion to be differentiated from reduction. Notably the unit cell expansions for the control experiments for Sr_2MnO_4 and Ca_2MnO_4 are linear, this serves as strong evidence that no oxidation takes place, consequently the assumption that A_2MnO_4 (A = Sr, Ca) systems are fully oxidized is confirmed. A total of 6 reduction experiments for each starting material allowed for approximately 330 Rietveld refinements to be carried out. The results are shown as volumes per formula unit for Sr_2MnO_4 and Ca_2MnO_4 in figure 3.19(a) and 3.19(b) respectively.

Figure 3.19(a) demonstrates the ability to controllably reduce Sr_2MnO_4 as a function of reduction potential. Reductions of Sr_2MnO_4 using $CO:CO_2$ begin between 225^oC and 275^oC, with higher concentrations of CO starting at lower temperatures. There is a close correlation between the concentration of CO reductant and the extent of reduction. This is easily observed from the insets in figure 3.19(a,b) which show %

volume change per formula unit as a function of temperature for each reaction atmosphere. Thermal expansion values from the control experiments were subtracted to allow for unit cell volumes to be obtained that are representative of the reduced phase unit cell. From the percentage volume change per formula unit plot (figure 3.19a - inset) the maximum rate of reduction is typically in the 400-500^{o}C range. Maximum reduction is typically observed between 525-625^{o}C (table 3.7) followed by a decrease in volume. The decrease in unit cell volume is indicative of oxidation, however the presence of this feature in the pure CO experiment also introduces the possibility of changes in thermal expansion for the reduced phases. The maximum reduced phase synthesized as shown in table 3.7 is approximately $Sr_2MnO_{3.60(5)}$ very similar to the maximum reduced phase of $Sr_2MnO_{3.63(1)}$ synthesized using metal hydrides (table 3.5). Comparing the results in 3.19(a) and (b) reveals that reduction of Ca_2MnO_4 does not begin until ~375^{o}C for highest CO concentrations while the lowest concentration of 1:9 ($CO:CO_2$) showed no reduction until 650^{o}C. Comparison of the insets in figure 3.19(a) and (b) show that Sr_2MnO_4 has a maximum volume change of ~2.4% per formula unit compared to a maximum of ~0.9% for Ca_2MnO_4. Complete decomposition of Ca_2MnO_4 is observed above 475^{o}C in pure CO to $Ca_{0.835}Mn_{0.165}O$, $Ca_{0.747}Mn_{0.253}O$ and $Ca_{0.559}Mn_{0.441}O$. Decomposition products were identified by subsequent room temperature powder X-ray diffraction of the Ca_2MnO_4/CO in-situ product.

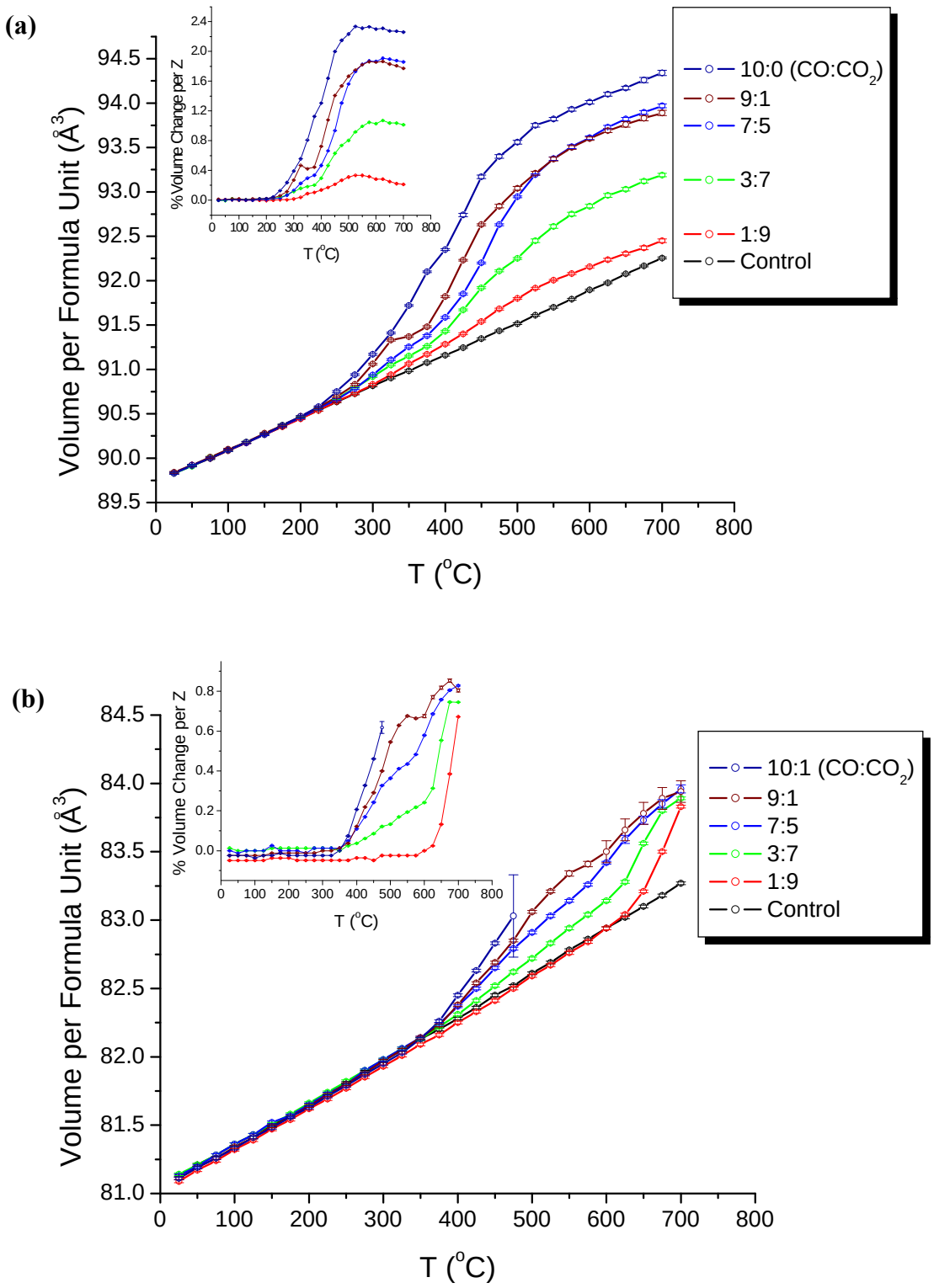

Figure 3.19. Evolution of volume per formula unit Sr_2MnO_4 (a) and Ca_2MnO_4 (b) as determined from Rietveld refinements of in-situ powder X-ray diffraction reduction experiments using various $CO:CO_2$ ratios. Insets in (a) and (b) show the % volume change per formula unit as a function of temperature.

Table 3.7. Approximation of the maximum reduced phase stoichiometry (Sr_2MnO_{4-x}) achieved for each gas composition as extrapolated from figure 3.6.[a]

Gas Flow (CO: CO_2)	T – Max. Volume (^oC)	Volume per Z [b] ($Å^3$)	Extrapolated stoichiometry from Figure 3.6.
1:9	525	90.14(3)	$Sr_2MnO_{3.96(5)}$
3:7	625	90.81(3)	$Sr_2MnO_{3.82(5)}$
7:5	625	91.59(3)	$Sr_2MnO_{3.67(5)}$
9:1	575	91.54(3)	$Sr_2MnO_{3.68(5)}$
10:0	525	91.97(3)	$Sr_2MnO_{3.60(5)}$ [c]

[a] Estimated oxygen stoichiometries were based on extrapolation from a linear fit of volume per formula unit ($Å^3$) as a function of oxygen composition between the synthesized $Sr_2MnO_{3.99(1)}$ and $Sr_2MnO_{3.63(1)}$ phases(characterized in table 3.5)..
[b] Volume per formula unit has been corrected for thermal expansion.
[c] The maximum volume achieved using pure CO exceeded the range of TGA data collected and thus may be a less accurate estimate.

Overall Ca_2MnO_4 reduces at significantly higher temperatures than Sr_2MnO_4 while lacking the stability that Sr_2MnO_4 displays under reducing conditions and reducing to a significantly lesser extent to ultimately reinforce the choice of Sr_2MnO_4 as justified in section 3.2.

3.9. Starting Material vs. Metal Hydride

When establishing a successful system for carrying out metal hydride reductions as was the case for Sr_2MnO_4, distinction between the influences of starting material and metal hydride on reactivity must be considered. It could be proposed that the success of solid state reduction is solely dependent on the choice of metal hydride. Although this is highly unlikely based on the results shown in figure 3.19, to address this reductions of Ca_2MnO_4 were carried out with SrH_2 as this metal hydride allowed for highly controlled reductions

of Sr_2MnO_4. It is clear from figure 3.20 that SrH_2 provides no benefit over the previously carried out preliminary reductions using NaH or CaH_2 either in terms of starting material stability as a function of temperature or the extent of reduction observed. This finding reinforces that the choice of using NaH and CaH_2 for preliminary reduction trials is satisfactory for determining an appropriate starting material candidate for solid state reduction.

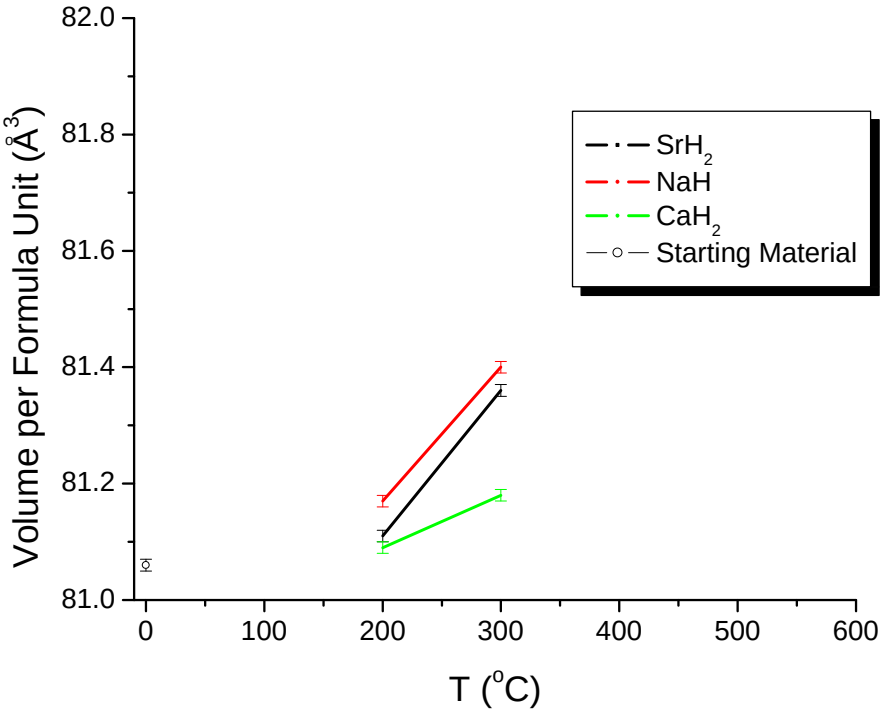

Figure 3.20. Volume per formula unit evolution as a function of temperature for Ca_2MnO_4 reduced with NaH, CaH_2 and SrH_2.

4. RESULTS AND DISCUSSION – PART II

4.1. Scandium Vanadate Reduction Attempts

$ScVO_4$ was reacted with NaH and CaH_2 in two series of reactions over a temperature range of 100-400°C typically at 25°C increments. Fine temperature steps were used to increase confidence in any potential trends observed. Powder X-ray diffraction Rietveld refinements of the $ScVO_4$ starting material (figure 4.1) and reaction products were carried out. Typically ~25 parameters were refined including scale factor, background, zero point, peak shape, peak asymmetry, unit-cell parameters and atomic coordinates. The refinement of $ScVO_4$ (figure 4.1, table 4.1) contained a minor Sc_2O_3 impurity phase.

Table 4.1. Refined unit cell parameters (upper table) and atomic coordinates (lower table) resulting from Rietveld refinement of powder X-ray diffraction data for $ScVO_4$.[a]

Number of Reflections	60
Number of Parameters	25
R_p (%)	3.82
R_{wp} (%)	6.05
R_B (%)	5.94
χ^2	15.3
Space Group	$I4_1/amd$
a (Å)	6.7783(1)
c (Å)	6.1341(1)
V (Å^3)	281.83(1)

Atom	x	y	z
Sc	0	3/4	1/8
V	0	1/4	3/8
O	0	0.4446(8)	0.1962(9)

[a] Site occupancy factors and thermal parameters (B_{iso}) were fixed.

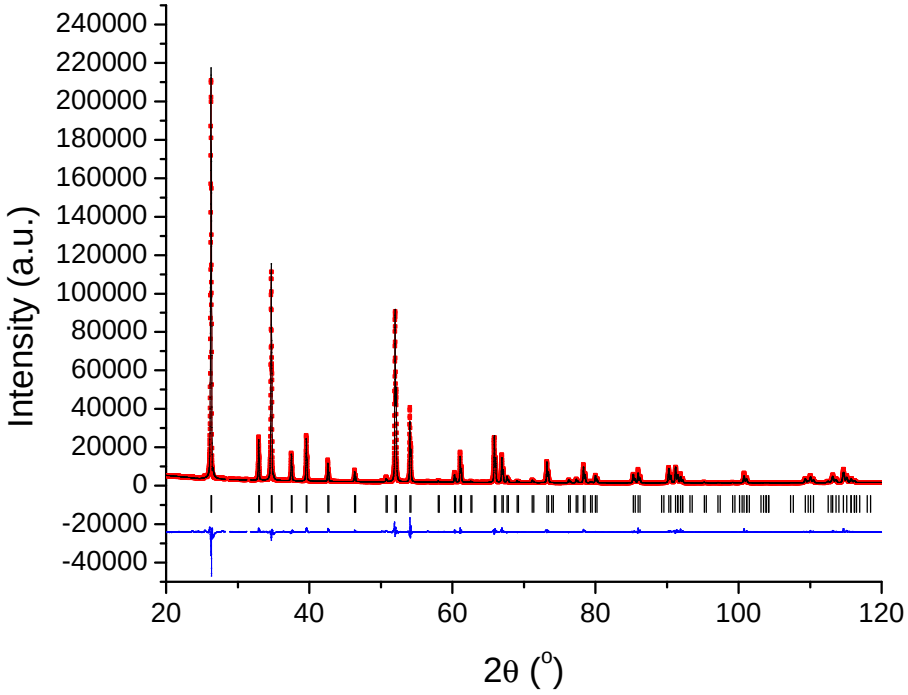

Figure 4.1. Room temperature Rietveld plot for $ScVO_4$, Cu $K\alpha_{1,2}$ (λ = 1.540598Å, 1.544426 Å). The red symbols are experimental data, the best fit and difference are shown as black and blue lines respectively. The black ticks correspond to individual Bragg reflections. Main impurity (Sc_2O_3) peaks at ~28.5° and ~31.5° have been excluded.

The reaction results of $ScVO_4$ with both CaH_2 and NaH are shown in figure 4.2a,b respectively. Inspection of the reaction products for $ScVO_4$ with CaH_2 (figure 4.2a) reveals no clear reduction trend due to the consistent oscillation of data points about the original starting material volume. Beyond 325°C reactions with CaH_2 result in impure products with a major $ScVO_3$ phase. The reaction results shown for NaH in figure 4.2b appear to show some sign of a decreased unit cell volume, however the 150°C product is consistent with the starting material. An explanation for a decrease in volume is not clear since literature shows that the oxygen defect zircon structure $ScVO_{3.94(2)}$ has a larger unit cell volume than $ScVO_4$. Above 200°C reaction products of $ScVO_4$ with NaH decompose

into multiple phases including $ScO_{0.95}$, Sc_2O_3 and V_2O_5 as determined by matching experimental data to the PDF database. The published volume per formula

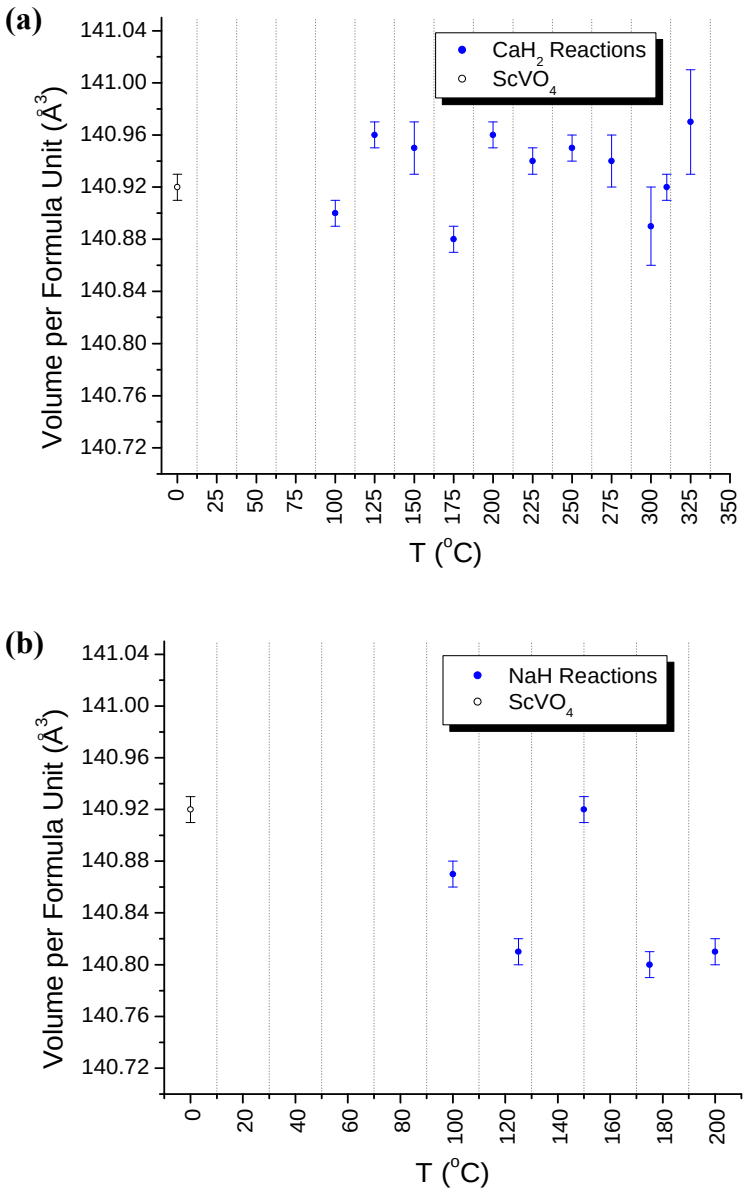

Figure 4.2. Reaction product volume per formula unit for CaH_2 (a) and NaH (b). The data point at 0°C corresponds to the starting material volume.

unit of $ScVO_{3.94(2)}$ is 141.03Å^3 and thus it can be concluded from figure 4.2 that this phase cannot be synthesized using NaH or CaH_2 as this volume is not produced.[104] It may however be possible that an intermediate reduced phase was produced using CaH_2 (e.g. $ScVO_{3.95\text{-}4.0}$).

In an effort to gain insight into the observed lack of reactivity of $ScVO_4$ with NaH and CaH_2 a sample of $ScVO_4$ was sealed in an evacuated ampoule and heated to 200^{o}C for 24 hours similarly to that previously described for Sr_2MnO_4. Unlike the partially reduced Sr_2MnO_{4-x} phase that resulted from this reaction, the product for the $ScVO_4$ vacuum reaction refined to be nearly within error to the starting material. This indicated that $ScVO_4$ was not capable of undergoing thermally induced reduction/oxygen loss at a temperature where this was observed for Sr_2MnO_4. This provides a qualitative comparison of oxide ion mobility in these phases and the lesser oxide ion mobility in $ScVO_4$ is consistent with the minimal reduction observed in figure 4.2. This may be an indication that poor oxygen mobility in the $ScVO_4$ zircon structure inhibits reduction. This proposal would be consistent with literature as the published $ScVO_{3.94(2)}$ phase was synthesized by an oxidative route (figure 1.24).

5. CONCLUSIONS & FUTURE WORK

Preliminary NaH and CaH_2 reduction trials allowed for identification of Sr_2MnO_4 as the most suitable Ruddlesden-Popper phase in the $Sr_{2-x}Ca_xMnO_4$ ($0<x<2$) system for comprehensive investigation using metal hydrides. Sr_2MnO_4 is the most stable starting material having a tolerance factor nearest to unity. This stability was supported by an in-situ powder X-ray diffraction CO/CO_2 reduction study in which Sr_2MnO_4 persisted under the most strongly reducing conditions (pure CO, 700^{o}C) while Ca_2MnO_4 decomposed. Novel reactivity trends have been developed for several group I and II metal hydrides (LiH, NaH, MgH_2, CaH_2, SrH_2, BaH_2) as reductants of Sr_2MnO_4. NaH and SrH_2 have been identified as the most suitable reductants of Sr_2MnO_4 based on the large temperature ranges (200^{o}C, 300^{o}C respectively) over which reduction occurs. NaH is the most reactive metal hydride at low temperatures (< 200^{o}C). The use of optimized reaction conditions for SrH_2 and NaH with Sr_2MnO_4 allowed for synthesis of several novel oxygen defect phases, Sr_2MnO_{4-x} ($0<x<0.37$). All compositions of Sr_2MnO_{4-x} with x < 037crystallize in a tetragonal structure. The only synthesized monoclinic phase was $Sr_2MnO_{3.63(1)}$ During oxidation of $Sr_2MnO_{3.63(1)}$ the transition from monoclinic to tetragonal takes place at 350^{o}C. The approach taken demonstrates how one can maximize benefit from the metal hydride reductant soft chemistry technique by understanding and controlling reaction conditions. This approach requires careful consideration of the starting material, reaction temperature and metal hydride.

A significant portion of this work focused on understanding the fundamental reduction mechanism for metal hydride reductions of Sr_2MnO_4. It can be concluded that NaH is the only metal hydride for which the results suggest purely solid state reduction

resulting from H^- anions. In the future reductions of Sr_2MnO_4 should be performed at the same temperature using Na powder to rule out the influence of sodium metal as a potential reductant. LiH and CaH_2 reduction results indicate that H^- is the dominating reductant and that the influence of H_2 and oxygen equilibrium effects must be considered as secondary and tertiary influences respectively. MgH_2 reductions were found to result purely from hydrogen gas. A general conclusion is that it is very difficult to characterize the nature of these reductions and that multiple factors (e.g. H^-, H_2, O_2 equilibrium, alkali/alkaline earth metals) are likely contributing to the final reduced product. Having said this all results for NaH, LiH and CaH_2 indicate that H^- is the most significant reductant.

Reaction results for LiH with Sr_2MnO_4 have shown strong dependence on LiH excess. Reductions producing $Sr2MnO4_{-x}$ ($0< x < 0.37$) phases result from a stoichiometric approach using LiH and from using excess (4-fold) LiH at select temperatures ($\leq 300^oC$, $\geq 500^oC$). A strong dependence on LiH concentration at 400^oC revealed highly convincing evidence for a novel Sr_2MnO_{4-x} phase doped with lithium. Future work should involve further characterization of these phases. Neutron diffraction data is anticipated to allow for successful structure solution regarding confirmation of the crystal system, determination of Li^+ location, and oxygen stoichiometry. XPS may also assist in successful characterization of manganese oxidation states present. It is also anticipated that low temperature powder X-ray diffraction data could be beneficial in understanding resultant magnetic properties. The dependence of such reactions on LiH concentration has not been explored in literature and may be a valuable approach to synthesizing lithium doped oxygen defect transition metal oxides.

Attempts to reduce $ScVO_4$ were carried out as an example of the application of metal hydride reductants to a different system. This particular system presented significant challenges due to the inability to carry out any high temperature reductions of $ScVO_4$ to intermediate oxygen compositions aside from $ScVO_3$. Reduction attempts were unsuccessful using NaH and CaH_2. However insights into the unsuccessful reductions came from the work on Sr_2MnO_4. The observed absence of oxygen equilibrium in an evacuated ampoule containing $ScVO_4$ during heating provided a structural comparison to that of Sr_2MnO_4 in which oxygen equilibrium is readily established. It is proposed that topotactic reduction of $ScVO_4$ is not possible due to reduction being inhibited by low oxide ion mobility. Thus proving that oxide ion mobility in Ruddlesden-Popper manganates is critical to successful metal hydride reduction.

This research has built a solid foundation for understanding and controlling metal hydride topotactic reductions. Future work should focus on applying this knowledge of metal hydride reactivity to reduce new systems. Systems most appropriate would be structures that are stable under reducing conditions to high temperatures (>600^{o}C) which support oxide ion mobility and flexibility in oxygen stoichiometry. Ruddlesden-Popper phases with tolerance factors near unity are very good candidates. Attempts to work with other layered materials such as Aurivillius or Dion-Jacobson phases may also prove to be successful. Advanced approaches involving single or multi-step reduction/insertion reactions are expected to develop continually.

6. APPENDIX A

Table A.1. Crystallographic data for polycrystalline starting materials from powder X-ray diffraction refinement.

Phase	a (Å)	c (Å)	Z	Space Group	Unit Cell Volume (Å^3)
$Sr_{1.964(6)}Ba_{0.036(6)}MnO_4$	3.7917(4)	12.512(3)	2	I4/mmm	179.89(3)
$Sr_{1.98}Ba_{0.02}MnO_4$[a]	3.7905(4)	12.504(1)	2	I4/mmm	179.66(3)
Sr_2MnO_4[a]	3.7886(2)	12.4952(8)	2	I4/mmm	179.35(2)
$Sr_{1.88(1)}Ca_{0.12(1)}MnO_4$	3.7795(4)	12.443(1)	2	I4/mmm	177.74(3)
$Sr_{1.61(1)}Ca_{0.39(1)}MnO_4$	3.7723(4)	12.396(2)	2	I4/mmm	176.40(4)
$Sr_{0.454(6)}Ca_{1.546(6)}MnO_4$	5.2264(4)	24.230(2)	8	$I4_1$/acd	661.86(9)
$Sr_{0.211(3)}Ca_{1.789(4)}MnO_4$	5.2088(2)	24.1917(8)	8	$I4_1$/acd	656.35(4)
Ca_2MnO_4[a]	5.1861(3)	24.122(2)	8	$I4_1$/acd	648.78(7)

[a] *The Rietveld refinements of the end members of the solid solutions as well as the least barium rich phase had their site occupancies fixed.*

7. REFERENCES

1. Pecharsky, V. K.; Zavalij, P. Y. Fundamentals of Powder Diffraction and Structural Characterization of Materials, 2nd Ed; Springer: Maryland, USA, 2009.
2. Viswanathan, B. Structure and Properties of Solid State Materials; Alpha Science: Oxford, U.K., 2006.
3. Mabbs, F. E.; Machin, D. J. Magnetism and Transition Metal Complexes; John Wiley & Sons, Inc.: New York, 1973.
4. Goodenough, J. B. Magnetism and the Chemical Bond; John Wiley & Sons Inc.: USA, 1963, Volume 1.
5. Goodenough, J. B. J. Phys. Chem. Solids. **1958,** 6, 287-297.
6. Kanamori, J. J. Phys. Chem. Solids. **1959,** 10, 87-98.
7. Zener, C. Phys. Rev. **1951,** 81, 440-444.
8. Zener, C. Phys. Rev. **1951,** 82, 403-405.
9. Kramers, H. A. Physica. **1934,** 1, 182-192.
10. Anderson, P. W. Phys. Rev. **1950,** 79, 350-356.
11. Anderson, P. W. Phys. Rev. **1959,** 115, 2-13.
12. Rouxel, J.; Tournoux, M. Solid State Ionics. **1996,** 84, 141-149.
13. Craven, W. E.; Osterag, W. Carbon. **1966,** 4, 223-226.
14. Dines, M. B. Science. **1975,** 188, 1210-1211.
15. Somoano, R. B.; Rembaum, A. Phys. Rev. Lett. **1971,** 27, 402-404.
16. Murphy, D. W.; Carides, J. N.; et al. Mat. Res. Bull. **1977,** 12, 825-830.
17. Tournoux, M.; Brohan, L.; et al. Mat. Res. Bul. **1980,** 15, 1129-1133.
18. Tournoux, M.; Marchland, R.; et al. Prog. Solid State Chem. **1986,** 17, 33-52.

19. Verbaere, A.; Tournoux, M. Bull. Soc. Chim. Fr. **1973,** 4, 1237-1241.

20. Sasaki, T.; Watanabe, M.; et al. J. Solid State Chem. **1991,** 92, 537-542.

21. Dion, M. J. Inorg. Nucl. Chem. **1978,** 40, 917-918.

22. Moriga, T.; Usaka, O.; et al. Solid State Ionics. **1995,** 79, 252-255.

23. Hansteen, O. H.; Fjellvag, H.; et al. J. Mater. Chem. **1998,** 8, 2081-2088.

24. Hayward, M. A.; Green, M. A.; et al. J. Am. Chem. Soc. **1999,** 121, 8843-8854.

25. Cotton, F. A.; Wilkinson, G. Advanced Inorganic Chemistry: A Comprehensive Text, 4th Ed; John Wiley & Sons: Canada, 1980, pp 247-252.

26. Shull, C. G.; et al. Phys. Rev. **1948,** 73, 842-847.

27. Bergsma, J.; Loopstra, B. O. Acta Cryst. **1962,** 15, 92-93.

28. Ellinger, F. H.; et al. **1955,** 77, 2647-2648.

29. Setten, M. J. V.; Wijis, G. A. Phys. Rev. B. **2008,** 77, 165115.

30. Grochala, W.; Edwards, P. P. Chem. Rev. **2004,** 104, 1283-1315.

31. Cotton, F. A.; et al. Advanced Inorganic Chemistry, 6th Ed; John Wiley & Sons, Inc.: Canada, 1999, pp 77-77.

32. Brown, H. C.; Schlesinger, H. I.; et al. J. Am. Chem. Soc. **1939,** 61, 673-680.

33. Chaikin, S. W.; Brown, W. G. J. Am. Chem. Soc. **1949,** 71, 122-125.

34. Schlesinger, H. I.; Brown, H. C.; et al. J. Am. Chem. Soc. **1953,** 75, 199-204.

35. House, H. O. Modern Synthetic Reactions, 2nd Ed; W.A. Benjamin, Inc.: USA, 1972.

36. Bittman, R.; Ciganek, E.; et al. Organic Reactions; John Wiley & Sons, Inc.:USA, 1985; Volume 34.

37. Atkins, P. W.; Shriver, D. F.; et al. Inorganic Chemistry, 4th Ed; W.H. Freeman and Co.: USA, 2006.

38. Hayward, M. A.; Lockett, M. A.; et al. J. Solid State Chem. **2007,** 180, 2851-2858.

39. Hayward, M. A.; Hadermann, J.; et al. J. Am. Chem. Soc. **2009,** 131, 10598-10604.

40. Hayward, M. A.; Adkin, J. J. Inorg. Chem. **2008,** 47, 10959-10964.

41. Tsujimoto, Y.; et al. Nature. **2007,** 450, 1062-1066.

42. Hayward, M. A.; Casey, P. S.; et al. J. Solid State Chem. **2006,** 179, 1375-1382.

43. Hayward, M. A.; Rosseinsky, M. J. Solid State Sci. **2003,** 5, 839-850.

44. Hayward, M. A.; Overton, A. J.; et al. Chem. Mater. **2009,** 21, 4940-4948.

45. Hayward, M. A.; Kitchen, H. J.; et al. Dalton Trans. **2010,** 39, 6098-6105.

46. Hayward, M. A.; Bieringer, M.; et al. Science. **2002,** 295, 1882-1884.

47. Hayward, M. A. Chem. Mater. **2006,** 18, 321-327.

48. Kageyama, H.; Watanabe, T.; et al. Angew. Chem. Int. Ed. **2008,** 47, 5740-5745.

49. Hayward, M. A.; Helps, R. M.; et al. Inorg. Chem. **2010,** 49, 11062-11068.

50. Hayward, M. A. Chem. Mater. **2005,** 17, 670-675.

51. Hayward, M. A.; Dixon, E. Inorg. Chem. **2010,** 49, 9649-9654.

52. Hayward, M. A.; Lockett, M. A.; et al. J. Solid State Chem. **2007,** 180, 2851-2858.

53. Hayward, M. A.; Lockett, M. A.; et al. Inorg. Chem. **2008,** 47, 5212-5217.

54. Hazen, R. M.; Burnham, C. W. Am. Mineral. **1974,** 59, 1166-1176.

55. Goodenough, J. B.; Zhou, J. S. Chem. Mater. **1998,** 10, 2980-2993.

56. Weller, M. T.; Knee, S. C. Chem. Commun. **2002,** 256-257.

57. Louriero, S. M.; Felser, C.; et al. Chem. Mater. **2000,** 12, 3181-3185.

58. Knee, C. S.; Field, M. A. L.; et al. Solid State Sci. **2004,** 6, 443-450.

59. McGlothlin, N.; Cava, R. J.; et al. Mater. Res. Bull. **2000,** 35, 1035-1043.

60. Vente, J. F.; Kamenev, K. V.; et al. Phys. Rev. B. **2001,** 64, 214403.

61. Hayward, M. A.; Blundell, S. J.; et al. Physica B. **2003,** 326, 527-531.

62. Hayward, M. A.; Rosseinsky, M. J. Chem. Mater. **2000,** 12, 2182-2195.

63. Rosseinsky, M. J.; Hayward, M. A.; et al. J. Am. Chem. Soc. **2005,** 127, 5996-6011.

64. Rosseinsky, M. J.; et al. Chem. Mater. **2006,** 18, 3046-3056.

65. Megaw, H. D. Proc. Phys. Soc. **1946,** 58, 133-152.

66. Woodward, P. M. Acta Cryst. **1997,** B53, 32-43.

67. Bailey, P. C.; Kay, H. F. Acta Cryst. **1957,** 10, 219.

68. Goldschmidt, V. M. Die Gesetze der Krystallochemie. **1926,** 21, 477-485.

69. Glazer, A. M. Acta Cryst. **1975,** A31, 756-762.

70. Woodward, P. M. Acta Cryst. **1997,** B53, 44-66.

71. Howard, C.; Stokes, H. T. Acta Cryst. **1998,** B54, 782-789.

72. Balz, D. Nautwissenschaften. **1953,** 40, 241.

73. Balz, D.; Plieth, K. Z. Elektrochem. Angew. Phys. Chem. **1955,** 59, 545-551.

74. Bringley, J. F.; Trail, S. S.; et al. J. Solid State Chem. **1990,** 86, 310-322.

75. Ganguli, D. J. Solid State Chem. **1979,** 30, 353-356.

76. Chen, B. H. J. Solid State Chem. **1996,** 125, 63-66.

77. Poix, P. J. Solid State Chem. **1980,** 31, 95-102.

78. Miwa, K.; Kagomiya, I.; et al. J. Eur. Ceram. Soc. **2007,** 27, 4287-4290.

79. Primak, W.; Kaufman, H.; et al. J. Am. Chem. Soc. **1948,** 70, 2043-2046.

80. Ruddlesden, S.; Popper, P. Acta Cryst. **1957,** 10, 538-540.

81. Ruddlesden, S. N.; Popper, P. Acta Cryst. **1958,** 11, 54-55.

82. Popper, P.; Ruddlesden, S. N. Trans. Br. Ceram. Soc. **1963,** 62, 443-449.

83. Jorgensen, J. D.; Dabrowski, B.; et al. Phys. Rev. B. **1989,** 40, 2187-2199.

84. Fjellvag, H.; Hansteen, O. H.; et al. J. Mater. Chem. **2000,** 10, 749-754.

85. Stephen, J.; Skinner, J.; et al. Mater. Today. **2003,** March, 30-37.

86. Kharton, V. V.; Viskup, A. P.; et al. J. Mater. Chem. **1999,** 9, 2623-2629.

87. Kharton, V. V.; Viskup, A. P.; et al. Solid State Ionics. **2001,** 143, 337-353.

88. Skinner, S. J.; Kilner, J. A. Solid State Ionics. **2000,** 135, 709-712.

89. Tezuka, K.; et al. J. Solid State Chem. **1999,** 145, 705-710.

90. Kriegel, R.; Preuß, N. Thermochim. Acta. **1996,** 285, 91-98.

91. Poeppelmeier, K. R.; et al. J. Solid State Chem. **1985,** 59, 71-80.

92. Poeppelmeier, K. R.; Leonowicz, M. E.; et al. J. Solid State Chem. **1982,** 45, 71-79.

93. Suescun, L.; Chmaissem, O.; et al. J. Solid State Chem. **2007,** 180, 1698-1707.

94. Jorgensen, J. D.; Chmaissem, O.; et al. Phys. Rev. B. **2003,** 67, 094431.

95. Poeppelmeier, K. R.; et al. J. Solid State Chem. **1982,** 44, 89-98.

96. Kriegel, R.; Borrmann, H.; et al. Z. Naturforsch., B: Chem. Sci. **1993,** 48b, 15-18.

97. Kriegel, R.; Preuß, N. Thermochim. Acta. **1996,** 285, 91-98.

98. Gillie, L. J. et al. J. Solid State Chem. **2002,** 167, 145-151.

99. Bouloux, J. C.; Soubeyroux, J. L.; et al. J. Solid State Chem. **1981,** 38, 34-39.

100. Kato, C.; Iikubo, S.; et al. J. Phys. Soc. Jpn. 74, 1026-1029.

101. Sullivan, E. C. Anion Manipulation in Perovskite Related Materials. Ph.D. Thesis, University of Birmingham. 2009.

102. Labanov, M. V.; Abakumov, A. M.; et al. Solid State Sci. **2002,** 4, 19-22.

103. Cox, D. E.; Shirane, G.; et al. Phys. Rev. **1969,** 188, 930-932.

104. Bieringer, M.; Shafi, S. P.; et al. Inorg. Chem. **2009,** 48, 10553-10559.

105. Reid, A. F.; Sienko, M. J. Inorg. Chem. **1967,** 6, 521-524.

106. Chakoumakos, B. C.; Abraham, M. M.; et al. J. Solid State Chem. **1994,** 109, 197-202.

107. Milligan, W. O.; Vernon, L. W. J. Phys. Chem. **1952,** 56, 145-147.

108. Alonso, J. A.; Casais, M. T.; et al. Dalton. Trans. **2004,** 1294-1297.

109. Shafi, S. P.; Bieringer, M.; et al. J. Solid State Chem. **2007,** 180, 3333-3340.

110. Rodriguez- Carvajal, J. Full Prof 2k Vers. 4.40, 2008.

111. Shannon, R. D. Acta Cryst. **1976,** A32, 751-767.

112. George, L.; Saxena, S. K. Int. J. Hydrogen Energy **2010,** 35, 5454-5470.

113. Smithson, H.; Marianetti, C. A.; et al. Phys. Rev. B. **2002,** 66, 144107.

114. Standnes, A. CHEMIX School Vers. 3.51, 2010.

115. Lide, D. R.; et al. CRC Handbook of Chemistry and Physics, 90th Ed; CRC Press: USA, 2009-2010.